RMIT
UNIVERSITY

Energetically Deposited Tin Oxide:
Characterization and Device Applications

A thesis submitted in fulfilment of the requirements for the degree of

Doctor of Philosophy

Phuong Yen Le

M.Eng.

RMIT University Vietnam

School of Engineering

College of Science, Engineering and Health

RMIT University

March 2019

Declaration

I certify that except where due acknowledgement has been made, the work is that of the author alone; the work has not been submitted previously, in whole or in part, to qualify for any other academic ward; the content of the thesis is the result of work which has been carried out since the official commencement date of the approved research program; and, any editorial work, paid or unpaid, carried out by a third party is acknowledged.

Phuong Yen Le

March 2019

Acknowledgements

I would like to thank my supervisors Assoc. Prof. Anthony Holland and Dr James Partridge for their continuous guidance, support and valuable suggestions. I am also thankful for all the encouragement and inspiration that they have given me.

I would like to thank Dr Billy Murdoch, Hiep Tran, Tom Raeber, Cindy Zhao and Chi-Ping Wu for helping me during my research. I am also thankful to the technical staff at RMIT microscopy and microanalysis facility for their support during the characterisation of samples throughout the research work.

My love and thanks go to my husband, Tuan for always encouraging, supporting and loving me. Finally, my love and gratitude go to my parents and my little sister. Thank you for 30 years of love and support.

Table of Contents

List of Figures

List of Tables

List of Abbreviations and Acronyms

AES	Auger Electron Spectroscopy
AFM	Atomic Force Microscopy
AM	Active Matrix
AOS	Amorphous Oxide Semiconductor
BE	Binding Energy
CBM	Conduction Band Minimum
CC-NDR	Current-Controlled Negative Differential Resistance
CMOS	Complementary Metal Oxide Semiconductor
CMVB	Chemical Modulation of the Valence Band
CVD	Chemical Vapour Deposition
DCMS	Direct Current Magnetron Sputtering
EB	Electron Beam
ECM	Electrochemical Metallization Memory
EEL	Electron Energy Loss
EELS	Electron Energy Loss Spectroscopy
FE	Field-Emission
FPGA	Field Programmable Gate Array
GZTO	Gallium Zinc Tin Oxide
HiPIMS	High-Power Impulse Magnetron Sputtering
HRS	High Resistance State
HR-TEM	High Resolution Transmission Electron Microscopy
ITO	Indium Tin Oxide
KE	Kinetic Energy
LCD	Liquid Crystal Display
LPCVD	Low-Pressure Chemical Vapour Deposition
LRS	Low Resistance State
LSM	Liquid State Machine
LTP	Long-Term Potentiation
MBE	Molecular Beam Epitaxy
MIM	Metal – Insulator – Metal
NDR	Negative Differential Resistance
NND	Nanoparticle Network Device
OLED	Organic Light-Emitting Diode
PECVD	Plasma-Enhanced Chemical Vapour Deposition
PLD	Pulsed Laser Deposition
PPD	Paired-Pulse Depression
PPF	Paired-Pulse Facilitation
RC	Reservoir Computing
RF	Radio Frequency
ROI	Region Of Interest
SAN	Scanning Auger Nanoprobe
SEM	Scanning Electron Microscope
SMU	Source-Measurement Unit
SPM	Scanning Probe Microscopy
STDP	Spiking-Time Dependent Plasticity

STP	Short-Term Plasticity
TCO	Transparent Conducting Oxide
TEM	Transmission Electron Microscopy
FD	Filamentary Device
TFT	Transparent Field-Effect Transistor
UD	Ultra Definition
VBM	Valence Band Maximum
VCM	Valence Change Memory
XPS	X-ray Photoelectron Spectroscopy
XRD	X-ray Diffraction
ZTO	Zinc Tin Oxide

Abstract

Semiconductor oxides are promising materials that have made impressive progress in recent years, challenging the dominance of silicon not only in conventional devices including field-effect transistors but being amenable to next-generation electronic devices such as memristors. Although a variety of oxides have been explored, tin oxide has been an interesting material for researchers when offering p-type characteristics of tin monoxide SnO and n-type characteristics in tin dioxide SnO_2. While SnO_2 is easy to grow and well suited for a wide range of applications, it is difficult to form p-type SnO due to its metastability where it forms into the more stable phase SnO_2.

The work presented in this Doctoral Dissertation focus on exploring the characteristics and applications of energetically deposited tin oxide thin films. The tin oxide film deposited using high-power impulse magnetron sputtering was found to be mixed-phase nanocrystalline SnO and SnO_2 in which SnO_2 is dominant. The high resistivity, low carrier concentration and low mobility in the as-deposited and annealed samples hindered the application of the high-power impulse magnetron sputtering (HiPIMS) SnO_x in thin film transistors, however, suggested suitability for these films as a memristive material.

A small but quantifiable variation in film stoichiometry (Sn:O) resulting from the off-axis deposition led to the formation of two different types of memristive devices, namely filamentary and nanoparticle network memristors. Both devices exhibited stable volatile bidirectional resistive switching with a ratio between high resistance and low resistance of more than two orders of magnitude. However, their underlying resistive switching mechanisms and device characteristics were significantly different. Synaptic-like behaviours were observed on both filamentary devices (FDs) and nanoparticle network devices (NNDs), highlighting their potential for information processing in neuromorphic computing systems. While a FD can become only an individual cell in reservoir computing circuits, an NND can be implemented as a reservoir due to their available inter-connectivity which is required for reservoir computing.

Chapter 1:

Introduction

1.1 Context and objective

Owing to the wide variety of structural, optical and electronic properties that they exhibit, metal oxides have attracted significant attention from the research community. As electronic materials, metal oxides can offer transparency (wide bandgap), flexibility, applicability to conventional devices including field-effect transistors as well as novel characteristics suited to next-generation electronic devices such as threshold-switches and memristors. Among metal oxides, tin oxide is rare in offering p-type characteristics in tin monoxide SnO and n-type characteristics in tin dioxide, SnO_2. High-performance transistors with p-type SnO channels have been demonstrated while SnO_2 has applications including transparent conducting electrodes, transistor channels, gas sensors and more recently, has appeared in resistive switching devices.

This thesis describes a project aiming to contribute to the emerging field of metal-oxide electronic materials and more specifically, device applications of wide bandgap tin oxide. The thesis begins with a review of recent findings in the field of metal oxide electronic device materials, before describing experimental methods applied during the project. These include methods for energetic film growth and device fabrication as well as microstructural, optical and electrical characterisation. The tin oxide films produced during the project are discussed in detail, as are post-deposition treatments that were applied to alter their electrical properties. Following this, the memristive properties of tin oxide thin film devices and self-assembled nanoparticle network devices are reported. The carrier transport and switching mechanisms in the devices were studied and applications in pattern recognition were explored. These aspects of the work are also described in detail.

1.2 Research questions

The questions that this thesis aims to answer include:

- Are energetic deposition methods suitable for depositing thin films of either p-type SnO or n-type SnO_2?
- Can these films be treated post-deposition to alter/improve their electrical characteristics?
- What mechanisms within tin oxide enable it to exhibit resistive switching phenomena?
- Can tin oxide exhibit resistive switching characteristics other than those already reported?
- And can the transport and switching characteristics be selected by changing the stoichiometry and/or morphology of the tin oxide device layers?

1.3   Original contributions

The achievements and original contributions through the PhD research project are listed below:

- There are few studies on SnO_2-based memristors. In these, non-volatile switching behaviour was mainly observed. To the author's knowledge, volatile SnO_x based memristors have been reported only once before (in 2018). The investigation of switching mechanisms and memristive properties of the memristors fabricated in this work contributes to the growth of oxide memristive devices. In particular, the project work has included:
  - Identification of a previously unreported phase change switching mechanism in tin oxide. The resistive switching of tin oxide thin film memristors is attributed to Joule heating induced decomposition of the minority SnO phase and formation of a SnO_2 conducting filament with higher effective n-type doping.
  - Demonstration of current-controlled negative differential resistance (CC-NDR) in tin oxide memristors, necessary for 'selector' devices and memristive oscillators
- A facile, top-down method for assembling electrically-contacted, resistive-switching random networks is reported in this thesis. The random networks of nanoparticles were formed in ambient conditions at prescribed locations within thin films of mixed phase tin oxide. This selective formation was achieved simply by passing limited current between on-film electrodes with nanoscale separations. After the 'electroforming' process, the networks of nanoparticles exhibit bidirectional threshold switching in ambient conditions. Whilst similar effects have been reported in other nanoparticle or nanowire switching networks, low-temperature and/or low-pressure conditions are typically required.
- First direct comparison between filamentary memristors and nanoparticle network memristors formed in similar films. This work highlights the differing device characteristics and the differing switching mechanisms originating in films of slightly differing stoichiometry.
  - First realization of higher-order harmonic generation in tin oxide based memristors. Both filamentary and nanoparticle network memristors were formed in mixed-phase tin oxide films and respectively exhibited production of second- and higher- order harmonics.
- First report on implementation of SnO_x-based filamentary memristors and nanoparticle network memristors for information processing. This work shows the potential for tin oxide memristive devices to be exploited in neuromorphic computing systems including reservoir computing.

1.4 Thesis outline

This thesis describes the fabrication of tin oxide thin films, and tin oxide based memristors as well as discussing the resistive switching characteristics and implementation of these memristors. The structure of the thesis is outlined as follows:

Chapter 2 includes a literature review on the recent research on oxide semiconductor materials including SnO and SnO$_2$, memristive devices and reservoir computing.

Chapter 3 describes deposition methods of thin films and the experimental techniques used to fabricate and characterise the materials and devices.

Chapter 4 focuses on the structural, optical and electrical properties of tin oxide deposited using high-power impulse magnetron sputtering (HiPIMS).

Chapter 5 investigates the memristive properties of filamentary devices formed on tin oxide deposited using HiPIMS and their application to signal processing. Film and device characterization were employed to understand the underlying mechanism for the resistive switching observed in these devices.

Chapter 6 demonstrates self-assembled nanoparticle network devices fabricated on HiPIMS deposited tin oxide film and the potential applications of these devices including implementation of logic functions and reservoir computing.

Chapter 7 presents the comparison between filamentary memristors and nanoparticle network memristors formed in similar HiPIMS deposited tin oxide films, followed by a summary of the work and suggestions for further research.

1.5 Publications

- P. Y. Le, H. N. Tran, Z. C. Zhao, D. R. McKenzie, D. G. McCulloch, A. S. Holland, B. J. Murdoch and J. G. Partridge, "Tin oxide artificial synapses for low power temporal information processing", *Nanotechnology*, vol *30*, p.325201, 2019.
- H. V. Pham, P. Y. Le, H. N. Tran, T. J. Raeber, M. S. N. Alnassar, A. S. Holland and J. G. Partridge, "Temperature dependent electrical characteristics of rectifying graphitic contacts to p-type silicon", Semiconductor Science and Technology, vol. 34, no. 1, p. 015003, 2018.
- P. Y. Le, B. J Murdoch, A. J. Barlow, Z. C. Zhao, D. R. McKenzie, A. S. Holland, D. G. McCulloch and J. G. Partridge, "Resistive switching nanoparticle networks self-assembled from mixed phase tin oxide: formation and network characteristics", under preparation (see Appendix B).

Chapter 2:

Literature review

This chapter presents a brief summary of metal oxide semiconductors, their applications and the challenges faced in improving these materials. Tin monoxide and tin dioxide are discussed in more detail since these materials are central to the chapters that follow this one. Finally, memristors, and emerging device technologies are introduced.

2.1   Transparent Oxide Semiconductors (TOSs)

Transparent conducting oxides (TCOs) and transparent semiconducting oxides (TSOs) are challenging the dominance of silicon in a wide range of applications, such as displays, solar cells, multi-function windows, transparent, and flexible electronics [1-3]. Many studies have revealed that oxide semiconductors offer higher carrier mobility which leads to higher refresh frequency and higher resolution for traditional displays. They can also offer greater compatibility with new technologies such as organic light-emitting diodes (OLEDs) or three-dimensional (3D) displays [3-5]. A series of prototypes have been demonstrated; e.g. 1.46-inch diagonal active matrix (AM) liquid crystal display (LCD) driven by ZnO-based transparent field-effect transistors (TFTs) in 2006 by researchers from Kochi University, high quality small- and medium-size LCDs using Indium Gallium Zinc Oxide (IGZO) for smartphone and tablet terminals in 2012 by Sharp Corporation [6]. At the end of 2010, Samsung released a 3D Ultra Definition (UD) television with 70-inch diagonal and 240Hz resolution using oxide semiconductor TFTs [7]. Amorphous oxide semiconductor (AOS)-based transistors have also been formed on "electronic papers" from Toppan printing company [8] and on AM-OLED displays from the LGE group. Some examples for displays using oxide semiconductor based TFTs are shown in Figure 2-1.
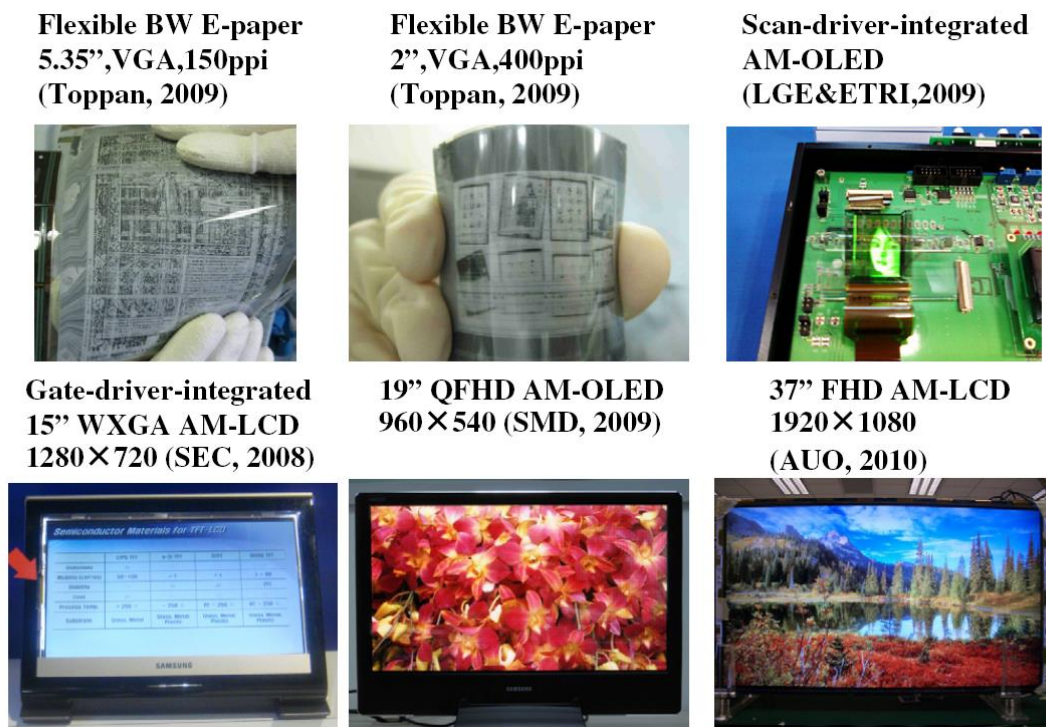
Figure 2-1: Some prototype displays using amorphous oxide semiconductor (AOS)-based transparent film transistors. Reproduced from [4].

Samsung demonstrated transparent liquid-crystal display (LCD) panels with no panel backlight and including TFTs fabricated from transparent oxide semiconductor materials. These screens utilize ambient light and consequently, consume 90% less electricity when compared with conventional LCD displays [9]. The future of transparent electronics seems promising. Displaybank has predicted that transparent displays will achieve significant growth (to $87.2 billion) by 2025 and surpass flat panel displays in 2030 [7], as shown in Figure 2-2.
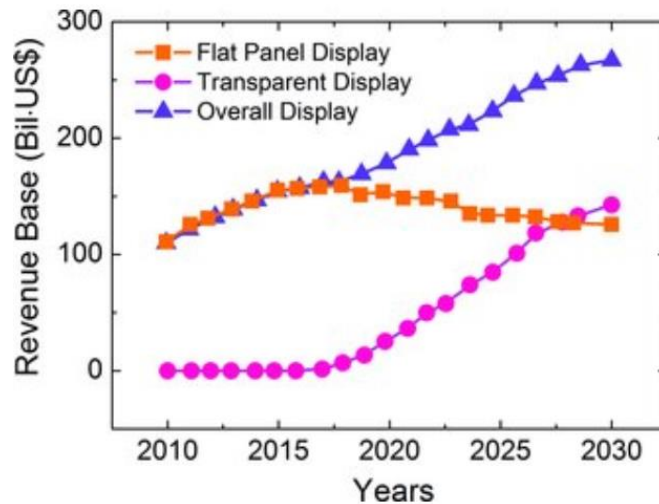
Figure 2-2: Global display market forecast by Displaybank in 2011. Reproduced from [7].

Besides display applications, transparent oxide semiconductors, typically fluorine-doped tin oxide (SnO_2:F) and metal-oxide/Ag/metal-oxide stacks like ZnO/Ag/ZnO, have been applied in architecture. Tin oxide coated windows have much lower thermal emittance of 15% compared to 84% for uncoated glass, enabling significant reduction in radiative heat loss [10]. These windows are called "low-e windows" and they are well suited for cold or moderate climates. Pyrolytic tin oxide coatings in heated glass freezer doors allow a small current to pass to defrost the doors. TOSs have been also used in solar control applications, photovoltaic cells, antistatic electromagnetic interference shields and electric heaters [1].

In summary, oxide semiconductors are promising materials which can be applied in many applications. However, the development and utilization of oxide semiconductors is inhibited by a lack of high-performance p-type oxide semiconductors. Hence, applications of oxide semiconductor materials are largely restricted to n-type unipolar devices. The ability to produce bipolar devices using TOSs would open up many more applications and this challenge has attracted significant attention from researchers in industry and academia alike.

2.1.1   N-type oxide semiconductors

Most oxide semiconductors are n-type oxides of post-transition metals such as Indium (In), zinc (Zn), tin (Sn) and Cadmium (Cd). In these oxides, the valence band is created by fully occupied p-orbitals of oxygen while the conduction band minimum (CBM) is composed of the unoccupied large-radius and overlapping spherical s-orbitals of metal cations, as illustrated in Figure 2-3. The direct overlap between metal ns^0 orbitals enables a facile pathway for electrons and the highly dispersive CBM gives rise to a small electron effective mass, leading to high electrical conductivity. These oxide semiconductors usually have a large optical bandgap and high transparency in the visible range.

In 1907, Badeker created cadmium oxide (CdO) by thermally oxidizing a film sputtered from Cd metal in vacuum [11], marking the dawning of TCOs. Although CdO has high carrier mobility [12, 13], the number of its application today is limited by its toxicity. After the advent of the first TCO film, oxide semiconductor materials have been studied and employed in a variety of applications. In World War II, antimony-doped tin oxide (Sb:SnO_2), was used in large-scale application as a transparent defroster for aircraft windshields [11]. Nowadays, due to its stability, SnO_2 is exploited as an electrode material in transparent electronics, displays, solar cells, smart windows and numerous other optoelectrical devices. Investigation on undoped tin oxide showed that tin interstitials mainly give rise to electron generation due to their defect states above the CBM while oxygen vacancies acting as shallow donors contribute minor generation. Sb-doped SnO_2 and F-doped SnO_2 are the most common doped SnO_2 materials [13, 14].
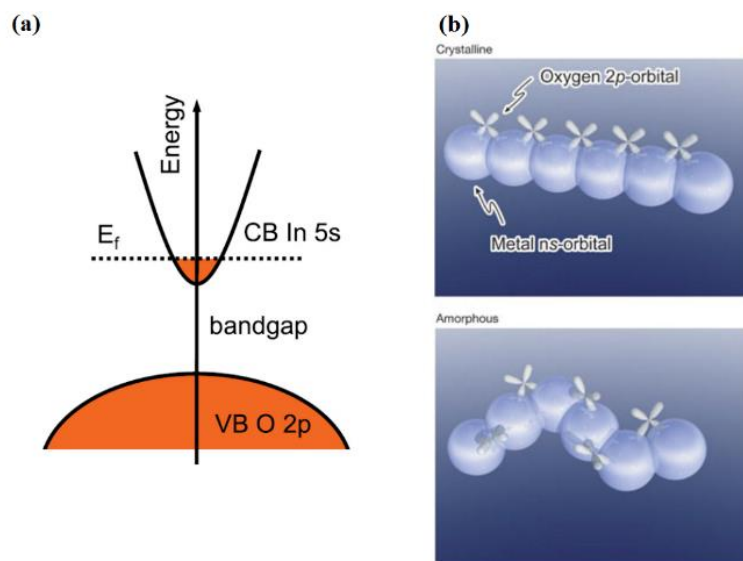
Figure 2-3: Schematic of the bandgap structure of Sn-doped In_2O_3 showing the In 5s derived conduction band (CB) and O 2p derived valence band (VB); (b) schematics showing orbitals for crystalline and amorphous oxides of post-transition metals. Reproduced from [2, 11].

Impurity-doped indium oxide (In_2O_3) semiconductors, including tin-doped In_2O_3 (ITO), indium zinc oxide (IZO) and gallium indium zinc oxide (GIZO) are the most favoured and successful TCO materials due to their high performance and stability [15]. In 1990, polycrystalline and amorphous In_2O_3 films were revealed to have similar electrical properties with high carrier density films ($N > 10^{20}$ cm^{-3}) by Bellingham et al. [16]. Moreover, amorphous TOSs have superior features such as low growth temperature, ease in deposition and etching for micro-patterning, and smooth surfaces [17]. Therefore, amorphous impurity-based In_2O_3 semiconductors have attracted significant interest from researchers and manufacturers.

Tin-doped In_2O_3 (ITO) is an n-type TCO where tin acts as a dopant in the lattice of indium oxide or replaces indium to be bound with interstitial oxygen [18]. ITO is of great interest for use in applications due to its wide bandgap resulting in high transmittance in the visible range, high carrier density and low resistivity [19-21]. The resistivity of ITO films was reported to be approximately $1.5 - 2{\times}10^4$ Ω.cm [17]. Lower resistivity values have been obtained using innovative growth methods such as high-density plasma-assisted electron beam evaporation or low-impedance, direct current (dc) magnetron sputtering [19, 22]. Optoelectronic devices such as photovoltaic cells [23], liquid crystal displays [24] and gas sensors [25] are examples in which ITO has been used.

The considerable contribution of zinc and gallium in impurity-based In_2O_3 materials prevents the crystallization of In_2O_3 which can easily occur at a temperature of approximately 150°C. Fully amorphous IZO films can be grown with a broad range of deposition conditions including substrate temperatures varying from room temperature to 600°C [26]. IZO films produced at room temperature were reported to have similar electrical properties to those of ITO films deposited at higher temperature [27]. Although IZO is a promising TCO material in TFTs or organic LEDs [28], its application as a TSO is limited since it is difficult to reduce its carrier density to below 10^{17} cm^{-3} [29]. The addition of gallium to ITO can alleviate this problem because Ga strongly binds with oxygen to prevent excessive free carriers created by oxygen vacancies [29]. With the addition of another cation, there are a wider variety of amorphous compositions offering useful electrical performance. IGZO has been applied in many industrial products such as in Sharp's LCD for smartphones and tablets [6]. The backplane display driver of Apple's iPad Air, using IGZO, consumes 57% lower power and delivers 23% higher contrast in comparison with the previous iPad which used amorphous Si [30].

Although impurity-based In_2O_3 materials have proven performance and demonstrated applications, the relative scarcity and price of In has been a strong motivator for research into alternatives such as zinc oxide (ZnO) [31-36], impurity-doped tin oxide (SnO_2), zinc tin oxide (ZTO) [37] and gallium zinc tin oxide (GZTO) [38, 39]. These oxide semiconductors provide properties close to those of impurity-based In_2O_3 but require more strictly controlled deposition conditions. Some n-type oxide semiconductors and their properties are reported in Table 2-1.

Table 2-1: Some n-type oxide semiconductors and reported properties

Film	Method a)	Substrate b)	Mobility (cm^2 /Vs)	Carrier concentration (cm^{-3})	T(%) c)	E_{opt} (eV)	Ref
InGaO$_3$	RFMS	Glass	10	10^{20}	90	3.3	[40]
ITO	PLD	YSZ	55	1.9×10^{21}	85		[41]
Cd$_2$SnO$_4$	RFMS	glass	32.3	7.4×10^{20}	90	2.97	[42]
In$_2$O$_3$	PLD	SiO$_2$/Si	119	3×10^{20}	90	-	[43]
ZnO	RFMS	Si	2	-	80	3.37	[44]
CdO	MOVPE	sapphire	20-124	2.6×10^{19} - 2.5×10^{20}	-	2.2	[45]
ZTO	FE	glass	18	2.96×10^{20}	-	3.3	[46]
IZTO	DCMS	glass	78	2×10^{20}	80	-	[47]
In$_2$O$_3$:H	ALD	SiO$_2$/Si	138	1.8×10^{20}	-	3.2	[48]
IZO	RFMS	glass	60	2.5×10^{20}	75	3.64	[49]
IGZO	HiPPMS	glass	140	$\sim 5 \times 10^{18}$	93	-	[50]
ATO	DCMS	glass	6	2.2×10^{20}			[51]
FTO	SP	glass	25	4.6×10^{20}	89	3.9	[52]
ZnO	RFMS	Si	2	-	80	3.37	[44]

a) Method: the deposition method employed for n-type thin films. (PLD: pulsed laser deposition; FE: flash evaporation. RF(DC)MS: radio-frequency (direct current) magnetron sputtering. R-SPE: reactive solid-phase epitaxy, SP: spray pyrolysis, ALD: atomic layer deposition)

b) Substrate: the substrate used in the Hall measurement. (YSZ: yttria stabilized zirconia; SiO$_2$: quartz.)

c) T%: Optical Transmission

2.1.2 P-type TCOs and TSOs

The success of n-type TCOs and TSOs, especially impurity-based In$_2$O$_3$ in commercial products, has driven research interest in p-type oxide semiconductor materials. P-type oxides with comparable performance to that of n-type oxides could extend the range and possibilities of transparent devices and circuits. If complementary metal oxide semiconductor (CMOS) technology using TCOs and TSOs became possible, the high-performance circuits currently based on non-transparent Si could be transferred to transparent and/or flexible substrate materials. Hence, an era of advanced transparent electronics would be opened. However, it is difficult to achieve p-type oxide semiconductor devices operating similarly to n-type counterparts because of limited carrier generation and the low mobility of positive carriers (holes) typically encountered. In contrast to the highly dispersed and delocalized CBM in n-type oxides which result in low electron effective mass and high electron mobility, the valence band maxima of p-type oxides are predominantly composed of anisotropic and localized *2p* orbitals of

oxygen (O). O atoms are small but have high electronegativity; hence the formation energy of the acceptors producing holes is high and a the effective mass of the holes is large [9]. Besides low performance, current p-type materials also suffer instability and irreproducibility [53, 54].

In 1997, Kawazoe et al. proposed the "chemical modulation of the valence band" (CMVB) concept to form p-type oxides by hybridizing O $2p$ orbitals with closed-shell Cu $3d^{10}$ orbitals [55]. The comparable energy level of Cu $3d^{10}$ is expected to overlap the O $2p^6$ level, and then the Cu cation creates covalent bonding with O ions which can delocalize the valence band maximum (VBM) [9]. This concept explains the high hole mobility achieved in cuprous oxide (Cu$_2$O), exceeding 100 cm^2/Vs [56]. However, the small separation between neighbouring Cu ions in Cu$_2$O causes d-d orbital interaction and hence, a narrow bandgap and colorization in Cu$_2$O. This problem can be solved by tetrahedral coordination of oxide ions in some layered structures, for example, in CuAlO$_2$ delafossite (also mentioned by Kawazoe). Since then, a series of p-type ternary Cu-bearing oxides such as CuMO$_2$ delafossites (where M = Al [55, 57], Ga [58], In [59], Cr [60], Y [61] and Sc [62]) and non- delafossite SrCu$_2$O$_2$ [63] have been reported. Layered Cu-chalcogen (Ch) materials (LaCuOCh, where Ch = S [64], Se [65]) and layered oxysulfide Cu$_2$Sr$_3$Sc$_2$O$_5$S$_2$ where chalcogens replace the oxygen to form a stronger hybridization with the Cu cation orbitals have also been proposed based on the extension of the chemical modulation concept. Layered copper oxides have wide bandgaps in the range from 3.1 eV to 3.79 eV [55, 61, 66-71] shown in Table 2-2. Nevertheless, they still have either low mobility or unsuitable carrier density which constrains their potential as p-type TSOs.

Spinel oxides ZnM$_2$O$_4$ (where M = Co, Rh, Ir) have been expected to become good candidates for p-type TOSs. These compounds consist of transition-metal cations (Co^{3+}, Rh^{3+}, and Ir^{3+}) with the d^6 configuration in an octahedral arrangement which behave similarly to closed-shell Cu $3d^{10}$ in Cu-bearing oxides when bonding with oxygen, because their low spin states can be considered as a "quasi-closed shell" configuration. ZnCo$_2$O$_4$ is the most common spinel oxide due to its potential in applications such as Li ion batteries and in photo- and electro-catalysis [11]. Rh and Ir are expensive to source for large scale industry applications. Some examples of spinel oxides ZnM$_2$O$_4$ are listed in Table 2-2.

Another method to obtain a high-performance p-type TCO or TSO is by forming oxides from metal cations which have pseudo-closed ns^2 orbitals such as Pb, Bi or Sn. This is because s states which have similar energy levels to the O $2p$ states can alleviate VB localization more effectively than d states. Hence, the VBM is more dispersed and holes have lower effective mass. While beryllium oxide Bi$_2$O$_3$ and tin monoxide SnO shows p-type conductivity, n-type conductivity was exhibited on lead oxide PbO [72-74].

Table 2-2: Some p-type oxide materials and reported properties

Film	Method a)	Substrate b)	T_{dep} (°C) c)	T_{PDA} (°C) c)	Mobility μ_{Hall} [cm²/V.s]	N_h [cm⁻³] d)	T [%] e)	Bandgap [eV]	Ref
CuAlO₂	PLD	Al₂O₃	700	–	10.4	1.3×10^{17}	60–70	3.50	[55]
CuGaO₂	PLD	YSZ	750	1215	0.8	1.0×10^{18}	–	–	[69]
Cu₀.₈₃AlO₂.₁₆	RFMS	Glass	500	–	0.82	1.5×10^{15}	–	–	[71]
CuAlO₂: CuO	RFMS	SiO₂	940	–	39.5	4.3×10^{15}	–	3.79	[70]
CuYO₂: Ca	TE	MgO	500	600	1	–	40–50	3.50	[61]
CuCrO₂: Mg	RFMS	SiO₂	600	600	1	–	50	3.10	[68]
LaCuOS	RFMS	SiO₂	RT	800	0.2	2.0×10^{15}	60	3.10	[67]
LaCuOSe	R-SPE	MgO	RT	1000	8	2.0×10^{19}	–	–	[66]
Cu₂O (111)	RFMS	Glass	600	–	256	1.0×10^{14}	–	–	[75]
Cu₂O	RFMS	Glass	RT	200	18.5	3.0×10^{13}	85	2.39	[76, 77]
Cu₂O	RFMS	SiO₂	RT	–	0.243	1.92×10^{19}	–	–	[78]
CuO	DCMS	Glass	RT	250	4.577	8.9×10^{17}	–	–	[79]
Cu₂O: N	FTS	Glass	RT	–	3.4	2.0×10^{18}	50	2.48	[80]
Cu₂O: Na	TO	–	1015	400–600	100	10^{13}–10^{16}	–	–	[81]
ZnRh₂O₄	PLD	Al₂O₃ & SiO₂	773	973	—	—	55	2.74	[82]
ZnIr₂O₄	PLD	Al₂O₃& SiO₂	773	973	—	—	61	2.97	[82]
ZnCo₂O₄	PLD	Al₂O₃ & SiO₂	773	973	—	—	26	2.26	[82]

a) Method: the deposition method employed for the p-type thin films. (PLD: pulsed laser deposition; TE: thermal evaporation. RF(DC)MS: radio-frequency (direct current) magnetron sputtering. R-SPE: reactive solid-phase epitaxy. FTS: Facing target sputtering. TO: thermal oxidation.)

b) Substrate: the substrate used in the Hall measurement. (YSZ: yttria stabilized zirconia; SiO₂: quartz.)

c) T_{dep} and T_{PDA}: Substrate temperature during deposition and post deposition annealing process. (RT: room temperature)

d) N_h: carrier concentration of the deposited film.

e) T: Optical transmittance of the deposited film

2.1.3   Tin dioxide (SnO₂)

Tin dioxide, also called stannic oxide, SnO_2 possesses a tetragonal rutile structure, in which each tin cation is surrounded by a slightly asymmetric octahedron of six oxygen atoms with bond-lengths of 2.023 Å (between Sn and two O in a same level plan) and 2.030 Å (between Sn and four O along an axis perpendicular with the plan). Each oxygen anion is bonded to three tin cations in a trigonal planar coordination, as shown in Figure 2-4. The lattice constants are a = b = 4.7374 Å and c = 3.1864 Å [83].
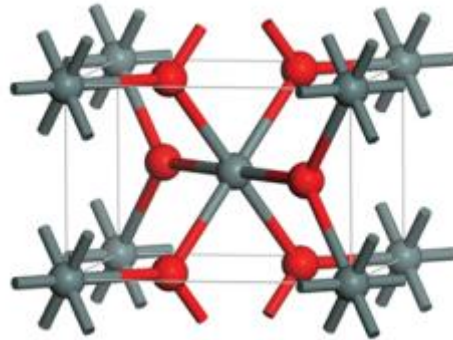
Figure 2-4: A unit cell of rutile-type SnO₂ where the grey and red spheres represent for tin cation and oxygen anion. Reproduced from [84].

With a wide direct bandgap of 3.6 eV [85], tin dioxide is highly transparent in the visible-light wavelength range (400-800 nm). Furthermore, the exciton binding energy of 130 meV [85] which is much higher than that of ZnO (60 meV [86]) suggests a promising candidate for optoelectronic devices. In the direct band structure of SnO_2, the bottom of the conduction band is composed by the empty Sn *5s* orbitals while mainly O *2p* orbitals and some Sn *s* and *p* states constitute the VBM [87]. The *s*-character of the CBM facilitates the overlap between orbitals of adjacent tin cation, thus providing a more conductive path for electron transport (as shown in Figure 2-3). Moreover, the electron effective mass is as low as $0.23-0.3*m_e$ (where m_e is the electron rest mass) [87]. As a result, high electron mobility can be achieved.

SnO_2 exhibits an intrinsic n-type conductivity which arises from shallow donor levels mainly produced by oxygen vacancies and tin interstitials. Typical properties of undoped SnO_2 films are high carrier concentration $N \approx 10^{19} - 10^{20} cm^{-3}$, low resistivity $\rho \approx 10^{-3} - 10^{-2} \Omega.cm$ and mobility $\mu \approx 5 - 30 cm^2/Vs$ [15, 88] which can reach 260 cm^2/Vs in single-crystalline SnO_2 [89]. However, it is usually difficult to control the concentration of these defects (i.e oxygen vacancies). Thermal annealing which reduces lattice mismatch effects and creates longer mean free paths for free electrons [85, 90] and impurity doping which increases dopant concentrations [91] are methods to increase the n-type conductivity of SnO_2. By doping with Sb, the resistivity decreases to $9.8 \times 10^{-4} \Omega.cm$ [92] or $5 \times 10^{-4} \Omega.cm$ [93] while

high visible spectrum transparency (88% and 95%, respectively) is maintained. With highly conductive and transparent properties, SnO_2 and doped SnO_2 materials are typical TCOs. Additionally, impurity-doped SnO_2 materials exhibit improved processability and environmental properties. Fluorine-doped SnO_2 is reported to be the TCO material with the highest work function, best thermal stability, best mechanical and chemical durability, best resistance to water and lowest fabrication cost [1, 94].

In 2004, Presley et al. [95] demonstrated a normally-off transparent thin film transistor consisting of a SnO_2 channel, indium tin oxide (ITO) electrodes and a superlattice of Al_2O_3 and TiO_2 (ATO) as the insulating layer (Figure 2-5). The transistor exhibits a maximum drain voltage close to 90 μA and an on/off ratio of 10^5 with the maximum field-effect mobility of ~0.8 cm^2/Vs. The average transmission of the device across the visible wavelength is ~75% (curve (b) in Figure 2-5). Higher performance enhance-mode SnO_2-based thin film transistors with the average field-effect mobility of 96.4 cm^2/Vs, an on/off ratio of 2.2×10^6 and capability to work at low voltages less than 4 V were reported by Hung et al [96].
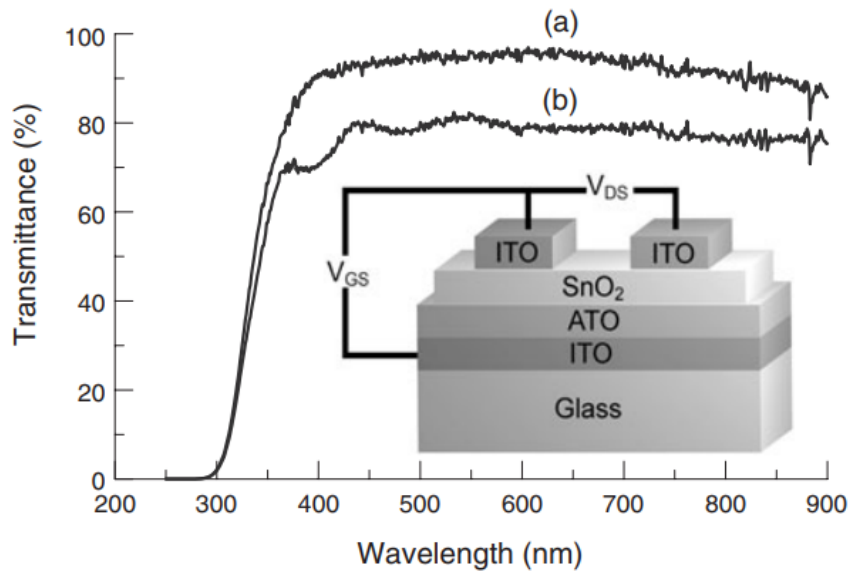
Figure 2-5: Optical transmission of the bottom-gate SnO_2 transparent thin film transistor (structure shown in inset). Reproduced from [95].

One of the most well-known applications of SnO_2 is in gas sensing, due to the high oxygen non-stoichiometry in SnO_2 lattice. SnO_2 sensors operate based on the change of resistance of the sensing layer with gas adsorption, where target gases have reduction-oxidation reactions with the surface of SnO_2. Under ambient conditions, oxygen from air is adsorbed, and then electrons in the conduction band near the surface region are immobilized by created surface acceptor states [97]. As a result, a depletion region is created and widened at the interface of the SnO_2 and the potential barrier at the

interface is increased as well. The presence of reducing or oxidizing gas will change the charge density near the surface, and in turn change the conductance of the sensing layer. SnO_2 layered devices have been employed to detect various gases, such as H_2 [98], O_2 [99], NO_2 [100, 101], CO [99, 102], ethanol [102, 103]. Additionally, multifunctional heterostructure geometries which have unique electron transfer or molecule absorption/desorption properties and thus improved sensitivity, stability and controllable selectivity can be developed by combining SnO_2 with various metal oxides [97, 100, 104, 105].

2.1.4   Tin monoxide (SnO)

Tin monoxide, also called stannous oxide, SnO possesses a litharge structure formed by layering tetragonal unit cells along the [0 0 1] crystallographic direction following the $Sn_{1/2}$-O-$Sn_{1/2}$ sequence, as illustrated in Figure 2-6. The Sn-O distance in SnO is 2.23 Å [14]. Its lattice constant has been reported in experimental and theoretical studies, as shown in Table 2-3.
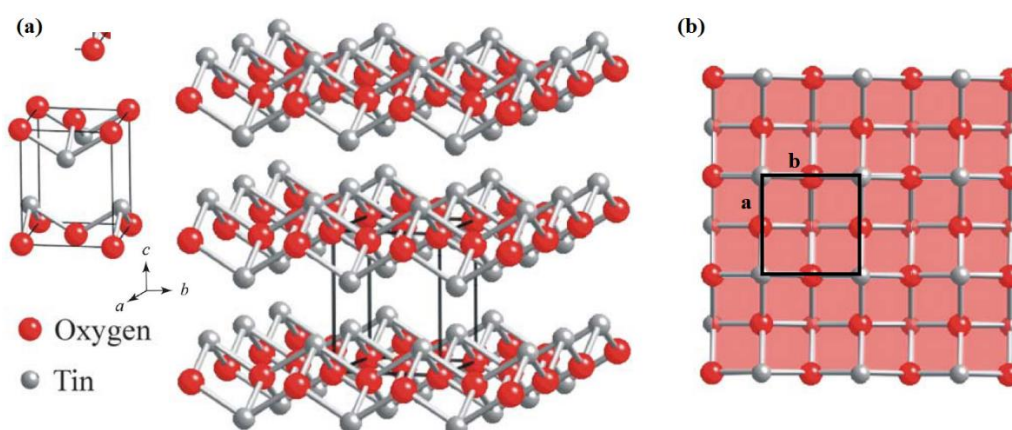
Figure 2-6: (a) The crystal structure of SnO; (b) Top view of SnO structure. Reproduced from [14].

The p-type nature of SnO is attributed to the dispersed VBM [106] and the formation of defects acting as native acceptors [107]. The top of the valence band results from the hybridization between Sn *5s* orbitals and O *2p* orbitals that have comparable energy levels as shown in Figure 2-7, hence the VBM is more dispersed and higher hole mobility can be obtained. Tin vacancies and oxygen interstitials are two candidates for p-type defects in SnO. Although having lower formation energy (2.37 eV [108]), interstitial O remains at the neutral state in the bandgap; hence it does not contribute to the electrical conductivity [107]. With a transition level observed at 0.39 eV above the VBM, tin vacancies result in p-type conductivity of SnO [108]. However, due to the high formation energy of a tin vacancy (5.25 eV [108]), it may not be the dominant mechanism for carrier formation. Unintentional impurities (e.g.

hydrogen) are more likely and can combine with tin vacancies to create complexes behaving like shallow acceptors [109].
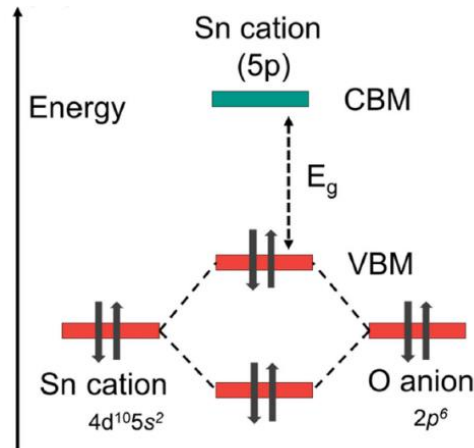
Figure 2-7: Schematic showing electron energy band structure of SnO with the hybridization between Sn 5s and O 2p orbitals. Reproduced from [9].

In polycrystalline SnO thin films, the accepter states were reported to have a slightly higher activation energy of 60 meV [110], when compared with accepter states in epitaxial SnO thin films (45 meV) [72, 111]. Increased barrier potentials at the grain boundaries in polycrystalline films reduce the hole mobility in the films [110]. The carrier mobility of SnO films also depends on the film orientation. According to Hsu et al. [112], the enhanced hole movement in the a-b plane give rises to higher hole mobility in c-axis oriented SnO films compared to the value obtained in (101)-oriented films. The increase of carrier mobility in p-type SnO thin films can be achieved by enriching Sn in the film composition since the films become more naturally metallic. That was confirmed by Granato et al. [113] and Caraveo-Frescas et al. [114] when they demonstrated that mixed phase thin films consisting of both SnO and Sn exhibited higher hole mobility than pure SnO films. The effective mass of SnO was reported to be $2.05*m_e$ (where m_e is the electron rest mass) [72] or more recently $2.6*m_e$ [108] for holes at the VBM, which is approximately ten times higher than the effective mass of electrons ($0.27*m_e$ [108]) at the dispersive CBM. SnO has both direct and indirect bandgaps. The direct bandgap varied from 2.6 eV to 2.78 eV as shown in Table 2-4 while the indirect bandgap was predicted to be in the range from 0.61 eV to 0.67 eV by hybrid DFT technique [115]. The low optical bandgap causes SnO thin films to absorb in the visible range.

Driven by the discovery of the p-type nature of SnO, SnO thin films have been grown with a variety of deposition approaches, such as electron beam (EB) evaporation, pulsed laser deposition, atomic layer deposition (ALD), and radio frequency (RF) magnetron sputtering using substrates and growth

temperatures as summarized in Table 2-4. However, due to the meta-stability of SnO, the deposition window to obtain pure SnO films is narrow. The chemical composition of the grown films strongly depends on the pressure, gas ratio, power, deposition and post-deposition annealing temperature. Small differences compared to the optimized conditions can lead to the coexistence of metallic Sn and/or SnO_2 with the SnO phase.

Table 2-3: Lattic parameters of SnO calculated in some studies

a = b (Å)	c (Å)	Type	Ref.
3.8029	4.8382	Experiment	[116]
3.7986	4.8408	Experiment	[117]
3.801	4.835	Experiment	[118]
3.797	4.6513	Computation	[119]
3.885	4.983	Computation	[107]
3.810	4.915	Computation	[120]
3.8989	4.9812	Computation	[121]
3.801	4.843	Computation	[122]

Ogo and co-workers reported the epitaxial growth of SnO thin films on (001) yttria stabilized zirconia substrates by employing pulsed laser deposition (PLD) [72, 111]. The substrates were heated up to 575 °C during the deposition process and annealed at 200 °C after deposition to obtain the epitaxial SnO films. The thin films presented the mobility and carrier concentration of 2.4 cm^2/Vs and 2.5 x 10^{17} cm^{-3} respectively. Caraveo-Frescas described a narrow window of deposition pressure and oxygen partial pressure (O_{pp}) to grow SnO thin films on lime-soda glass substrates [114]. As shown in Figure 2-8, the p-type polycrystalline thin films could be pure SnO or of mixed phase with the highest hole mobility of 18.7 cm^2/Vs obtained at 1.8 mTorr and 9% O_{pp}. Kim et al. [123] also demonstrated significant differences in the stoichiometry of their films which were estimated to vary from $SnO_{0.55}$ to $SnO_{1.08}$ under different oxygen pressure, as-deposited and post-annealed conditions.
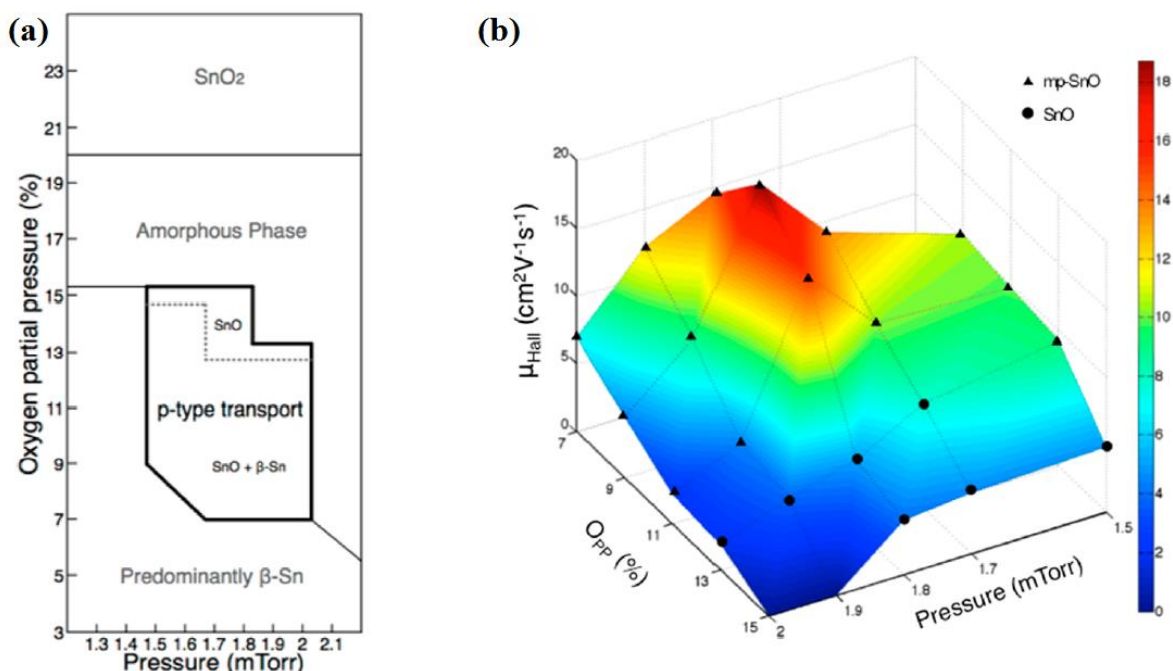
Figure 2-8: (a) Phase stability map to obtain p-type tin monoxide, showing a narrow window of deposition pressure and oxygen partial pressure; (b) Room temperature Hall mobility of the films deposited in the pressure range from 1.5 to 2.0 mTorr and 7% to 15% oxygen partial pressure, mp-SnO denote a mixed phase SnO. Reproduced from [114].

In 2008, Ogo et al. presented the first high performance p-type top-gate-structured TFT with PLD-deposited epitaxial SnO channel, PLD-deposited Al_2O_3 insulator layer and e-beam evaporated Au/Ni contacts (Figure 2-9) [111]. The threshold voltage, on/off ratio, field-effect mobility and saturation mobility were 4.8V, 10^2, 1.3 cm^2/Vs and 0.7 cm^2/Vs respectively. In 2010, a high-performance p-type SnO TFT demonstrated by Fortunato et al. [73] marked a milestone in the progress of p-type SnO as a commercially viable material when scalable magnetron sputtering was used for growth. The SnO films obtained after deposition and post-deposition annealing had a polycrystalline structure with hole concentrations in the range from 10^{16} to 10^{18} cm^{-3} and maximum hole mobility of 4.8 cm^2/Vs. A threshold voltage of -5 V, on/off ratio of 10^3 and field-effect mobility of 1.2 cm^2/Vs were obtained in their staggered bottom-gate TFT composed of a 30 nm SnO channel and Au/Ti contacts [73].
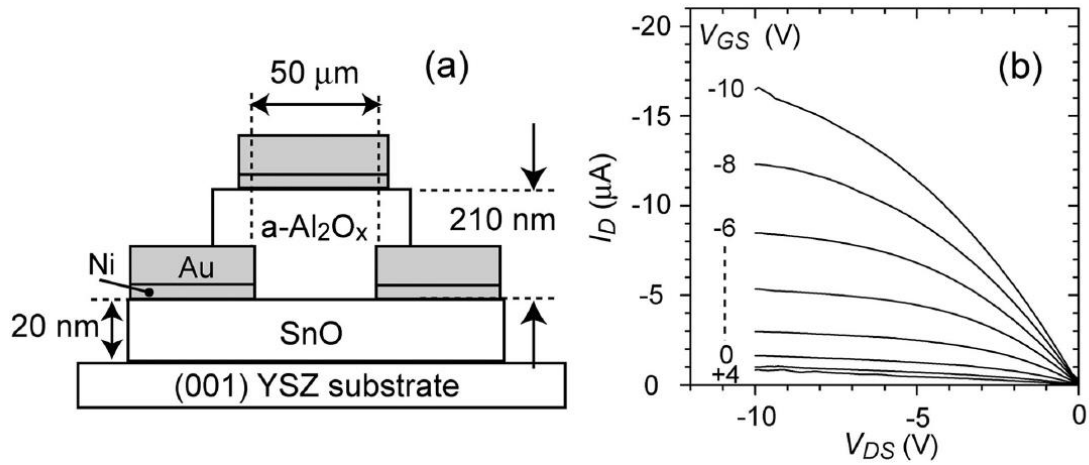
Figure 2-9: (a) Structure of a top-gate SnO TFT. b) Output characteristics. Reproduced from [111].

In 2011, the first SnO-based ambipolar TFT in which both electrons and holes were transported in the same channel under the applied gate bias voltage was demonstrated by Nomura et al. [124]. A 15 nm polycrystalline SnO channel was deposited by PLD and then treated by post-deposition annealing at 250^oC. SiO_2/Si and ITO were used as bottom gate/electrode and top contacts while an Y_2O_3 layer and a top gate were grown to form a dual-gate TFT. The ambipolar SnO TFT exhibited mobility of 0.81 cm^2/Vs for p-channel operation and 5×10^{-4} cm^2/Vs for n-channel operation. In addition to the aforementioned reports, there are several recent studies on pn-junction using SnO as the p-type layer [125-127] and CMOS inverters using p-type SnO TFTs [124, 128, 129].
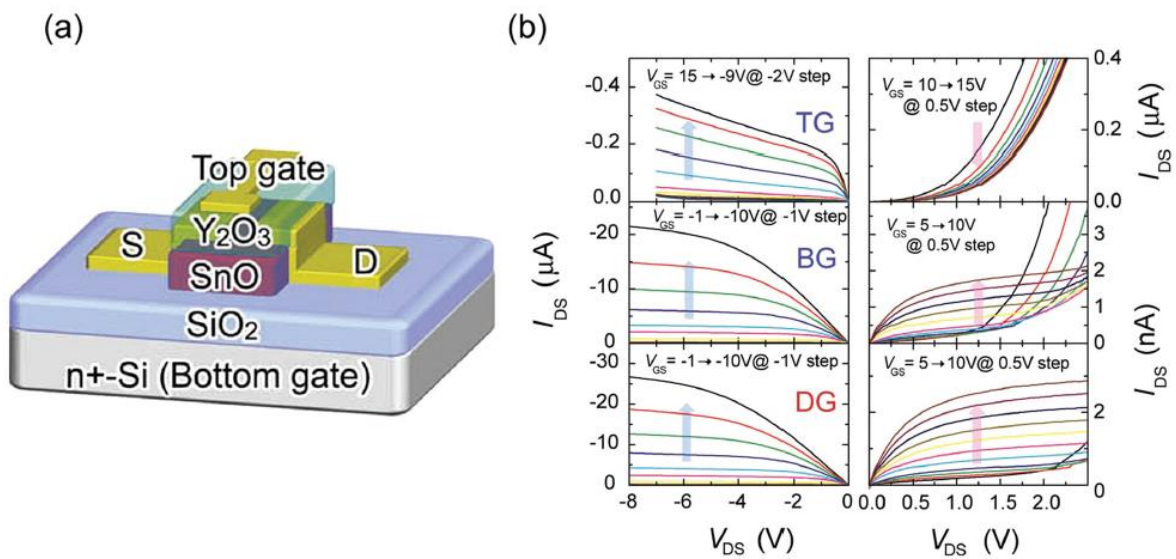
Figure 2-10: (a) Structure of an ambipolar SnO TFT. (b) Output characterisitcs of the TFT under p-channel (left) and n-channel (right) operation. Reproduced from [124].

Table 2-4: Summary of several reported tin monoxide SnO thin films.

Films	Method	Substrate	T_{dep} [°C]	T_{PDA} [°C]	Mobility	Carrier density	Transmittance	Direct Bandgap	Year	Ref
a)	b)	c)	d)	d)	μ_{Hall} [cm^2/Vs]	N_h [cm^{-3}]	[%]	[eV]		
ep-SnO	PLD	YSZ	575	200	2.4	2.5×10^{17}	–	2.70	2009	[72, 111]
pc-SnO	TE	Si/SiO$_2$	RT	310	2.83	5.0×10^{17}	70	–	2010	[130]
pc-SnO	EBE	SiO$_2$	RT	600	1.4	2.8×10^{16}	70	2.77	2010	[131]
pc-SnO	RFMS	Glass	RT	200	4.8	10^{16}–10^{18}	85	–	2010	[3, 73]
pc-SnO	PLD	Si/SiO$_2$	RT	250	1.9	1×10^{17}	–	–	2011	[124]
pc-SnO	EBE	Si/SiO$_2$	RT	350	3.9	5.6×10^{15}	60	2.70	2012	[132]
pc-SnO	DCMS	Soda-lime glass	RT	180	18.7	2.18×10^{17}	92	2.65	2013	[114]
pc-SnO	RFMS	Si/SiO$_2$	RT	250	3	1.0×10^{18}	70	2.78	2013	[133]
SnO	PLD	YSZ	575	–	7	1×10^{17}	–	2.60	2013	[106]
pc-SnO	RFMS	Glass	RT	300	3	7.22×10^{16}	–	2.71	2014	[134]
pc-SnO	PLD	Glass	RT	300	1.8	1.0×10^{19}	–	2.70	2014	[112]
pc-SnO	RFMS	SiO$_2$	200	–	3.34	2.3×10^{18}	60	–	2014	[127]
pc-SnO	ALD	Si/SiO$_2$	210	–	2.9	3.4×10^{17}	60	2.60	2014	[135]
pc-SnO	PLD	Si/SiO$_2$	500	–	2	9.0×10^{16}	–	2.68	2015	[136]

a) The crystal structure of the SnO. (ep: epitaxial; pc: polycrystalline.);

b) Method: the preparation method for the SnO thin films. (ALD: atomic layer deposition; EBE: electron beam evaporation; PLD: pulsed laser deposition; RF(DC)MS: radio-frequency (direct current) magnetron sputtering. TE: thermal evaporation.)

c) Substrate: the substrate used in the Hall measurement. (YSZ: yttria stabilized zirconia; SiO$_2$: quartz.)

d) T_{dep} and T_{PDA} : Substrate temperature during deposition and post deposition annealing process. (RT: room temperature)

2.2 Memristance, switching properties and reservoir computing

Solid state transistors have revolutionized our world by enabling the ubiquitous existence of compact, low–cost and high–performance electronic devices such as computers, mobile phones and home appliances. However, the transistor, as it is currently designed, is approaching limits in scaling and capabilities. New devices that offer higher density, higher speed and lower-power consumption are being sought in recognition of this. Owing to their simple structure, low power consumption and fast switching capabilities, memristors or memristive devices have emerged as promising building-block devices for next generation memory, computation and signal processing circuits [137].

2.2.1 A brief history of memristors

The concept of "memristor" (or memory resistor) was proposed by L. Chua in 1971. Based on symmetry, he proposed the existence of a fourth fundamental circuit element in addition to the three known classical two-terminal circuit elements, namely the resistor, capacitor, and inductor. A memristor is defined by the relationship between the magnetic flux (φ) and electric charge (q), called the memristance (M) [138]:

$$d\varphi = M.dq \tag{2-1}$$

A memristor therefore demonstrates unique properties which cannot be duplicated in any circuit built using combinations of the other three fundamental components [138].
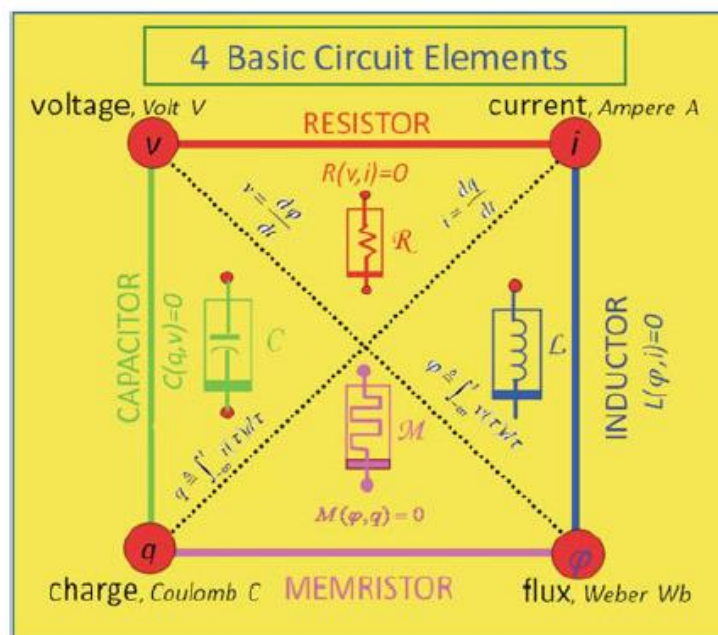
Figure 2-11: The four fundamental circuit elements. Reproduced from [139].

Later, in 1976, L. Chua and S. M. Kang proposed the models for memristive systems, defined by the following equations [140]:

$$\xi = F(\xi, x, t)$$
$$y = G(\xi, x, t)x \tag{2-2}$$

Where x denotes inputs (e.g. voltage or current), y denotes outputs (e.g. current or voltage, respectively) of the system. The function F describes how the internal state ξ evolves while the function G presents resistance or conductance of the system, respectively. Hence, a memristive model is a non-linear resistor whose state of resistance depends on both the history of input signals and time.

In 2008, a group of researchers from Hewlett Packard (HP) Labs claimed the discovery of the "missing memristor" by linking a practical model with the Chua's theory, although there were many reports of unrecognized memristance examples which preceded this work [139]. The prototype memristors were fabricated using of thin – film titanium dioxide TiO_2 as an insulator layer separating top and bottom platinum electrodes. With an analytic example, the memristance phenomenon was reported to occur naturally in nanoscale electronic devices [141]. Storing and logic processing properties including long retention time, fast, non-volatile and low power electrical switching were observed in the prototype memristors fabricated at HP Labs.

After this highly cited work, interest in memristors increased rapidly. Materials, fabrication, switching mechanisms, properties, applications and compatibility with or capability for replacing current CMOS technology have formed the basis for a significant body of work including papers, patents and books.

2.2.2 Resistive switching mechanisms

A memristor usually has a sandwiched metal – insulator – metal (MIM) structure with the device functionality originating in the insulating layer (also called active layer) (Figure 2-12). It exhibits a low resistance state (LRS) and a high resistance state (HRS) depending on the magnitude and/or polarity of the applied voltage (and electric field) and the length of time that the voltage has been applied. Once switched, a 'non-volatile' memristor may maintain its current resistance state for a long time in the absence of the applied bias [139, 142].

Although memristors have a simple structure, switching mechanisms which are responsible for resistive switching in memristor devices are complicated due to the chemistry of (electrode and insulation layer) materials [137]. Switching mechanisms can be broadly categorized into valence change, electrochemical metallization, phase change, thermo-chemical, ferroelectric [143, 144] and nanomechanical effects [145]. The first three classes (valence change, electrochemical metallization, phase change), the most commonly reported resistive switching mechanisms, will be described as following.
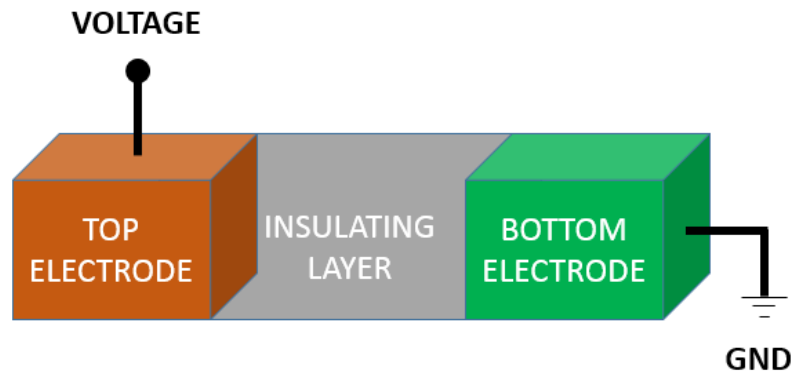
Figure 2-12: Schematic showing the metal – insulator – metal structure of a memristor.

The valence change memory (VCM) resistive switching mechanism relies on the migration of anion species under an external electric field [141]. The anion movement changes the local stoichiometry of the insulating layer, leading to the formation or rupture of conducting channels inside the insulating layer and between the two electrodes of the device, e.g. electrically conductive oxygen deficient Ti_4O_7 phase formation within an insulating TiO_2 layer [146, 147]. In most metal/metal-oxide/metal memristor devices, an electroforming process is required to generate initial conducting paths [137]. In general, electroforming involves applying a higher-than-usual electric bias/field across the two device terminals of the memristor. During this electroforming step, oxygen ions migrate leaving oxygen vacancies in the initially insulating active oxide layer [148].

The electrochemical metallization memory (ECM) resistive switching mechanism is based on the migration of metal cations which are dissolved from the interface of electrochemically active metal electrode(s) into the insulating layer. This mechanism is usually reported in MIM devices in which the insulator region is sandwiched between an electrochemically active electrode such as Ag or Cu, and an inert counter electrode such as Pt, Au, or W [149-151]. Dissolved metal cations are driven by external electric field and Joule heating to move toward the inert counter electrode, leaving behind metal vacancies. The movement of metal cations reduces the effective gap between two electrodes of the device, to gradually form conductive filament(s) and resulting in increased device conductance. Once the filament(s) connect the two terminals of the device, the device is switched from its HRS to its LRS. In order to switch the device back to the HRS, a negative voltage is applied to the active electrode. The existing metallic filament(s) is then ruptured/dissolved due to oxidation [137].

The phase change mechanism is based on phase transitions obtained by heating and quenching materials through Joule heating [139]. When subjected to an external electric field, phase change materials (e.g. $Ge_2Sb_2Te_5$ [152]) can switch between amorphous (high resistivity) and crystalline (low resistivity) states [152, 153].

2.2.3 Memristive materials

The VCM mechanism has been observed in most insulating metal oxide-based anion devices in which native dopants are believed to be responsible for resistive switching [154]. Insulating oxides can be viewed as semiconductors with native dopants, resulting from oxygen deficiency in n-type oxides such as TiO_{2-x} [147]) or oxygen excess in p-type oxides such as $Co_{1-x}O$ [155]. The movement of these native dopants under the co-existence of electric field and Joule heating give rise to chemical changes in the oxides, resulting in resistive switching. Theory and experiments [145, 156, 157] have demonstrated the role of oxygen vacancies and cation interstitials in device switching. However, more evidence is needed to determine the roles of other impurities, such as hydrogen, which are suspected to contribute to resistive switching [158, 159]. The switching materials of these anion devices include oxide insulators from simple binary transition metal oxides (e.g. TiO_2 [160], HfO_2 [161], NiO [162], Nb_2O_5 [163], SnO_2 [164]) to complex oxides including perovskites (e.g $SrTiO_3$ [165]).

Hafnium (IV) oxide HfO_2 is a frequently chosen material for memristive devices operating based on the VCM mechanism. This is due to their low-operating voltage, stability and wide operational temperature range [142, 166]. HfO_2-based RRAMs have been reported to exhibit desirable properties including simple fabrication, fast switching speeds, scalability (<10 nm), and compatibility with conventional complementary metal-oxide-semiconductor (CMOS) technology [167]. Taking as an example, a unipolar switching $Pd/Hf/HfO_2/Pd$ memristor (Figure 2-13) comprising an insulator layer HfO_2, an Hf capping layer (acting as oxygen getter) and top/bottom Pd electrodes, the VCM mechanism is discussed in detail. If the impact of impurities is neglected, a combination of hafnium and/or oxygen species (including atoms and vacancies) cause the resistive switching. In the "forming" process, under a high positive voltage applied onto the top Pd electrode, oxygen anions drift from the HfO_2 toward the Hf-capping layer, enhancing oxidation of the metallic cap (Hf) and leading to the generation of oxygen vacancies which form a conducting filament(s). From an energetic point of view, there is a transfer of oxygen vacancies from the anion electrode into the insulator layer, rather than a vacancy generation process [168]. The filament(s) bridge the top and bottom electrodes, resulting in a sharp drop of the device resistance as the device enters its LRS state. The concentration of the defects existing in the filament determines the carrier transport mechanism which can change from trap-assisted tunnelling, to Poole-Frenkel hopping and on to Ohmic conduction [168]. The device "RESET" operates based on local oxidization due to Joule heating and consequently, the existing filament(s) rupture when higher current passes through the device (Figure 2-13(b)). Many oxygen vacancies remain near the capping layer (Figure 2-13(c)), therefore the bias used to switch the device from HRS to LRS in "SET" operation is smaller than that initially required in the forming process.
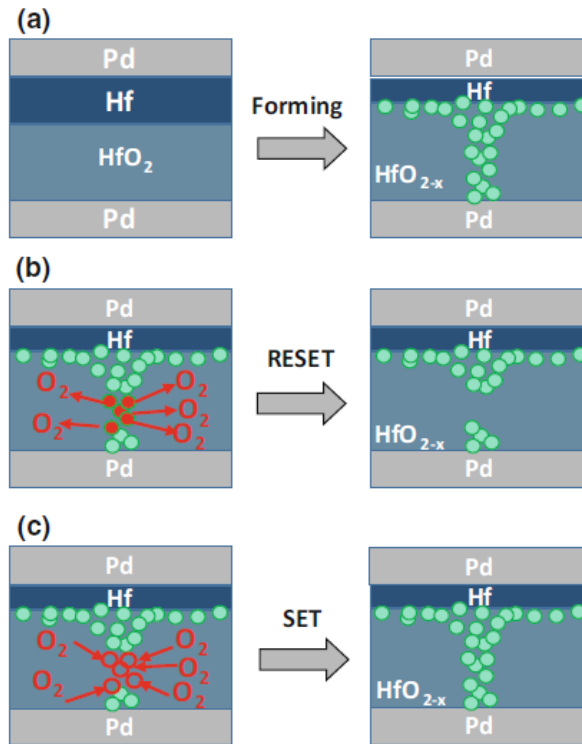
Figure 2-13: Schematics illustrate the Pd/Hf/HfO₂/Pd memristor and the formation and rupture during the device operation. Reproduced from [142].

ECM is the switching mechanism of devices in which metallic cations determine the device switching. Cation devices are required to have an electrochemically active material (e.g. Cu, Ag or alloys of these metals) and an electrochemically inert metallic electrode (e.g. Pt, W, Au) (discussed in section 2.2.2). The insulating materials for cation devices can be varied in a wide range from traditional electrolytes (e.g. Cu_2S [169], AgI [170], Ge_xTe_y [171]), to oxides (e.g. HfO_2 [172], SiO_2 [173], Cu_xO [174]) or others such as nitrides, amorphous Si, C or even vacuum gaps [175-178]. Using oxide materials as the active insulator layer increases the compatibility of cation devices with CMOS and enables implementation in some special applications such as non-volatile switches in large-scale integrated circuits [154]. In an Ag/H₂O/Pt device (Figure 2-14), some Ag atoms at the active electrode are oxidized to become Ag^+ cations when a positive high voltage is applied on the Ag electrode during the "forming" or "set" processes. The movement of these cations toward the counter electrode (Pt) is then driven by an external electric field and Joule heating. At the cathode, the electrochemical reduction of Ag^+ ions enables Ag atoms to be deposited on the surface of the cathode and grow towards the anode (Ag electrode). When the filament(s) created from Ag atoms reach the anode, the device enters its LRS. To switch the device off (HRS), a positive bias is applied on the Pt electrode. The Ag filament is then dissolved from the interface of the Ag electrode and Ag filament(s).
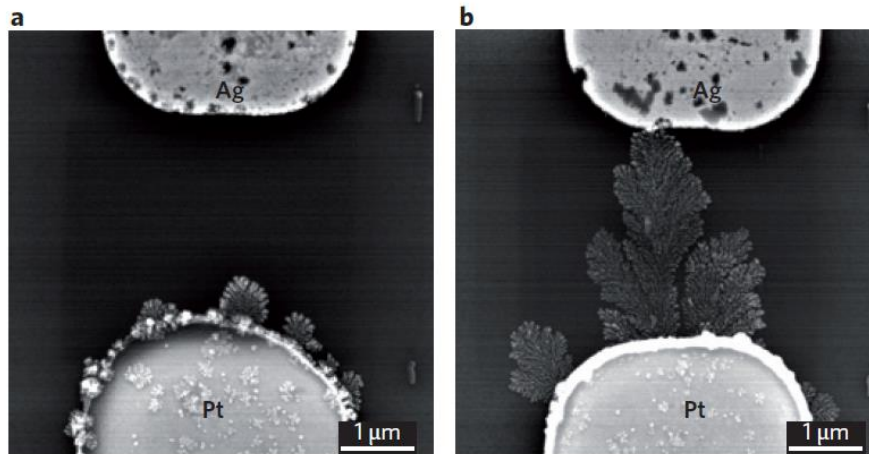
*Figure 2-14: Scanning electron microscopy images showing the Ag/H₂O/Pt device (**a**) in HRS with smaller and shorter Ag dendrites and (**b**) in LRS with longer and larger Ag dendrites. Reproduced from [154].*

The materials for the devices operating due to the phase change mechanism are required to exist in at least two structurally distinct solid phases. These can be an amorphous and one or more crystalline phases. Accompanying the change in phase are large structure differences that ensure the material exhibits significantly different optical and electrical properties. For example, the amorphous phase may have high resistivity and low optical reflection, in contrast to low resistivity and high reflectivity obtained from the crystalline phase. In the material MoO_x [179] for example, the metastable amorphous phase is transformed to the stable crystalline phase by heating the material above its crystallization temperature for a certain period. Melting the crystalline material and then quenching it sufficiently rapidly to obtain a solid amorphous state is the principle for the reserve crystalline-to-amorphous transformation. Phase changing materials include tellurium-based chalcogenides (e.g. $Ge_2Sb_2Te_5$ [153], GeTe [180]) and oxides (e.g. Ga-doped In_2O_3 [181], MoO_x [179]). Ogawa et al.[179] demonstrated a W/Mo-oxide/W device operating based on the phase change resistive switching property of molybdenum oxide. In the pristine state, the amorphous phase of the MoO_x layer exhibited high resistance. When a sufficiently high bias was applied, the device provided a more than five-orders-of-magnitude decrease in resistance which was maintained in the LRS. The amorphous-crystalline transition observed by transmission electron microscopy (TEM) image (Figure 2-15). A higher bias, enabling the occurrence of re-amorphization process, was used to switch the device back to its HRS.
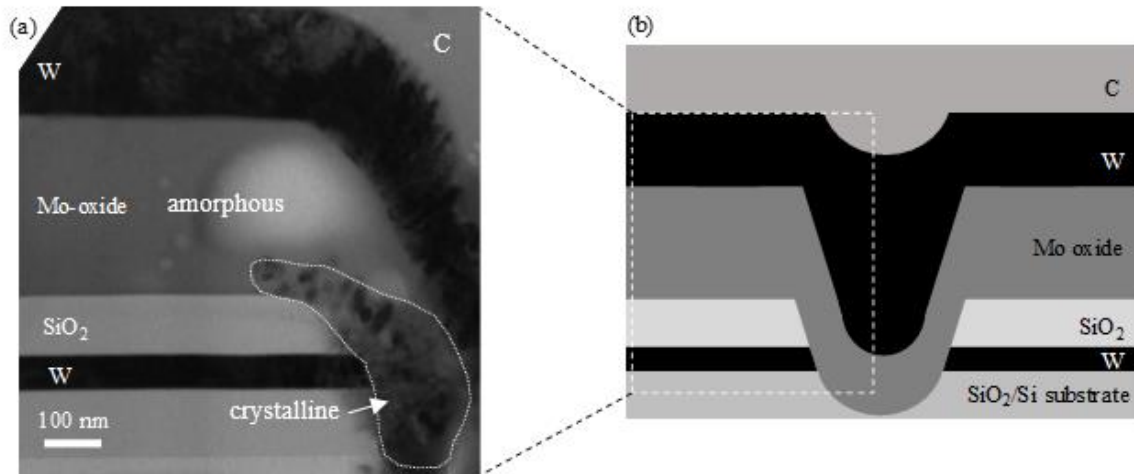
Figure 2-15: (a) Cross-sectional transmission electron microscopy (TEM) image of W/Mo-oxide/W and (b) schematic of the device structure. Reproduced from [179].

Tin oxide has received less attention as a memristive material than many other oxides. This is surprising since this low cost and nontoxic material [182-184] is rare among oxides in supporting n- and p- type behaviour depending on phase and this aspect is particularly promising as a potential memristive mechanism. In the reports published to date, resistive switching in tin oxide has largely been attributed to migration of inherent defects [183, 185-187]; the mechanism(s) involved have not been investigated thoroughly. The dependence of the switching mechanism(s) on stoichiometry (or the presence of minority phases) has not been investigated and given the tendency for tin oxide films to be oxygen deficient, is an important consideration. Nagashima et al. [183] studied the resistivity switching (RS) properties of memristor devices with tin oxide thin films deposited by PLD acting as the insulating layer, the Pt bottom electrode and the top electrode made from Ti, Ag and Pt. The devices exhibited unipolar non-volatile RS behaviour with a more than two orders of magnitude ratio of high resistance to low resistance (Figure 2-16(a)). Retention times and endurance were up to 10^4 s and 100 cycles, respectively (Figure 2-16(b) and (c)). Bipolar resistive switching characteristics were observed in resistive random-access memories based on an $Al/SnO_x/Pt$ structure [186]. The resistance ratio maintained itself at ~55/1 (HRS/LRS) for 100 endurance cycle. The device showed good stability and long retention time of 10^5 s. An $Ag/ITO/SnO_{2-x}/SnS/Mo$ RRAM with self-assembled SnO_{2-x} layer also demonstrated bipolar RS behaviour with a resistance ratio of 544/1 maintained for more than 100 cycles without degradation. The interface of the ITO and self-assembled SnO_{2-x} was thought to contribute to the RS properties of the device. To the author's knowledge, RS behaviour observed in SnO_2-based memristors has been non-volatile [185-187] and therefore more suited to memory storage, except in one report on $Au/SnO_2/FTO$ memristors by Pan et al. [164]. These latter devices exhibited volatile resistive memory and synaptic characteristics including short term potentiation, long term plasticity and spike rate dependent plasticity, suggesting suitability for artificial neural network applications.
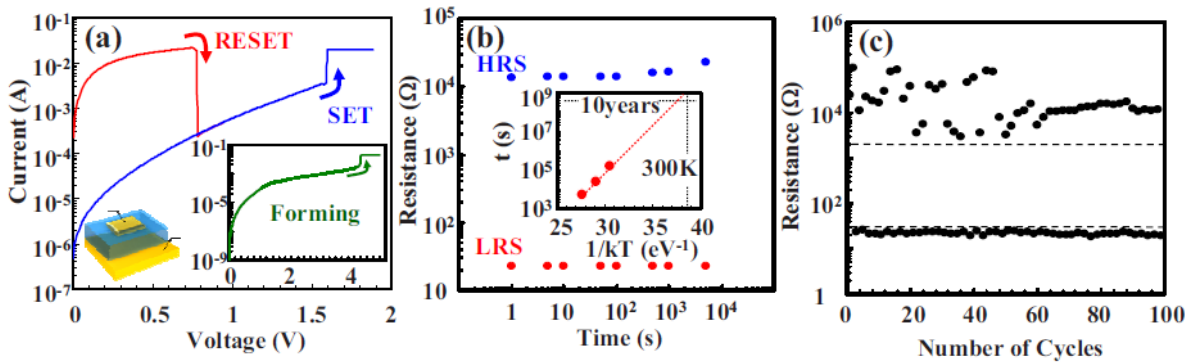
Figure 2-16: (a) Typical IV data of Pt/SnO₂/Pt with the inset showing the device electroforming data. (b) and (c) show the retention and endurance data of both LRS and HRS of the device. Reproduced from [183].

2.2.4 Activity-dependent plasticity in memristors

One of the most interesting and technologically significant aspects of memristors is their ability to emulate biological synapses. Biological memory storage and signal processing can be much more efficient than man-made circuits. Pattern recognition, involved in most every-day activities, is a notable example where biological processing is performed with massively higher efficiency than achieved in conventional computing. As a result, terms to describe biological memory are often useful in describing the characteristics of inorganic memristors. Several learning rules devised from the behaviour of biological synapses have been successfully demonstrated in memristive devices [188-190]. Hence, memristors are believed to be suitable for physical implementation of synaptic functions in neuromorphic circuits [139]. One of the most well-known synaptic learning rules is spiking-time dependent plasticity (STDP), also known as one of the Hebbian learning rules. This rule states that the synaptic 'weight' (ΔW – analogous to conductance) is a function of the time delay ($\Delta t = t_{post} - t_{pre}$) between the pre- and post-synaptic 'spikes' (or voltage pulses) [191-193] (Figure 2-17). Taking the most commonly observed asymmetric Hebbian learning rule as an example (Figure 2-17(a)), if the pre-synaptic spike arrives before the post-synaptic spike ($\Delta t > 0$), potentiation, represented by the increase of conductivity of the synaptic devices, will be induced. Otherwise if $\Delta t < 0$, depression, represented by the decrease of conductivity of the synaptic devices, will be induced. Different spikes and different type of synapses, excitatory or inhibitory leads to different form of STPD. The temporal order of pre- and post-synaptic spikes also determines the polarity of the synaptic weight change (Figure 2-17(a) and (b)).
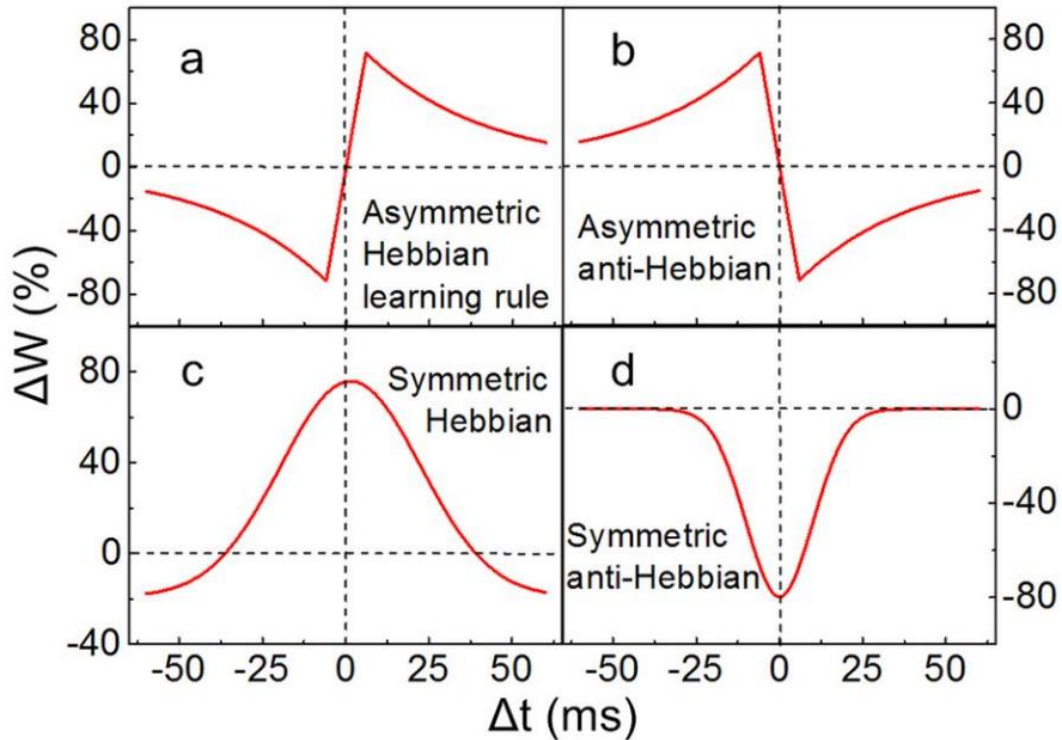
*Figure 2-17: Ideal STPD learning rules: (**a**) asymmetric Hebbian learning rule, (**b**) asymmetric anti-Hebbian learning rule, (**c**) symmetric Hebbian learning rule and (**d**) symmetric anti-Hebbian learning rule. Reproduced from [190].*

In addition to STDP, short-term plasticity (STP) and long-term potentiation (LTP) have been observed in memristive devices [194-196]. STP describes the phenomenon in which the conductivity of memristive devices rapidly decays to its original value (e.g. responding to HRS) when the repetition time between spikes is long. LTP is exhibited when the conductivity of memristive devices changed due to shortly repeated spikes [189]. The decay in LTP can occur after several hours or years [196]. A transition from STP to LTP can be obtained by the repeated stimulations at a high repetition rate. In contrast to LTP which is necessary for storing information, STP is suitable for information processing systems, enabling the release of information which is no longer needed.

2.2.5 Reservoir computing

As down-scaling in integrated CMOS technology approaches its fundamental limits, attention is shifting to computing by non-von Neuman and non-Boolean computing models [197]. Reservoir computing (RC) is a neural network-based computing model which can effectively process time-dependent inputs [198, 199]. An RC system consists of two parts: the first part, called the "reservoir", is connected to the input $u(t)$ and the second part, called the "readout", generates the final output $y(t)$ (shown schematically in Figure 2-18). In the reservoir, the connectivity structure is fixed, however, the network nodes or neurons will evolve dynamically with the temporal input signal. The dynamic evolution enables the

reservoir to perform a non-linear transformation from the input $u(t)$ to the new high-dimensional space (enhancing the separability), called reservoir states $x(t)$ [200]. To process empirical inputs, the reservoir is required to have a short-term memory which allows the determination of reservoir states from present inputs and inputs from the recent past. The reservoir states are analysed in the readout which is trained to produce the desired output $y(t)$ from the linearly weighted combination of the reservoir neural node value. Since training in RC focuses only on the connection weights W in the readout, learning complexity and training cost in RC are both reduced when compared with conventional recurrent neural networks (RNNs) [199, 201].
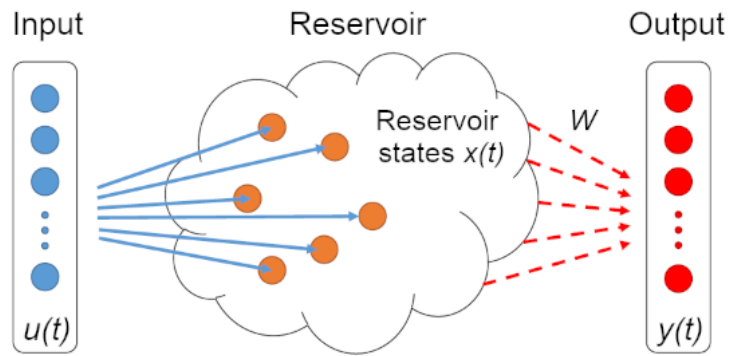
Figure 2-18: A schematic of an RC system.

RC has been reported in numerous studies and applications. Two well-known variants of RC are echo state networks (ESNs) and liquid state machines (LSMs) which were proposed by Jaeger et al. [202] and Maass et al. [203], respectively in the early 2000s. Various forms of RC have been implemented using analog circuits [198, 204], field programmable gate arrays (FPGAs) [205-207] and photonic systems [208]. Numerical modelling [197, 209, 210] has shown that networks of memristive devices can perform RC and predicted that memristive RC systems will exhibit high-performance in pattern recognition, signal processing and disease detection [200, 210-213]. In 2017, Du et al. [200] demonstrated a memristor-based RC in which the reservoir was not composed of a network of memristors but formed from a small group of independent memristors. An input signal was divided into multiple segments, each of which was transformed into an internal signal by the individual memristors. The internal signals were collected and acted as the reservoir state. Pattern recognition and time series prediction tasks were performed using this memristor-based RC.

Throughout this thesis, experimental evidence and discussions have been provided to explain the formation and mechanisms of resistive switching behaviour observed on energetically deposited SnO_x – based memristors. Device applications are also discussed in detail.

Chapter 3:

Deposition methods and characterisation techniques

This chapter discusses the experimental and simulation techniques used to fabricate, characterise and simulate the tin oxide films and devices investigated in this thesis. The deposition methods of thin film growth are described in the first section, followed by the brief summary of material and electrical characterisation techniques. Finally, the Technology Computer Aided Design simulation tool which is applied for thermal analysis of tin oxide devices is introduced.

3.1   Deposition Methods

3.1.1   Thin film deposition methods

A wide variety of thin film deposition methods exist from low quality film deposition techniques such as oxidation of metallic films, electrochemical deposition, sol-gel synthesis to high quality ones, such as molecular beam epitaxy (MBE), chemical vapour deposition (CVD), pulse laser deposition (PLD). The first group typically creates poor quality films reflected by low carrier mobility and moderate crystallinity but offers large coverage area. For the second group, either high growth temperature, low coverage area or high fabrication cost is a drawback.

Molecular beam epitaxy (MBE) is a thin film deposition technique in which high purity films can be grown. But its growth rate is lower than those of most other techniques. Chemical vapour deposition (CVD) has found widespread use for the formation of high-quality thin films of various materials. CVD has many derivatives i.e. metal-organic CVD (MOCVD), plasma-enhanced CVD (PECVD) and low-pressure CVD (LPCVD). The major drawback of CVD lies in the high deposition temperatures (200 – 1600°C [214]) which limits substrate selection. Furthermore, CVD processes often rely on highly toxic, explosive or corrosive precursors and produce hazardous by-products like CO or HF.

Pulse laser deposition (PLD) is one of the best methods to produce high quality thin films with low defect density. It is often considered as an energetic technique but the ionization degree in the depositing flux is much lower than either filtered cathode vacuum arc (FCVA) or high-power pulsed magnetron sputtering (HiPPMS). PLD is not preferred in industry due to its relative high deposition temperature, low coverage area and high production cost [215].

3.1.2   Thin film growth using HiPIMS deposition

Energetic deposition methods belong to a group of physical vapour deposition methods in which the depositing flux is partial or fully ionized. Diverse microstructure of the grown films can be achieved by controlling the energy of ions landing on the substrate surface via the applied substrate bias. In Ref. [216], Andre presented a diagram showing how energetic deposition can be used to obtain different film microstructures under the effects of three parameters, namely thickness (t*), normalised energy (E*) and generalised temperature (T*). The normalised energy is a combination of the pressure, displacement and heat effects caused by the kinetic energy of bombarding particles while the generalised temperature is calculated from the sample temperature and the heat effects arising from the potential energy of energetic particles. Energetic methods can be employed to grow several microstructure forms at low temperature, while similar structure films are achieved using conventional low-energy deposition methods at much higher temperature.
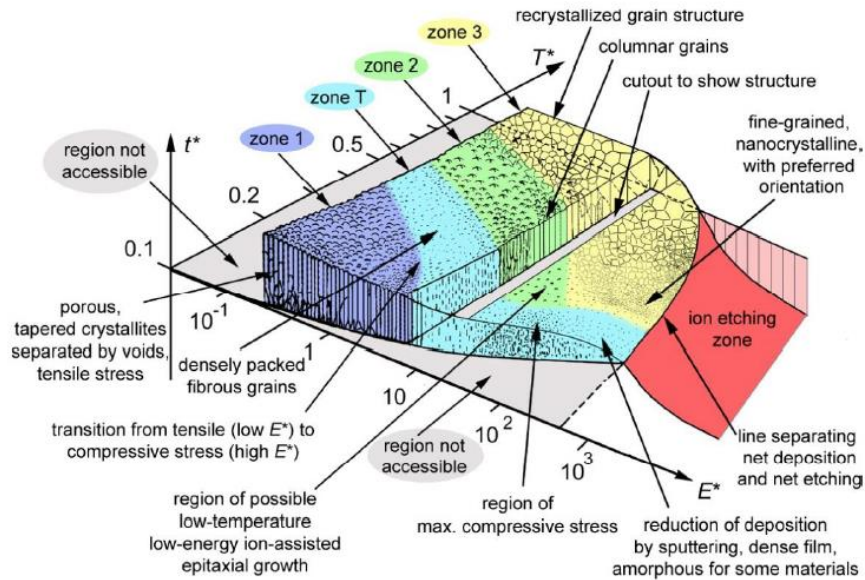
Figure 3-1: The structure zone diagram for energetic deposition of thin films devised by Anders. Reproduced from [216].

Magnetron sputtering, a type of physical vapour deposition (PVD), is one of the most frequently used thin film deposition methods. Magnetic fields are employed to enhance and confine the sputtering plasma close to the target. Positively charged ions in the plasma are accelerated and bombard the negatively charged target, leading to ejection of atoms from the target. The ejected (mostly) neutral atoms condense on a substrate to form a thin film. Magnetron sputtering systems, with direct current (DC) or radio frequency (RF) power, have been employed to form SnO films from a metallic Sn target with a mixture of argon and oxygen [73, 217], from a SnO target [127], or from a mixed phase SnO/SnO$_2$ target [218, 219]. The disadvantages of magnetron sputtering processes include low ionization efficiencies in the plasma, low deposition rates and substrate heating effects. Unbalanced magnetron sputtering [220] or high power pulsed magnetron sputtering (HiPIMS) [221] are variants which alleviate some of these problems.

The high-power impulse magnetron sputtering (HiPIMS) deposition method provides similar large-area/low-cost benefits to conventional magnetron sputtering but superior control over the structural and electronic characteristics of the deposited films due to its energetic, macro particle-free plasma [222]. The plasma has a greater ionization fraction due to the high-power pulses that are applied to the target (at low duty cycle to avoid melting). Due to the low duty cycle and because much of the energy goes into the generation of high ionization charge states [222], HiPIMS typically has a lower deposition rate than direct current (dc) or radio-frequency (RF) magnetron sputtering. This is a concern for mechanical coatings but not for very thin (< 100nm) active device layers. In reactive operation, the pulsed duty cycle in HiPIMS can be optimized to promote oxygen/nitrogen incorporation and ensure stoichiometric

oxides/nitrides [223]. HiPIMS is now a well-established production method for mechanical coatings [224, 225] and is finding increasing use as a method for producing electronic materials [226, 227].

In this project, tin oxide films were deposited onto SiO_2 (300 nm layer thickness on Si wafer) at room temperature using an AJA magnetron sputtering deposition system connected to a RUP-7 pulsed power supply. A Sn target (3-inch diameter, 99.99% purity) was operated in HiPIMS mode to grow tin oxide films (details in Chapter 4).
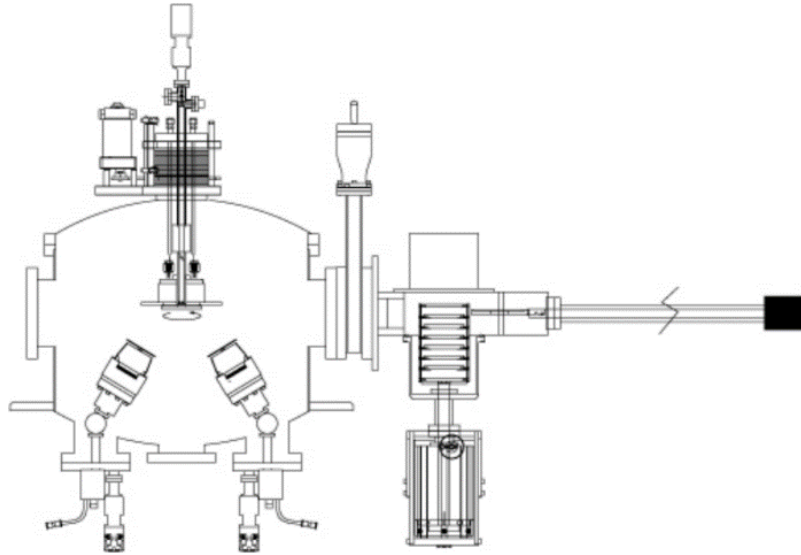
Figure 3-2: Diagram of HiPIMS deposition system courtesy of AjA Inc.

3.2   Structural Characterization

3.2.1   X-ray Diffraction (XRD)

XRD is a common tool for identifying and characterizing the crystal structure of materials. Based on constructive interference of X-rays diffracted from crystal plane within a sample, XRD can reveal atom spacing and preferred orientation (if any). The size, shape and internal stress of small crystalline regions can also be deduced from X-ray diffractograms.

X-rays generated by a cathode ray tube are filtered to produce monochromatic radiation which is collimated and directed toward the sample. The X-rays are scattered from atoms within the sample. Constructive diffraction occurs from crystalline regions (see Figure 3-3) and is described by Bragg's law:

$$n\lambda = 2d\,sin\theta \qquad\qquad (3\text{-}1)$$

where:
d: distance between atomic planes in a crystal
θ: incident angle
λ: wavelength of incident X-ray beam
n: an integer

By scanning the sample or X-ray beam through a range of angles, peaks in diffraction intensity are detected. The angular locations (2θ) of these peaks depend on the size and shape of the unit cell of the material. Their intensities are strongly influenced by the crystalline order in the sample.
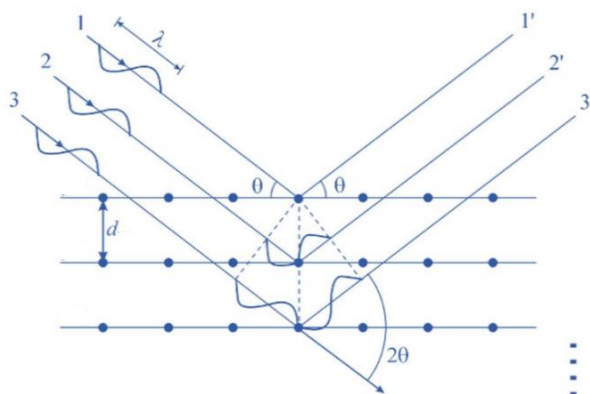
Figure 3-3: Reflection of X-rays by planes of atoms within a crystal. Reproduced from [228].

Average crystallite size of the scanned film can be calculated by using the Scherrer formula:

$$L = \frac{k\lambda}{\beta \cos\theta}$$

(3-2)

Where:
k: dimensionless shape factor with a value approximately equal to unity (typically k=0.9)
λ: wavelength of incident X-ray beam (in nm)
β: the full width at half maximum intensity (FWHM) of diffraction profile (in radians)
θ: Bragg angle (in degrees)

In this project, XRD was performed by using a Bruker D4 diffractometer. This instrument is equipped with Cu Kα radiation having the wavelength of 0.154nm.

3.2.2 X-ray Photoelectron Spectroscopy (XPS)

XPS is a standard tool for surface material characterization. Spectra are obtained by irritating a solid surface with a beam of X-rays whilst measuring the kinetic energy of photo-electrons emitted from the top 1-10nm of the material. The identification and quantification of all surface elements are determined by the energies and intensities of the photoelectron peaks illustrated in XPS spectra [228].

The kinetic energy (KE) of the electron, which is ejected from an atom or a molecule after absorbing an X-ray photon, depends on the photon energy (hv) and its binding energy (BE) (i.e. the energy required to remove an electron from the surface).

The binding energy of an electron depends on:
- The element and orbital from which the electron is ejected.
- The chemical environment of the atom from which the electron is ejected.

According to Gaussian/Lorentz peaks fitted to the XPS spectrum, elements and their chemical states in the scanned samples can be detected. The area under each peak is integrated to determine the ratio of the elements which present in the sample. The information can be obtained through survey and specific elemental scans while valence band scan provides an estimation of the gap between valence band and Fermi level of the sample material. The energy difference between the valence band maximum and the Fermi level located at 0 eV can be extracted by extrapolating the valence band edge to the background in XPS valence band spectrum [229].
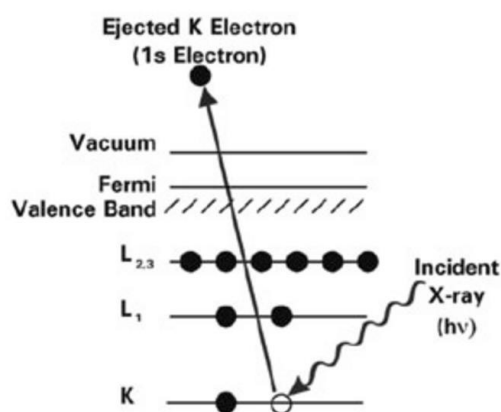
Figure 3-4: The photoemission process involved for XPS surface analysis. The discs and bars respectively represent electrons and energy levels within the material being analysed. The equation governing the process is: KE = hν – BE. Reproduced from [228].

In this project, XPS spectra analysis was carried out using a Thermo Scientific K-Alpha system equipped with Aluminum (Al) Kα mico-focused monochromators, an ion gun with energy range from 100eV to 4000eV for etching and a flood gun for charge neutralisation.

3.2.3   Auger Electron Spectroscopy (AES)

AES is a common tool for studying the material surfaces. In AES, a beam of energetic electrons with energies of 1-10 kV is produced by using an electron gun. When the sample is irradiated with this beam, core electrons are ejected and then a core hole is left behind. This core hole can be filled by an outer shell electron, causing an energy loss. Due to the principal of conservation of energy, another electron must be ejected from the atom and which can be analysed using a spectrometer. This electron is called Auger electron having a kinetic energy which is approximately equal to the difference between the energy of the core hole and the energy levels of two outer electrons [230]. Therefore, analysis of Auger electrons can yield surface compositional maps and depth composition profiling of the sample's surface.

In this project, AES was performed on a PHI 710 Scanning Auger Nanoprobe (SAN) (Physical Electronics, Chanhassen, USA) utilising a field emission electron source and a coaxial single pass

cylindrical mirror analyser for electron energy analysis. The source was operated at 10 kV, 1 nA for spectroscopy and microscopy.

3.2.4 Electron Microscopy

Electron Microscopy (EM) used for forming images is a powerful tool for visualizing and analysing specimens at the microscale and nanoscale. By using a beam of high energy electrons that have much shorter wavelength (100,000 times) than those of light [231], EM offers detail inaccessible by light microscopy. This tool also enables the investigation of crystal structures, specimen orientations and chemical compositions of phases, precipitates and contaminants through electron diffraction pattern, in-situ X-ray and electron-energy analysis.

A scanning electron microscope (SEM) is a typical electron microscope that enables identification of chemical elements and elemental quantification, illustration of the surface topology and detection of micro-scale defects. In an SEM, an electron beam is electromagnetically scanned across the sample and generate signals when it strikes the sample. The signals can be secondary electrons which escape from the sample after the strike of the primary beam or backscattered electrons which are from the primary beam and backscattered 180°. A secondary electron typically has much lower energy, compared to the primary electrons [232] while the intensity of backscattered electrons depends on the atomic weight of the sample material [233]. Either secondary electrons or backscattered electrons are used to produce image/spectra of a sample's surface.
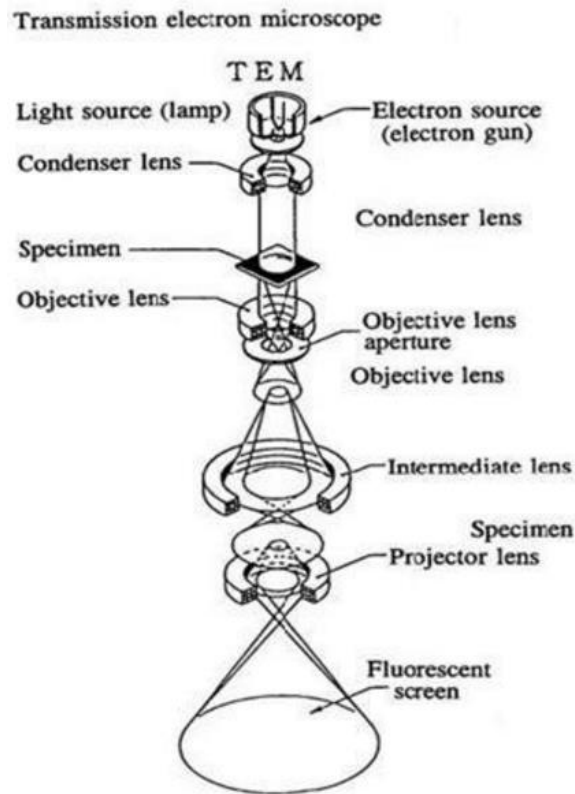
Figure 3-5: General layout of a TEM describing the path of electron beam in a TEM. Reproduced from [234].

In a transmission electron microscopy (TEM), electrons, emitted from an electron source at the top of the microscope, are concentrated into a very thin beam through electromagnetic lenses. The electron beam is transmitted through the specimen being investigated. Depending upon the thickness and electron transparency of the sample, some of the electrons are scattered. Electrons are then collected by other lenses for zooming or contrast enhancement before striking a fluorescent screen to create an image. The darker regions of the image are from regions of the sample passing no or few electrons while the lighter parts of the image are from regions of a sample where more electrons were transmitted through. Contrast in the image therefore provides information on the structure, texture, shape and size of the sample.

3.2.5 Atomic force microscopy (AFM)

Atomic force microscopy is used to reveal the surface morphology of scanned samples based on measuring the force between its sharp tip and samples. The 3-6μm tall pyramid tip is a part of a flexible cantilever which is attached to one end of a piezoelectric tube. The piezoelectric tube horizontally and vertically adjusts the position of the cantilever based on the applied voltage at its electrodes. A laser diode creates a highly dense laser beam which is directed toward the cantilever. The position of the laser spot on a four-segment photo-detector which the reflected beam strikes indicates the angular deflection of the cantilever. A feedback loop operates with the attempt to keep the cantilever deflection

constant. As the tip scan over the sample surface, a height map of the sample is generated. Not only the root mean square (RMS) roughness of the surface of the film can be reported by using AFM, but the grain size of the film surface can also be estimated. Macro scale defects presenting during the deposition process or treatment can be observed.
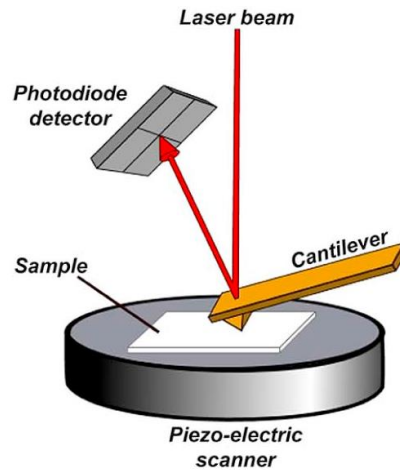
Figure 3-6: General schematic of AFM. Reproduced from [235].

A Veeco Dimension 3100 Scanning Probe Microscopy (SPM)/AFM and an Asylum Research MFP-3D Infinity atomic force microscope were employed to analyse the morphology of deposited thin films in this project.

3.3 Electrical characterisation

3.3.1 Hall Effect measurement

The Hall Effect measurement is a simple method to determine the carrier density, mobility and resistivity of a semiconductor. It is widely used in industry and research laboratories due to its simplicity, low cost and fast turnaround time. The basic principle of the Hall Effect is the Lorentz force, consisting of electric force and magnetic force. When an electron moves along the electric field direction which is perpendicular to an applied magnetic field, a magnetic force $-qv \times B$ acting normal to both electric and magnetic field is generated. As a result, the Lorentz force is determined by $-q(E + v \times B)$ where q is the elementary charge, E is the electric field, v is the electron velocity and B is the magnetic field. This force makes an electron drift away from its original direction, and hence creates an excess of negative charge on one side of the sample. This charge leads to a potential drop across two sides of the sample, known as the Hall voltage (V_H). The carrier density can be obtained from the equation:

$$n_s = \frac{I \times B}{q|V_H|}$$

(3-3)

where I is the current through the sample.
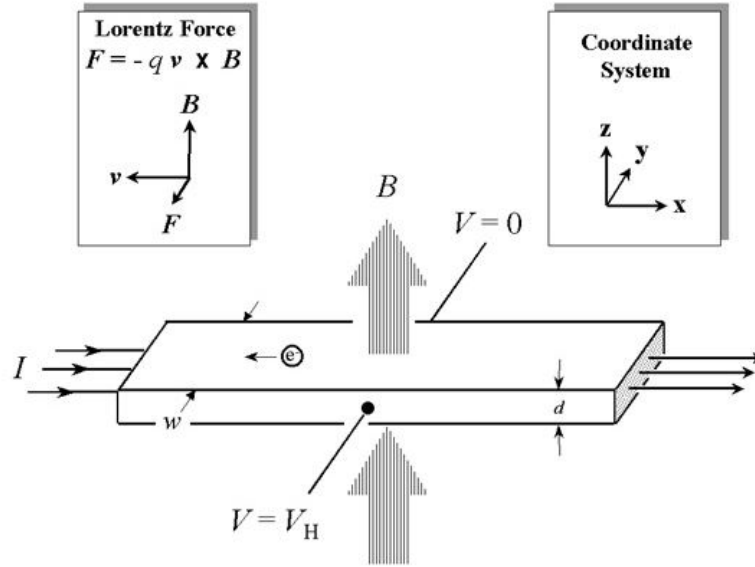
Figure 3-7: Schematic showing the Lorentz force in an n-type bar-shaped semiconductor. Reproduced from [236].

The sheet resistance of the sample can be determined by the Van der Pauw resistivity measurement method. In order to carry out the Van der Pauw measurement, four small ohmic contacts are placed on the periphery (corners are preferred) of the sample. Resistances R_A and R_B are calculated from the voltage applied at two adjacent contacts and the current passing through the other contacts is measured as shown in Figure 3-8.

These resistances are related to the sheet resistance R_S through the Van der Pauw equation

$$e^{-\frac{\pi R_A}{R_S}} + e^{-\frac{\pi R_B}{R_S}} = 1 \tag{3-4}$$

R_A and R_B are known, so R_S can be solved. The electrical resistivity ρ is calculated by:

$$\rho = R_s \times d \tag{3-5}$$

where d is the thickness of the measured conducting film (sample).

From the carrier density (Hall Effect measurement) and resistivity (Van der Pauw measurement), the carrier mobility can be determined by:

$$\mu = \frac{|V_H|}{R_S IB} = \frac{1}{q n_S R_S} \tag{3-6}$$

In this project, a Dynavac coating system was used to form ohmic contacts for SnO_x films while an Ecopia HMS 3000 system with fixed 0.55T magnetic field was used for Hall measurements.
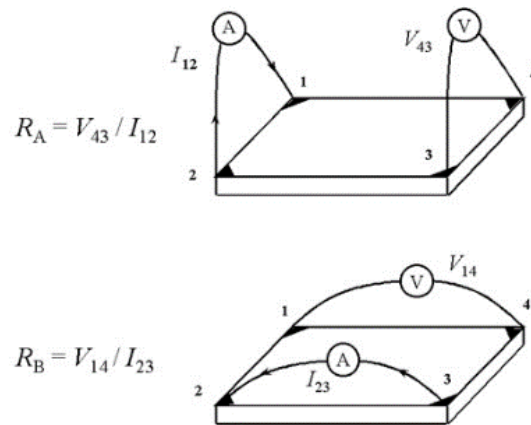
Figure 3-8: Schematic showing Van der Pauw resistivity measurement setup. Reproduced from [236].

3.3.2 Current-voltage measurements

Current-voltage (I-V) characteristics of a device, the relationship between the current flowing through the device and the DC voltage across its electrodes, identify its behaviour in an electrical circuit. Performance of the device significantly depends on its basic parameters such as structure or material properties, hence I-V measurements enable engineers to determine important parameters of the device.

I-V measurements are carried out with a probe station and a source-meter. Electrical contact to the device is with needle probes. When biases are applied to electrical contacts of the device, the current flow is measured, and then its I-V characteristics are achieved.

A Keithley 2400 SourceMeter SMU instrument with the lowest current capability of 1pA and accuracy of 0.02% was employed for I-V measurement in this project. A temperature-controlled microscope stage (Linkam Scientific) enabled measurements to be performed at temperatures down to 90K. This is particularly useful for oxides semiconductors as the temperature dependence of their resistivity is indicative of their charge transport mechanisms.

Chapter 4:

Structural and electrical characterization of energetically deposited tin oxide thin film

In this chapter, the deposition tin oxide using high power impulse magnetron sputtering (HiPIMS) is described. Following this, structural, optical and electrical measurements are provided and discussed. The aim of this work was to determine the structural and electrical characteristics of HiPIMS deposited SnO_x before exploring device applications for the material.

4.1 Introduction

Metal oxides have emerged as potential materials for a wide-range of next generation electronic devices including those required for transparent and flexible circuits [1, 3, 5]. While n-type oxides with high performance have been developed, the growth of p-type oxides lags behind due to limited carrier generation and the low mobility of positive carriers. However, p-type oxides with comparable performance to that of n-type oxides are necessary to broaden the applications possible with oxide semiconductors.

Oxides of tin, mainly including tin monoxide (or stannous oxide) SnO and tin dioxide (or stannic oxide) SnO_2 have attracted interest from researchers for several decades. While SnO_2 exhibits an intrinsic n-type conductivity, SnO exhibits inherent p-type characteristics. High conductivity, high mobility, sensitivity to various gases and memristive behaviors enable SnO_2 to be employed in a wide range of applications from transparent conducting electrodes and transistor channels to gas sensors and neuromorphic electronic devices including memristors (discussed in section 2.1.3). The development of SnO in electronics typically focuses on improving performance of SnO-based transistors. Although high performance p-type SnO has been obtained (discussed in section 2.1.4), SnO still suffers a narrow deposition window due to its meta-stability which tends to cause coexistence of either metallic Sn or SnO_2 along with the SnO phase. Both SnO and SnO_2 films can be fabricated using various deposition techniques such as pulsed laser deposition (PLD) [111, 124, 237], atomic layer deposition [135, 238], radio frequency (RF) or direct current (DC) magnetron sputtering [95, 114, 127].

In this chapter, the structural, element composition and optical properties of SnO_x thin film deposited at room temperature by high power impulse magnetron sputtering (HiPIMS) are described. Electrical measurements were carried out to determine whether the SnO_x thin film could be incorporated into functional electronic devices.

4.2 Experiment

The SnO_x film was deposited onto SiO_2 (50 nm layer thickness on 4-inch Si wafer) at room temperature using an AJA magnetron sputter deposition system equipped with a RUP-7 pulsed power supply (Figure 3-2). Prior to deposition, the system was pumped to a base pressure less than 1×10^{-6} Torr. During deposition, Ar and O_2 were injected to the system with the ratio 1(Ar):3(O_2) to maintain the process pressure of 6.0 mTorr. The substrate potential floated (at ~10 V) during the 20 min deposition. The Sn target was 3-inches in diameter, 99.99% purity and was operated in HiPIMS mode with pulse amplitude, width and frequency of 635 V, 100 μs and 100 Hz, respectively. The waveforms of HiPIMS voltage (blue) and target current (green) are shown in Figure 4-1, together with the trigger pulse from the signal generator (yellow) and the substrate current (pink). Since the RUP-7 is designed to deliver a current while maintaining the pre-set output voltage, it has an output inductance. This output inductance and small output capacitance causes the ringing at the start of the voltage pulse which persists whilst there is no load prior to plasma ignition. The current onset at 25 μs is associated with plasma ignition. This delay of current onset is typical for HiPIMS systems and is well described by Anders [239]. Following plasma ignition, the target current significantly increases to reach a peak of 6.69 A in approximately 25 μs before it reduces in the last 40 μs. This can be explained by gas rarefaction (due to the gas in the vicinity of the target surface is heated) leading to a small gas ion flux to the target and lower current [239].

Figure 4-1: The HiPIMS voltage, current waveforms used for the SnOₓ thin film deposition.

The reactive deposition process produced a film which varied in thickness from 20 nm at the O-rich region to 50 nm at the Sn-rich region. Following deposition, the wafer was diced into 10×10 mm^2 samples (Figure 4-2) for structural/electrical characterization and device fabrication. The surfaces of the films were mapped in tapping mode using an Asylum Research MFP-3D Infinity atomic force microscopy (AFM). A Bruker D4 x-ray diffraction (XRD) system with Cu K-α (8.048 keV) source and Bragg–Brentano configuration was employed to characterize the crystallinity of the films while their composition was investigated using a Thermo Scientific K-Alpha system equipped with an Al Kα (1487 eV) mico-focused monochromator. The optical properties of the films were determined using an Oscillator model to fit spectroscopic ellipsometry data.

After microstructural and optical characterization, four Van der Pauw corner contacts were thermally evaporated onto the diced SnO$_x$ samples. Hall Effect measurements were performed on these samples at room temperature using an Ecopia HMS 3000 system with fixed 0.55 T magnetic field.
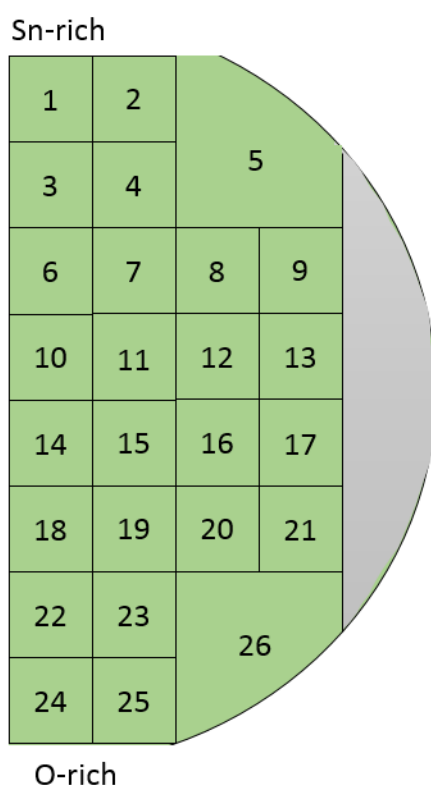
Figure 4-2: Schematic showing ID and position of 10×10 mm^2 samples diced from half of the wafer with SnO$_x$ thin film deposited on SiO$_2$/Si substrate (green) and without SnO$_x$ (grey).

4.3 Results and discussion

4.3.1 Phase and microstructure characteristics

An AFM image of the as-deposited SnOx sample #14 (close to the center of the wafer, referring to Figure 4-2) is shown in Figure 4-3. The surface of the film has a comparatively low RMS roughness of 2.7 nm. The morphologies of other samples (#1, 5,18, 24) are similar with roughness less than 3.5 nm.
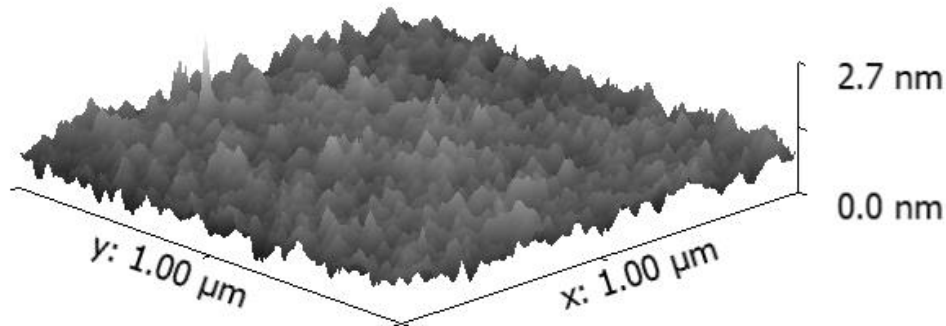
Figure 4-3: Atomic force micrographs showing the surface morphology of as-deposited SnOx sample #14.

Figure 4-4(a) shows representative X-ray diffractograms from the HiPIMS deposited SnO_x film. These were taken from samples 14, 15 and 18 which were located centrally within the wafer during deposition. While peaks belonging to SnO and SnO_2 are observed in sample #14 which was located closer to the Sn source during deposition, only the SnO_2 (111) peak is detected in the remaining (less Sn-rich) samples. All observed peaks are broad, indicating that the as-deposited films were nanocrystalline, typical of tin oxide deposited at or near room temperature [219, 240]. Taking the full width at half maximum (FWHM) (0.30° - 0.28°) of the SnO_2 (111) peaks in each diffractogram and using Scherrer's analysis [241], the average crystallite size was estimated to be 25 - 30 nm.

Elsewhere on the wafer, Sn-rich samples consistently exhibited a mixed phase composition of SnO and SnO_2 with small and broad peaks corresponding to SnO (101), SnO (200) and SnO_2 (111). Oxygen rich samples (located furthest from the Sn source during deposition) exhibited weak or non-existent peaks attributable to SnO or SnO_2, suggesting greater structural disorder in the more oxygen rich (tin-poor) samples.

Figure 4-4(b) shows X-ray diffractograms of HiPIMS deposited SnO_x samples which were annealed in vacuum for 30 minutes at various temperatures. SnO (200) and SnO (101) peaks are observed from the post-annealed sample #14 and #25, respectively while the other peaks (SnO (101) and SnO_2 (111) of sample #14 and SnO_2 (111) of sample #15) are sharper in comparison with those from the as-deposited films (Figure 4-4(a)). Therefore, annealing between 200 °C and 350 °C improved the crystallinity of

these films. Higher annealing temperature caused the disproportionation reaction (phase decomposition) of SnO into Sn and SnO_2, in agreement with previous reports [14, 242, 243]. This explains the absence of SnO peaks produced by samples after annealing at 400 °C and the appearance of new peaks corresponding to SnO_2 (110) in diffractograms taken from the Sn-rich samples (#3 and #4, Figure 4-4(b)).
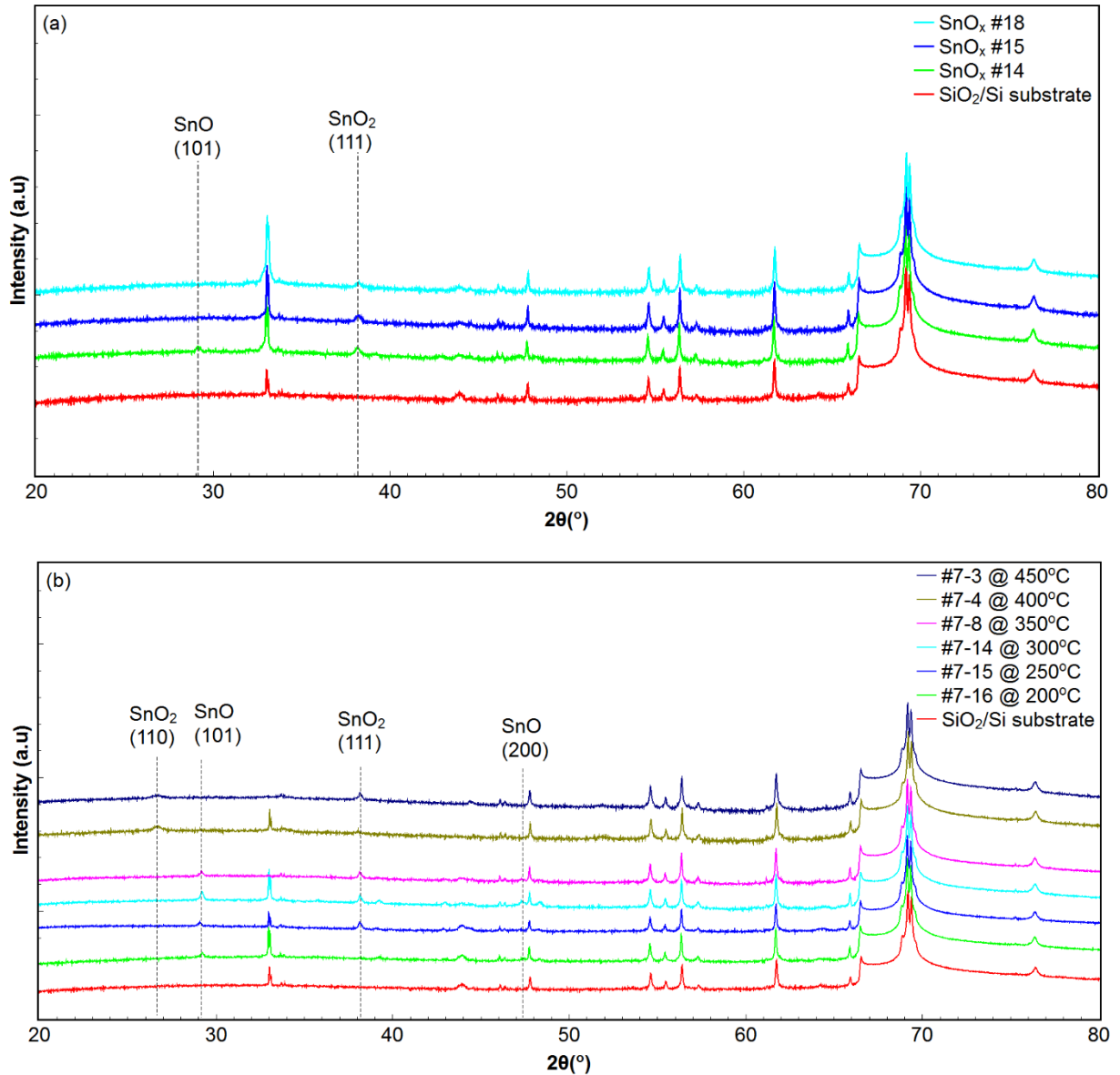
Figure 4-4: XRD diffractograms of (a) SnOₓ films grown on SiO₂/Si substrates by HiPIMS at room temperature and (b) similar HiPIMS SnOₓ films annealed at various temperatures in vacuum after deposition.

4.3.2 Compositional analysis

Figure 4-5(a) shows a valence-band (VB) XPS spectrum (with binding energy range 0 - 15 eV) taken from the HiPIMS SnOₓ #14 film. This spectrum includes contributions from SnO and from SnO_2. The

peak centered at a binding energy of 2.18 eV is attributed to the Sn *5s*-derived valence band maximum (VBM) in SnO while the leading peak at the binding energy of 4.77 eV is a signature of the O *2p*-derived VBM in SnO$_2$. This confirms the existence of both SnO and SnO$_2$ in the film, in agreement with the XRD results. The bandgap of the HiPIMS SnO$_x$ exceeded the ~2.8 eV energy difference between the VB edge and the Fermi energy (at 0.0 eV), which is determined by extrapolating the valence band edge to the instrument background.

Figure 4-5(b) shows the Sn $3d_{5/2}$ spectrum of the SnO$_x$ #14 film, in which the Sn^{4+} and Sn^{2+} components are deconvoluted using the same peak fitting parameters described by Themlin et al. [244]. The peak intensity of Sn^{4+} significantly exceeds that of Sn^{2+}, implying the dominance of the SnO$_2$ phase in the film. From the ratio between these peaks, the composition was estimated to be 1:0.19 SnO$_2$:SnO.
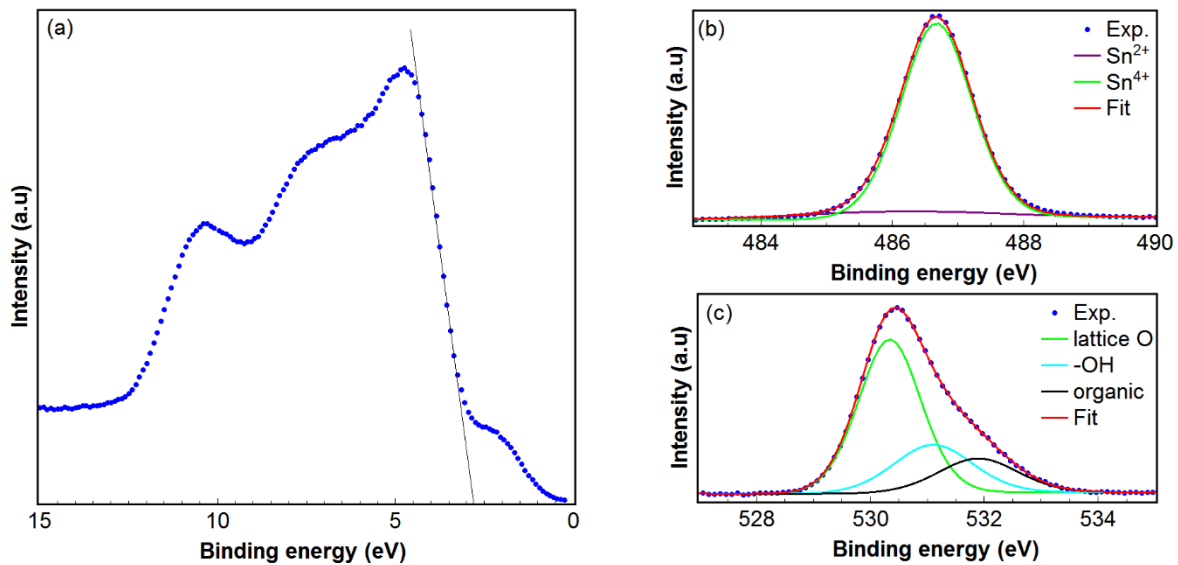
Figure 4-5: (a) XPS spectrum in the valence band region, (b) Sn $3d_{5/2}$, and (c) O 1s spectra of the SnO$_x$ film.

Figure 4-5(c) shows the O *1s* spectrum of the SnO$_x$ #14 film which is composed of lattice O, -OH and -CO groups. The peak of the lattice O component is ~530.4 eV, corresponding to the bond O-Sn^{4+} [245]. This again confirms the main contribution of SnO$_2$ in the film. Surface bound -OH and -CO groups are typically found after the optical lithography process and due to the presence of water vapor in the ambient laboratory environment. The peak at 531.5 eV, corresponding to a -OH group has previously been reported to arise from oxygen vacancies [164]. However, the intensity of the peak at 531.5 eV reduced after in situ Ar etching (Figure 4-6(a)). Since Ar ion etching is known to introduce oxygen vacancies and remove OH groups on a variety of metal oxide surfaces [229, 246], it is believed that the peak at 531.5 eV was caused by attached OH groups. Figure 4-6(a) shows that after in-situ (within XPS system) Ar etching, the ratio between the -OH group and the lattice – bound O is reduced from ~0.37 (before the first etch) to ~0.27 after the first etch and then to 0.13 after the second etch. OH attachment

is known to cause electron accumulation (leading to a metallic-like surface) and downward band-bending in semiconducting oxides including ZnO and SnO_2 [229, 247]. Figure 4-6(b) shows the energy shift of the VBM towards the Fermi energy after the two aforementioned in situ Ar etch processes. The bandgap of SnO is 2.6 – 2.78 eV (Table 2-4) while the bandgap of SnO_2 is 3.6 eV [85]. The gap between the VBM and the FE (0.0 eV on the binding energy scale), denoted by VBM-FE, is larger than the gap between the CBM and the FE (equal to the difference between the bandgap and VBM-FE). This is consistent with the film exhibiting n-type conductivity.
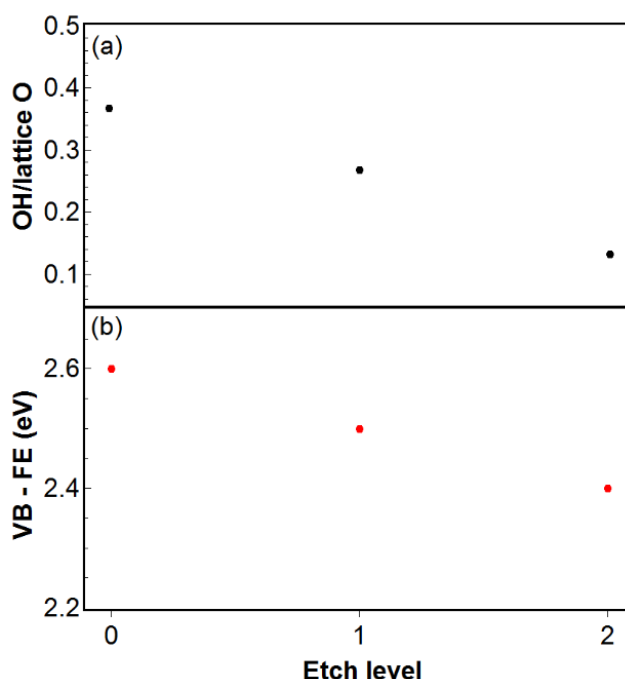
Figure 4-6: (a) The ratio between -OH group and the lattice bounded O and (b) the energy difference VBM-FE after in situ Ar etching processes.

In order to investigate the composition of SnO_x films located at different regions of the wafer, XPS analyses were carried out for three samples #1 (or Sn-rich), #10 (or Sn-mid) and #24 (or Sn-poor). In Figure 4-7(a), the valence band spectra of Sn-rich and Sn-mid samples are similar with the contribution from Sn *5s*-derived VBM in SnO and O *2p*-derived VBM in SnO_2, implying the existence of both SnO and SnO_2 phases in the films and there is no much difference in composition between the Sn-rich and Sn-mid samples. The same conclusion can be drawn from the Sn *3d$_{5/2}$*, and O *1s* spectra of these samples. However, in the Sn-poor sample, there is a significant intensity reduction of the peak attributed to the Sn 5s-derived VBM in SnO (Figure 4-7(a)). Additionally, energy shifts towards Sn^{4+} and O-Sn^{4+} were observed in the Sn *3d$_{5/2}$*, and O *1s* spectra of the Sn-poor sample, in comparison with the Sn *3d$_{5/2}$*, and O *1s* spectra of the other samples (Figure 4-7(b) and (c)). This indicates the increase of SnO_2 contribution in the Sn-poor film and is consistent with the position of the film on the wafer which is far away from the Sn target during deposition. By analysing VB, Sn *3d$_{5/2}$*, and O *1s* spectra of some SnO_x

51

films, the tin to oxygen ratio (Sn:O) ranged from 1:1.7 to 1:1.9 from the Sn-rich to Sn-poor sides of the wafer.
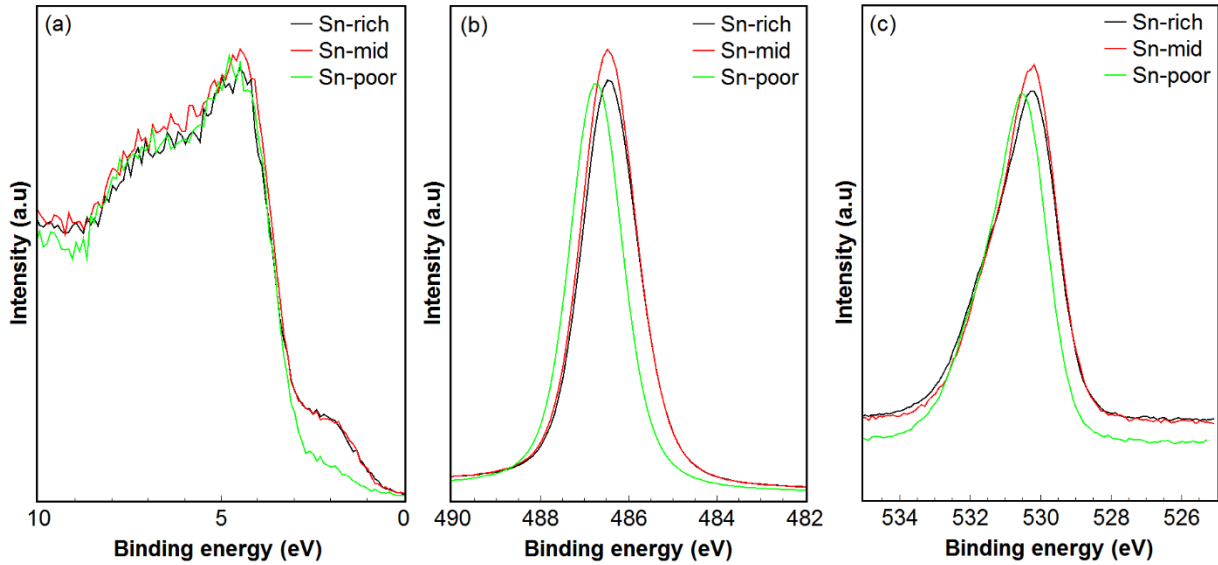
Figure 4-7: (a) XPS spectra in the valence band region, (b) Sn 3d5/2, and (c) O 1s spectra of the SnOx films located at different regions (Sn rich, Sn poor and the middle of the wafer).

4.3.3   Optical and electrical properties

As the SnO_x film was deposited on a SiO_2/Si wafer, the optical properties of the film/samples were determined using an Oscillator model and Tauc's graphical method [248] for optical gap extraction based on the ellipsometry data. The ellipsometric angle ψ and phase difference Δ were recorded in the wave length range from 200 nm to 1000 nm when the incidence angle was varied from 65, 70 and 75°. The refractive index n and extinction coefficient k were extracted by fitting the spectroscopic spectra of ψ and Δ as a function of the incident wavelength λ. Figure 4-8(a) and (b) shows the extracted refractive index n and extinction coefficient k over the 300-800 nm wavelength range. The refractive index decreased with wavelength as observed in other tin oxide films [249]. All samples (Sn-rich and Sn-poor) exhibited similar values of the refractive index n and extinction coefficient k within the wavelength range 300 nm to 800 nm. The optical bandgap of the as-deposited SnO_x samples were estimated by both the direct and indirect bandgap approximation of the Tauc plot, $(\alpha h v)^2$ and $(\alpha h v)^{1/2}$ versus E respectively. However, the values obtained from the direct band gap approximation were much higher for both tin oxide samples than those reported in previous studies [7, 245], hence, the indirect band gap nature of HiPIMS SnO_x is inferred. By extrapolating the linear portion of the plots to the energy axis, the bandgaps of Sn-rich and Sn-poor samples were estimated to be ~3.5 eV and ~3.6 eV, respectively (Figure 4-8(c)). The difference in the bandgaps of these two samples can be explained by the higher ratio of SnO_2, which has a higher bandgap than SnO phase, in the Sn-poor film.

52
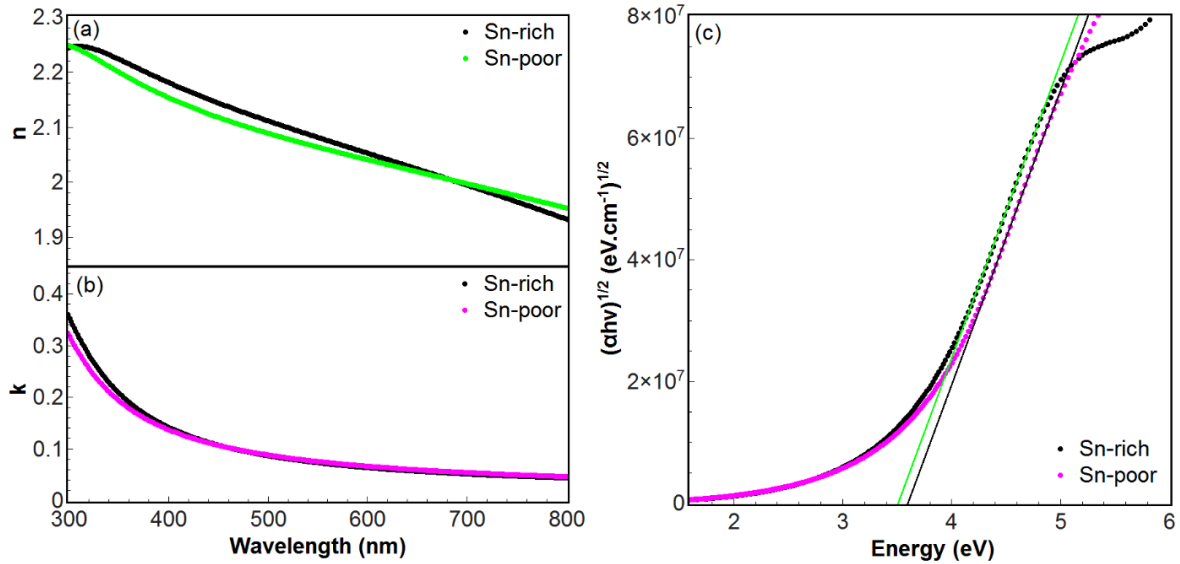
Figure 4-8: (a) Refraction index n and (b) extinction coefficient k as a function of incident wavelength λ for Sn-rich and Sn-poor samples. (c) Tauc plots obtained from Sn-rich and Sn-poor samples.

The as-deposited HiPIMS SnO_x films exhibited high resistivity (0.1 - 10 GΩ). Consequently, the carrier concentration and mobility of the films could not be reliably measured using the Hall measurement system available to this project. After post-deposition annealing in vacuum, the resistivity of the films decreased. Hot-probe measurements confirmed that after annealing, samples with low annealing temperature (less than 400 °C) did exhibit p-type conductivity. However, low carrier concentration and/or low carrier mobility once again lead to Hall-effect measurements that were inconsistent at differing measurement currents. Based on the measurements, it is probable that the p-type carrier mobility was significantly less than 1 cm^2/V.s. This hindered application of the HiPIMS SnO_x films in TFTs but the as-deposited semi-insulating character of the films enabled memristive characteristics to be investigated with these films serving as the active insulating layer in prototype memristor devices.

4.4 Summary

Tin oxide deposited on a SiO_2/Si wafer at room temperature using a HiPIMS deposition system, was characterized structurally, optically and electrically. A mixed phase composition of SnO and SnO_2 existed in the as-deposited thin film with SnO_2 being the dominant phase. The elemental compositions of the 10×10 mm^2 samples cleaved from the wafer were determined by XPS to be in the range from 1(Sn):1.7(O) (Sn-rich side) to 1(Sn):1.9(O) (Sn-poor side). The composition varied systematically with the original position of the sample on the wafer and with respect to the Sn sputter source. The high resistivity measured in the as-deposited SnO_x samples, low carrier concentration and low mobility of the as-deposited and annealed samples prevented the application of the HiPIMS tin oxide in thin film transistors. However, these properties suggested suitability for the thin film tin oxide as a memristive device material. This aspect of the material is explored in detail in chapters 5 and 6.

Chapter 5:

Resistive switching in tin oxide thin film memristors

In this chapter, the memristance in mixed-phase tin oxide thin films prepared by high power impulse magnetron sputtering (HiPIMS) is described. This involves the investigation of switching mechanism and device behaviour under different conditions. The aim of this work is to determine the memristive characteristics of tin oxide thin film memristive devices and investigate their applications.

5.1   Introduction

Owing to scalability, low power consumption, fast switching and biological synapse mimicking capabilities, memristors have been considered as potential candidatures for next generation non-volatile random-access memories and neuromorphic systems [142, 250]. The ability to store memory as a resistance state in an ultra-compact device is a notable characteristic [139] but emulation of biological synaptic behaviour is perhaps more significant in enabling new circuit technology [191]. A continuum of possible device resistances and plasticity (activity dependent resistance) enable brain-inspired computing [251] that can complete tasks such as pattern recognition with much greater efficiency than achievable technology with conventional Von Neumann computing. Hybrid approaches that combine Von Neumann and bio-inspired architectures are also possible [251-253].

As a memristive material, tin oxide has received less attention than other oxides, but non-volatile memristors that include tin oxide active layers have been demonstrated [183, 185-187]. Nagashima et al. [183] reported unipolar Pt-contacted non-volatile memristors with pulsed laser deposited tin oxide layers that were compatible with CMOS fabrication. When operated as a resistive random-access memory cell, the authors observed retention times up to 10^4 s and endurance up to 100 cycles. Since then, non-volatile operation with state retention times up to 10^5 s and endurance exceeding 500 cycles have been observed in memristors with SnO_x active layers [185-187]. Resistive switching in tin oxide has consistently been attributed to electric field induced migration of defects (principally oxygen vacancies and/or interstitial tin) [164, 183, 185-187]. Very recently, Pan et al. [164] demonstrated solution processed SnO_2 memristors with volatile resistive memory. Synaptic characteristics including short term potentiation and spike rate dependent plasticity were observed in their (asymmetric) Au-SnO_2-FTO devices. The mechanism was once again attributed to migration of charged defects (oxygen vacancies) through the layer and into Schottky barrier depletion regions at the interfaces.

This chapter presents the electrical properties of lateral memristors configured with symmetric inert platinum contacts and mixed phase tin oxide thin films deposited at room temperature using high power impulse magnetron sputtering (HiPPIMS). The morphological changes and conduction mechanisms in these devices were investigate. Activity dependence and input voltage pulse sequence were also used to highlight potential employment of SnO_x memristors in bio-inspired pattern recognition systems.

5.2   Experiment

A thin film of tin oxide was deposited at room temperature onto SiO_2 (50 nm layer thickness on Si wafer) using a high-power impulse magnetron sputtering (HiPIMS) system, with the details described in Section 4.2. The memristors were formed by coating platinum contacts on the top of the fabricated tin oxide films using a two-step lithographical/lift-off process. In the lithographical step, electron-beam resist (950 PMMA A4, 200 nm thickness) was patterned using a FEI Nova NanoSEM interfaced with Nabity NPGS electron beam writing software. The operating conditions were: 30.00 kV accelerating voltage, 5.0 mm working distance, and 24 pA beam current. A Gatan PECS ion-beam deposition system was then used to deposit the 20 nm thick Pt layer. After a lift-off step, remained two contacts each 2 μm in width and separated by 300 nm approximately (Figure 5-1).
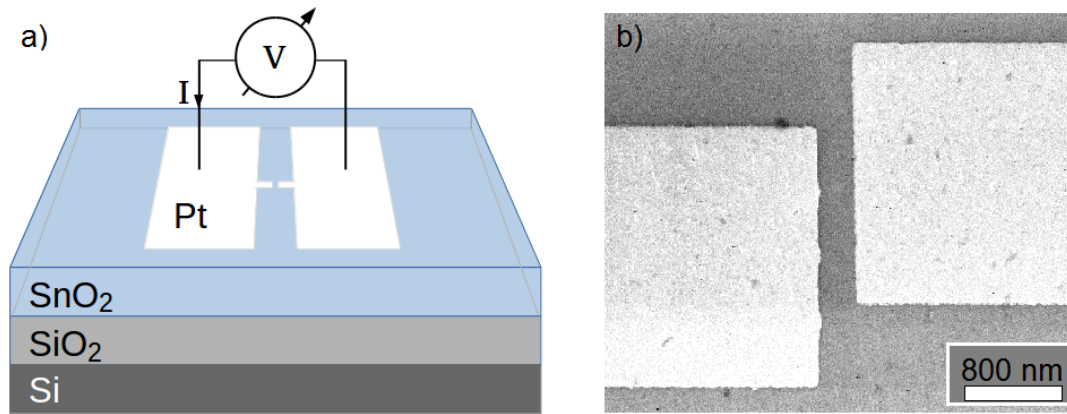
Figure 5-1: (a) Schematic and (b) scanning electron microscopy (SEM) image of the Pt contacted SnO_2 memristor

X-ray diffraction (XRD), X-ray photoelectron spectroscopy (XPS), spectroscopic ellipsometry and atomic force microscopy (AFM) were used to investigate the crystal structure, composition and morphological changes of the tin oxide films of the memristive devices in the pristine, post-annealing stage or after switching activities.

5.3   Result and Discussion

5.3.1   Resistive switching in memristive thin film tin oxide devices

Figure 5-2 shows room-temperature current-voltage (*I-V*) characteristics taken using Keysight twin channel source-measurement unit. With no electroforming step required, the device exhibited stable volatile bidirectional resistive switching with more than two orders of magnitude separating the high and low resistance states. A 100 nA current limit was imposed during measurement to avoid damage to the device. The *I-V* sweep period lasted about 24 s with 1001 measuring and recording times. Below the threshold for both positive and negative voltage, the memristive device is in the high resistance state (HRS), marked as steps "1" and "3" in Figure 5-2(a). With an applied voltage of 17 V (or electric field of 0.5 MV/cm) approximately, the current (and conductance) increases significantly until reaching the compliance current (100nA), demonstrating the switching to low resistance state (LRS). Due to the high conductance state of the device, the current still maintains at 100 nA even after the applied voltage reduces below the threshold voltage (17 V), and then decreases, as marked by steps "2" and "4" in Figure 5-2(a). As the bias reduces, the current becomes insufficient to sustain the conductive path between two the Pt electrodes and the device switches back to the HRS.

Figure 5-2(b) shows the switching characteristics of the memristive SnO_x device over 50 consecutive *I-V* sweeps with the average OFF/ON switching ratio for the device at 20 V over 50 cycles found to be around 128. The positive and negative threshold voltages varied by less than ±1 V over 50 sweep cycles. The current–voltage plots in Figure 5-2(b) are approximately symmetric as expected from a symmetric device.

In Figure 5-2(c), the cumulative probability of switching during 50 similar *I-V* sweeps is plotted as a function of the threshold voltage and fitted using Weibull analysis [254].

$$F(x) = 1 - exp\left[\left(-\frac{x}{x_0}\right)^{\beta}\right]$$

(5-1)

Where *F(x)* is the switching probability, *x* is a voltage, x_0 is the average value of threshold voltage, and *β* is the Weibull slope. A single Weibull slope parameter provides reasonable agreement to the experimental data (Figure 5-2(c)) and this is indicative of a single filamentary conduction path [254].

Atomic force microscopy was performed on devices before and after switching. Provided the 100 nA compliance limit was imposed, no morphological transformations were observed. However, after the device was operated with a higher current compliance (300 nA), a feature resembling a filamentary path between the electrodes was observed (Figure 5-2(d)), supporting the assertion that a filament produced the switching behaviour shown in Figure 5-2(a) and (b).

The dominant transport mechanisms in the HRS and LRS differ as shown in Figure 5-3(a) and (b). In the HRS (Figure 5-3(a)), transport is limited by Schottky emission, consistent with the presence of Schottky barriers at the device interfaces. The differential resistance (*dV/dI*) measured at zero bias in the HRS was 12 GΩ. Van der Pauw resistivity measurements on the tin oxide layer were obtained using Al ohmic contacts and these provided an estimated resistance of the layer between the device contacts of 0.5 MΩ. Hence, the interfacial potential barriers are significant in limiting the device current in its HRS.
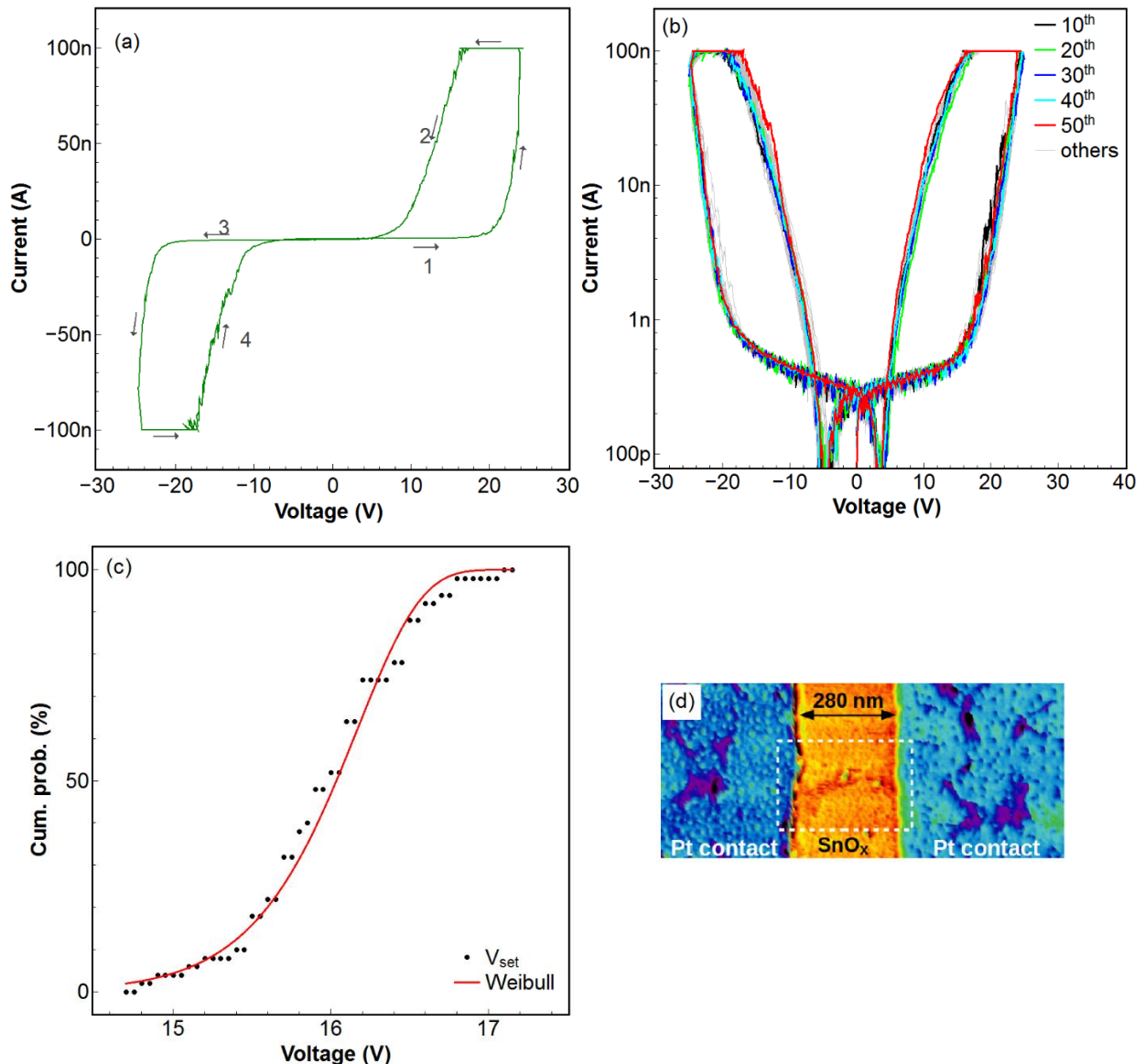
Figure 5-2: (a) Typical I-V characteristics of the lateral memristor with 100 nA current limit imposed during measurement. (b) Bidirectional resistive switching of a memristive device over 50 consecutive I-V sweeps with highlighted 10th, 20th, 30th, 40th and 50th sweeps (black, green, blue, cyan and red lines, respectively) in log (current) scale. (c) Cumulative probability of set threshold voltages fitted with the Weibull function. (d) An atomic force micrograph showing a filamentary conduction path in a device operated at higher current (300 nA).

When the current drops below the current compliance of 100 nA in the LRS (Figure 5-3(b)), the *I-V* relationship is approximately linear. This is consistent with the characteristics of back-to-back Schottky diodes in which the Schottky barriers do not limit the current and the dominant carrier transport mechanism is direct tunnelling through the potential barriers [255]. The data in this region can be also fitted with the Fowler-Nordheim (F – N) equation (eq. 5-2) [256-258].

$$I = A_{FN}V^2 \, exp\left(-\frac{4d\sqrt{2m_e\Phi^3}}{3\hbar qV}\right)$$

$$(5\text{-}2)$$

Where I is the current passing through the device, A_{FN} is the F – N constant, V is the applied voltage, d is the barrier width, m_e is the effective electron mass in the insulator, $\hbar$ is the reduced Planck constant, Φ is the barrier height and q is the electron charge. However, F – N emission was excluded as the transport mechanism as a barrier width of 20 nm was required for best correspondence to our data and this is too thick for tunnelling [259].
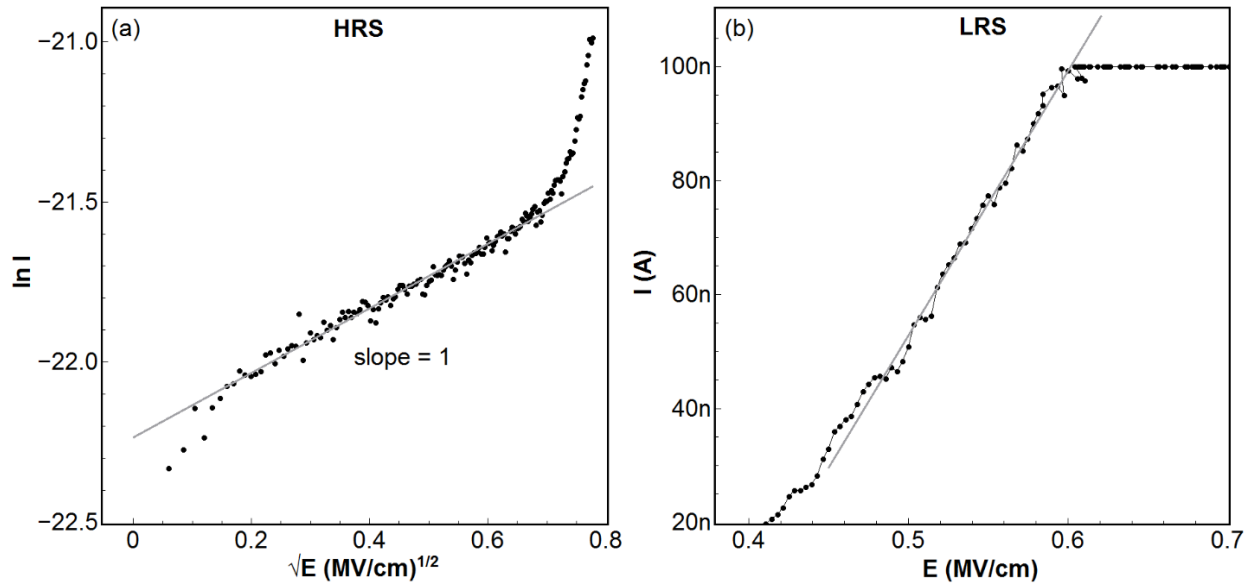
Figure 5-3: Data and fitting in (a) HRS and (b) LRS of a memristive SnOₓ device in a typical sweep

5.3.2   Switching mechanism of memristive tin oxide devices

Current-controlled V-I characteristics are shown in Figure 5-4(a). Clear s-type negative differential resistance (NDR) is observed at room temperature (298 K) but this characteristic reduces as the temperature is increased and disappears at ~360 K. Similar behaviour has been observed previously in metal oxides including VO₂ [260], HfO₂ [261], Ti₄O₇ [262] and NbO₂ [263]. It has been suggested that the increased conductivity could be a result of a temperature-induced Mott insulator-to-metal transition (IMT) [263], however, the behaviour has also been attributed to combined Joule-heating and Poole-

Frenkel conduction [264]. CC-NDR in oxides is of considerable interest for applications such as selector element in crossbar memory arrays, inductor-less voltage-controlled oscillators or relaxation oscillators [263, 265, 266]. This suggests that the HiPIMS deposited SnO_x film may be suitable for selector devices. By studying the dependence of NDR on temperature (Figure 5-4(a)), the maximum working temperature of tin oxide – based devices (as selectors) is obtained.

The threshold voltage and power of the SnO_x device are displayed in Figure 5-4(b) and (c), respectively. Both are observed to decrease in magnitude as the device temperature is increased. At ~330K, the approximate operating temperature of many microelectronic devices, NDR is still observed with the threshold voltage less than 8V and the threshold power less than 30 nW.
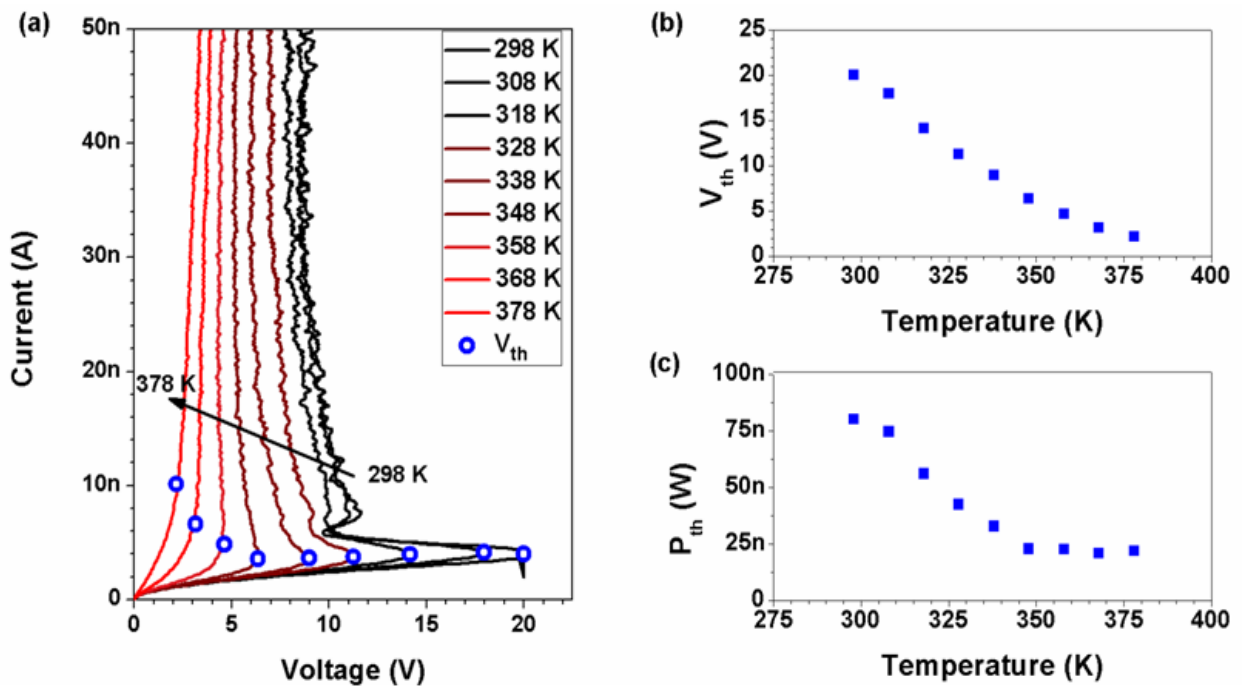
Figure 5-4: (a) Temperature dependent V-I characteristics of the lateral tin oxide memristor with 20 V voltage limit imposed during measurement, (b) Threshold voltage, V_{th}, and (c) threshold power, P_{th}, as a function of device temperature.

Based on the data/microscopy analysis presented above, a filament formation mechanism for memristance is proposed for the SnO_x memristive device. In the LRS, this filament straddles the Schottky barriers within the device and produces the Ohmic characteristic shown in Figure 5-3(b). Regarding the composition of the filament, we can exclude diffusion/migration of the contact material (often occurring in memristors) and subsequent filament formation as a switching mechanism because Pt is inert and non-migratory [137, 267] (even at significantly higher electric fields than employed here). Device encapsulation (in 200 nm - thick polymethylmethacrylate) caused no significant change in the device characteristics; bidirectional, volatile threshold switching with similar relaxation characteristics

were still observed. This showed that the filamentary memristive conduction occurred within the tin oxide layer rather than across a surface contamination layer.

It has been reported that Joule heating causes local temperatures exceeding 1000 K within many memristive devices and consequently plays a pivotal role in their operation [268]. In order to elucidate the role of Joule heating, a separate sample of the SnO_x device layer was annealed in air at 400 °C for 30-mins. After cooling, XRD, XPS and spectroscopic ellipsometry were repeated to investigate any change in crystal structure and element composition.

Figure 5-5 shows XRD diffractograms of the tin oxide film formed on the SiO_2/Si substrate as deposited and after annealing at 400°C in air for 30 minutes. The SnO_2 (101) peak coincidentally has the same position (33.33°) with the Si (211) peak. The SnO_2 (101) phase was thought to exist in the as-deposited and annealed memristive HiPIMS SnO_x device layer as the higher intensities of the peak located at 33.33° in the X-ray diffractograms of both the as-deposited and annealed SnO_x layer were observed compared to that in XRD of the SiO_2/Si substrate.

The broad peaks corresponding to SnO (101) (at 29.8°), SnO (200) (at 47.85°), SnO_2 (101) (at 34°) and SnO_2 (111) (at 38°) can be seen in the XRD diffractograms of the as – deposited SnO_x, implying the existence of both SnO and SnO_2 phases and the nanocrystalline structure of the tin oxide layer of the memristive device. Using Scherrer's analysis, the average crystallite size was estimated to be around 30 nm from the 0.30° - 0.27° full width at half maximum (FWHM) of the SnO (101) and SnO_2 (111) peaks. After the sample was annealed in air, only the SnO (101) peak was visible in the diffractogram. The disappearance of peaks from SnO_2 does not imply removal of SnO_2 post – annealing. Decomposition $(2SnO \rightarrow SnO_2 + Sn)$ has been reported to occur in SnO at 300°C [242]. The comparison between XRD diffractogram patterns of the as – deposited and post – annealed sample does infer that annealing at 400 °C in air induces moderate crystallization of SnO in the favoured (101) orientation whilst causing disordering of the SnO_2 phase.
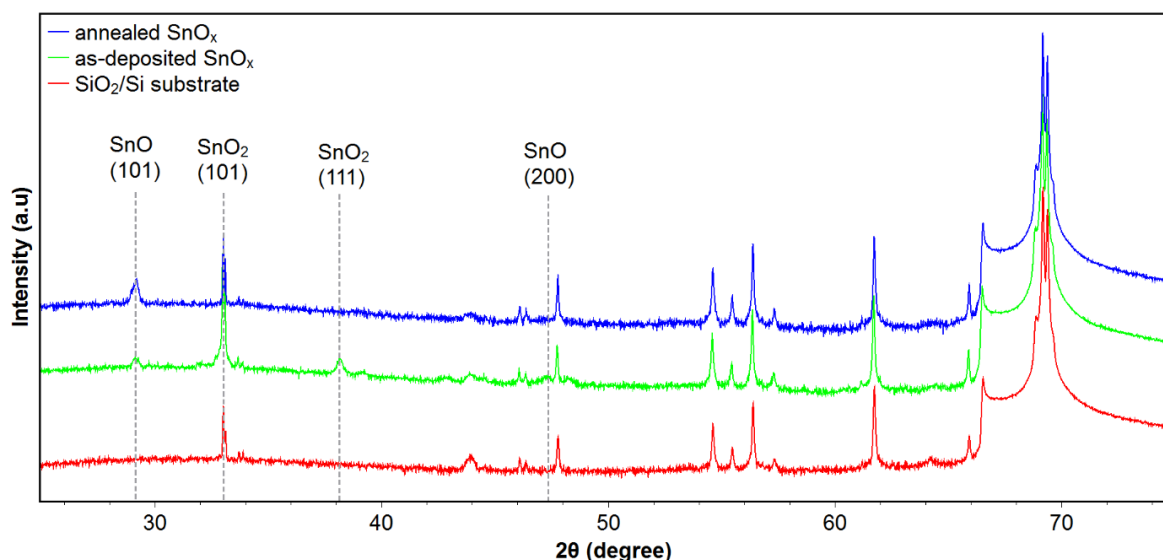
Figure 5-5: X-Ray diffractograms collected from an as-deposited and annealed memristive SnOₓ device layer on SiO₂/Si substrate.

Figure 5-6 illustrates the deconvolution of the core level spectra for Sn *3d$_{5/2}$* and O *1s,* and the spectrum in the valence band (VB) region (in the binding – energy range of ~0 to 15eV) collected from the memristive tin oxide device layer before and after annealing in air. The XPS system was calibrated so that zero on the binding energy scale corresponded with the Fermi energy. The element (Sn and O) binding energies were aligned to adventitious carbon (C *1s*) binding energy of 284.8 eV.

The Sn*3d$_{5/2}$* spectrum was deconvoluted with Sn^0, Sn^{2+} and Sn^{4+} components. Since the contribution of Sn^0 is negligible, this component is excluded in the deconvolution. Quantifying the phase composition of sub-stoichiometric tin oxide from Sn *3d$_{5/2}$* XPS can be problematic as the electron binding energies of Sn^{2+} and Sn^{4+} differ by only 0.7 eV [133, 244]. Using the same peak fitting parameters described by Themlin et al.[244], the best – fit curves for both Sn*3d$_{5/2}$* spectra of the as – deposited and post – annealed films are illustrated in the Figure 5-6. The results show that the Sn *3d$_{5/2}$* spectra are mainly composed of Sn^{4+}, indicating the dominance of Sn^{4+} or SnO_2 in the films either as-deposited or after annealing. The phase compositions of the as-deposited and post-annealed films were estimated to by 1:0.21 and 1:0.08 SnO_2:SnO respectively. The Sn:O ratios extracted from the Sn *3d$_{5/2}$* and O *1s* peaks were 1:1.83 and 1:1.92 in the memristive SnOₓ device layer before and after post-annealing process, respectively. The reduction of Sn^{2+} portion in the Sn *3d$_{5/2}$* XPS spectrum of the annealed film compared to that in the Sn *3d$_{5/2}$* spectrum of the as-deposited film and the increase of oxygen content confirm the transformation of the SnO phase into the stable SnO_2 phase in the high temperature and oxygen rich environment.

The O *1s* spectra (Figure 5-6) include contributions from lattice bound oxygen and from surface bound CO and OH. The peak at 531.5 eV has previously been reported to be attributed to oxygen vacancies [164]. However, that peak was proved to arise a from hydroxyl group (detail in section 4.3.2).

Furthermore, the reduced intensity of the peak at 531.5 eV after 400°C annealing (compared with the case of as-deposited in Figure 5-6) is in agreement with the reduction of the hydroxyl group after annealing at high temperature. Hence, the O *1s* XPS data is not suggestive of a change in the density of oxygen vacancies (which influence the n-type conductivity of the tin oxide film).

In the valence-band spectrum collected from the as-deposited SnO_x film shown in Figure 5-6(a), the leading peak centred at an energy of 4.78 eV is attributed to the O *2p*-derived valence band maximum (VBM) of SnO_2 [14, 244]. Importantly, the small peak at 2.58 eV which is a distinct signature of Sn *5s*-derived VBM in SnO [14, 244] is also clearly visible. The relative intensities of these peaks provide an alternative method for estimating the phase composition, also proposed by Themlin et al. [244]. A value of 0.2 for the intensity ratio *I(Sn 5s)/I(O 2p)* yields an area ratio $S(Sn^{2+})/S(Sn^{2+} + Sn^{4+})$ of 0.17, in close agreement with the value obtained from fitting the Sn *3d$_{5/2}$* peak (1:0.21 SnO_2:SnO). A significant decrease in the Sn *5s*-derived peak of SnO (Sn(II)) following annealing was observed in the valence band spectrum (Figure 5-6(b)). This peak comprises acceptor-like states above the VBM of Sn(IV) and these compensate the inherent n-type conductivity of the dominant phase. Increased n-type conductivity (attributed to interstitial Sn and/or oxygen vacancies [269]) is therefore expected to accompany a decrease in the intensity of this peak. Electrical measurements confirmed this and showed a two-orders-of-magnitude increase in conductivity post-annealing.
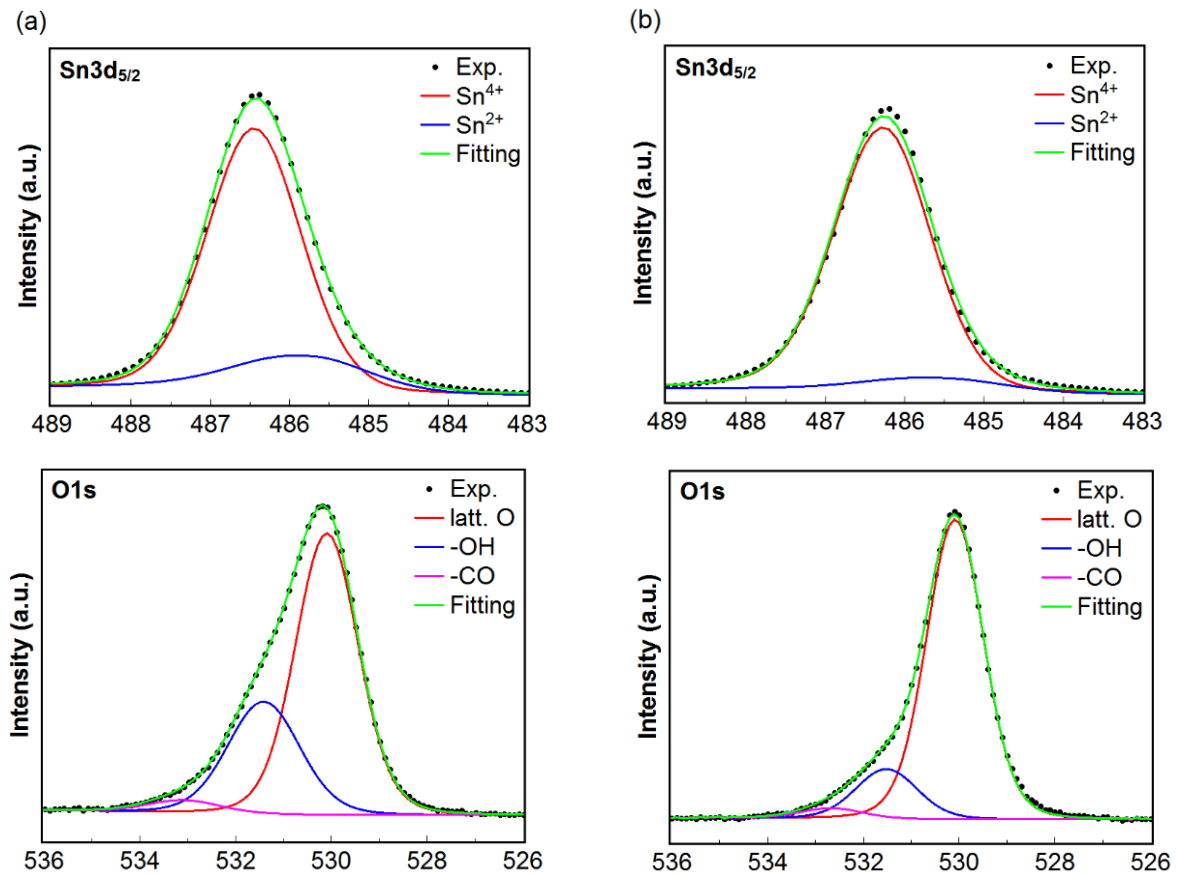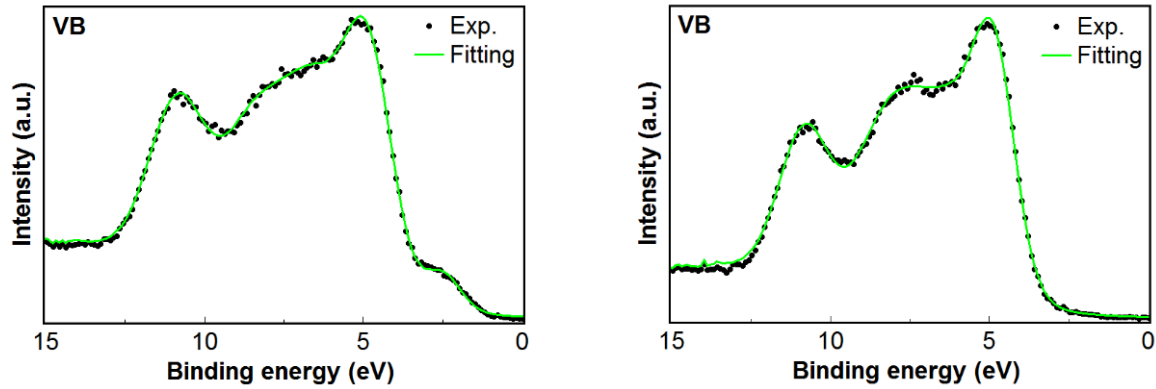
Figure 5-6: Sn 3d$_{5/2}$, O 1s and valence band (VB) x-ray photoelectron spectra collected from the (a) as-deposited and (b) annealed SnO$_x$ layer.

Tauc's graphical method [248, 270] was used to determine whether the SnO$_x$ samples have a direct or indirect band gap and whether there is any change in the optical band gap between as-deposited and annealed samples. Both the direct and indirect bandgap approximation of the Tauc plot, $(\alpha h v)^2$ and $(\alpha h v)^{1/2}$ versus E respectively were employed to estimate the optical bandgap of the as-deposited and annealed SnO$_x$ samples. However, the indirect band gap of HiPIMS SnO$_x$ is inferred when the direct band gap approximation yields much higher values for both tin oxide samples before and after annealing than those reported in previous studies [7, 245]. In Figure 5-7, the intercepts over the energy axis of the extrapolated linear portion of the plots indicate approximate band gaps of 3.5 and 3.92 eV for the sample before and after annealing respectively. The increase of the band gap after annealing is attributed to Burstein–Moss shifts [271]. This effect often occurs in oxide materials owing to the highly dispersed states that form the bottom of the conduction bands [269, 272]. Hence, electrons occupy states within the conduction band, causing the Fermi level to shift to higher energy and widening the apparent band gap. The increased n-type conductivity measured after annealing is consistent with this interpretation of the optical measurements.
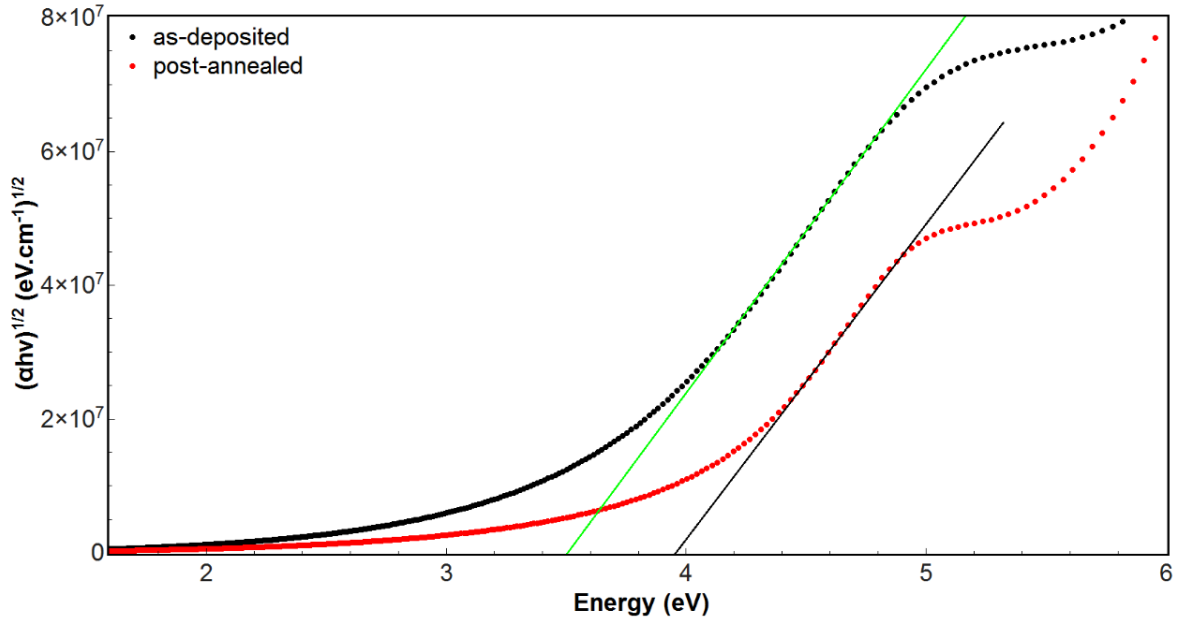
Figure 5-7: Tauc plots taken from the as-deposited and annealed SnOx samples.

Returning to the memristive devices, their LRS is thought to result from Joule heating induced decomposition of the along a preferred current path between the contacts. A highly n-doped SnO_2 filament is then produced as SnO decomposes to SnO_2 and Sn. As the voltage across the device and the current through it are reduced, the filamentary path rapidly cools, and oxygen back-diffuses causing the filament to re-adopt a mixed SnO_2-SnO phase composition and relax to the HRS. The oxygen required for this relaxation may mostly reside within the layer since encapsulation (polymethyl methacrylate PMMA) produced no significant difference in this characteristic. Joule heating induced phase changes have been reported in many other memristive materials (see for example [268]) but we have yet to see it explicitly stated as a mechanism for resistive switching in tin oxide. It was not possible to probe the structure of the nanoscale filament itself but based on prior reports describing phase change memristance in other material systems [251] it is likely that higher crystallinity/order exists in the filament than in the surrounding (unmodified) layer. This would further contribute to the significant difference in resistance between the HRS and LRS of the device. After rapid cooling (quenching) it is also likely that the filamentary region re-adopts its amorphous structure [251].

5.3.3   Light sensitivity of tin oxide thin film devices

Figure 5-8 presents the I-V characteristic of a memristive tin oxide thin film device when exposed to UV illumination (wavelength = 310 nm, FWHM = 15 nm, power density = 100 μW/cm^2). The dark I-V characteristics are included to show the response due to illumination. Taken together, these results show that the response (in LRS and HRS) exhibited by the device upon illumination is due to photo-conductivity in the semi-insulating device layer. The excitation of free carriers by the UV illumination

causes an increase in free carrier concentration, resulting in higher conductivity in the HRS. In the LRS, a filament connects the electrodes. The filament is thought to consist of highly-doped SnO_2 (after thermal decomposition of SnO to SnO_2 and Sn) and UV-illumination again leads to more conduction due to higher carrier concentration. An increase in both conductivity and relaxation time were obtained. The relaxation time was taken to be the time required for the device to return to within 1% of its LRS conductance. The conductance in the LRS at +10 V bias is approximately three times higher when the device is exposed to UV light. As mentioned previously, Schottky barriers at the contacts are the dominant factor in limiting the device current transport in its HRS. In the LRS, these barriers are short-circuited by the filament and they are no longer the dominant factor in limiting current transport. The larger increase in conduction exhibited in the LRS is consistent with this assertion.

The thin film tin oxide memristors exhibited wavelength – dependent conductance (in their HRS and LRS) with no significant response shown in the visible spectrum. This suggests that these devices maybe used for neuromorphic light sensory applications [273].
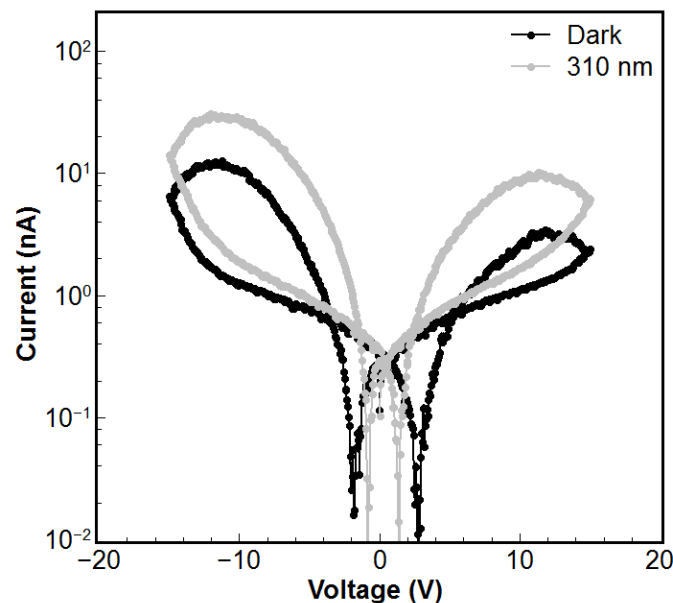
Figure 5-8: I-V characteristics for a SnO_x thin film device in dark and ultraviolet – illuminated (310 nm, 100 μW/cm²) conditions.

5.3.4 Activity – dependent conductance and pulse response of thin film tin oxide devices

Memristive thin film SnO_x devices have demonstrated a volatile bidirectional threshold switching behavior. This short-term memory behavior suggests suitability for bio-inspired signal processing system. In order to demonstrate the temporal dynamics of the memristive SnO_x devices, their responses (represented by the read current) to different applied pulses in different time sequences were recorded. In these pulse measurements, the memristive SnO_x devices exhibited a high dependence on the intensity, separation time and the number of stimulations.

Figure 5-9(a) illustrates the voltage input (upper panel) and current response (lower panel) of a memristive SnO_x device. With single 300 ms wide input voltage pulses, the device did not exhibit any clear response until the pulse amplitude reached 15 V. Further increase of the pulse amplitude to 20 and 25 V led to larger output currents of 100 nA and 300 nA, respectively. This characteristic mimics synaptic behavior in which increases in synaptic weight (conductance) become more significant under higher intensity stimuli (in this case, higher amplitude voltage pulses).

In addition to varying amplitude, varying duration also produces differing device responses. In Figure 5-9(b), 20 V amplitude pulses with differing widths are applied to the device. A long interval time (18 s) was used to enable full relaxation back to the HRS to occur between pulses. Pulse widths of 180 and 230 ms produce similar current responses but longer pulses (280 and 330 ms) produce more significant increases in current and device conductance. This increasing response above a threshold pulse width is attributed to filaments in differing states. Below the threshold pulse width, the filament is believed to be incomplete (fragmented) with tunnel gaps limiting the current-flow. Above the threshold pulse width, the filament is more complete and as the pulse width increases further, the effective diameter of the filament increases as does its conductance.
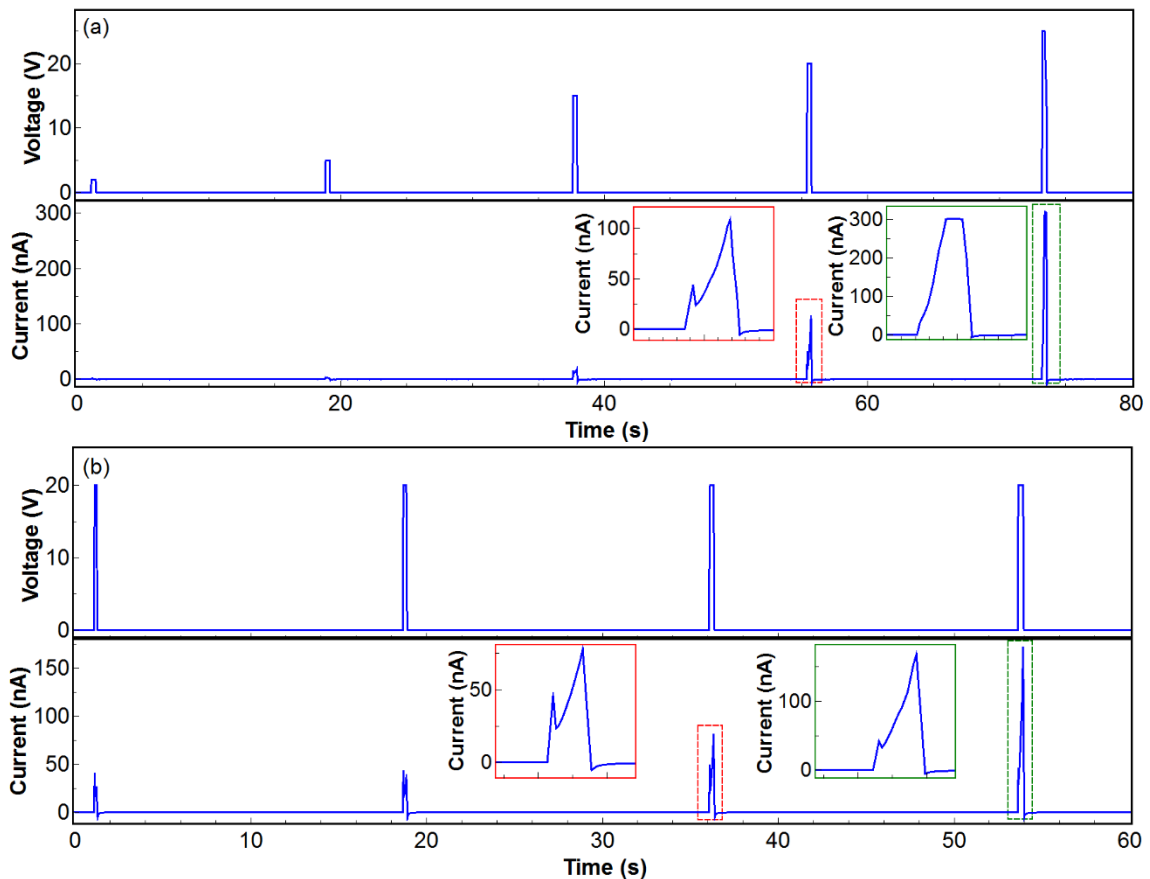
Figure 5-9: Input pulse sequences (upper panels) and responses (lower panels) of the memristive tin oxide device. (a) A sequence of 300 ms wide input voltage pulses of variable pulse amplitude (2, 5, 15, 20, 25 V) and

the corresponding output currents with 300 nA current limit. (b) A sequence of input voltage pulses composed of a variable range of pulse widths from 180 to 330 ms (step of 50 ms) with amplitude of 20 V and corresponding output currents. One electrode was biased while the other was grounded during measurements (see Figure 5-1).

Figure 5-10(a) demonstrates the conductance modulation of the device per pulse (200 ms duration, 1.5 Hz) as a function of input voltage. In Figure 5-10(a), the conductance modulation rate, dG/dt, increases with increasing voltage pulse amplitude. As in threshold switching devices in which metal ion-diffusion occurs [252], an incubation period is observed before a rapid rise in the conductance takes place. However, in the SnO_x filamentary devices, this effect is believed to result from increased device temperature due to cumulative Joule heating. In the absence of external heating, if the inter-pulse interval (time interval between pulses) is sufficiently short, the device can switch to its LRS at lower threshold voltages. For example, with a train of 50 consecutive pulses (amplitude 7.5 V, pulse width 200 ms and frequency 1.5 Hz), the device conductance reaches 20 nS (Figure 5-10(a)). As previously shown in Figure 5-9(b), a single 20 V pulse of 330 ms duration was required for this device to obtain the same conductance.

Figure 5-10(b) shows the implementation of paired-pulse facilitation (PPF) which describes the increase of device conductance under the application of paired pulses which are separated in time below a maximum period. This data was collected after an incubation period of 200 s (and 200 pulses) at which point the conductance after each pulse remained similar, as shown in Figure 5-10(a). By increasing the inter-pulse period (corresponding to a frequency reduced from 1.5 Hz to 1.0 Hz), the conductance decreases with each pulse. With the extended inter-pulse period, the stimulation is not sufficient to prevent the filament relaxing due to back-diffusion of oxygen and reformation of SnO. With this longer inter pulse width (and frequency = 1.0 Hz), the conductance decay rate is higher after the 7.5 V pulses than after the 5.5 V pulses. This is consistent with a higher Joule heating and subsequent cooling when the 7.5 V pulses are applied.

68
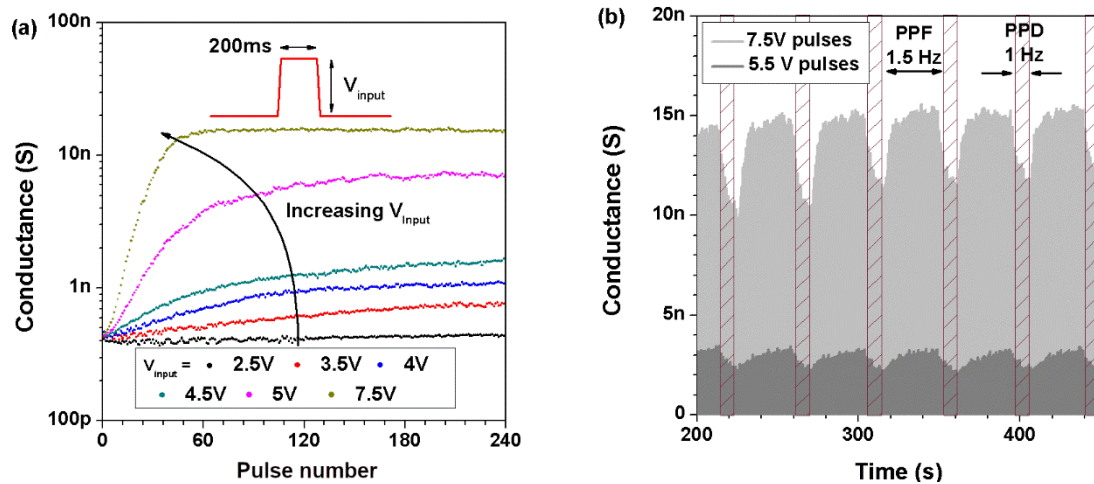
Figure 5-10: (a) Conductance evolution in response to voltage pulse trains of different pulse height, V_{input} (1.5 Hz, 200 ms duration). (100 nA current limit imposed during measurement). (b) paired-pulse facilitation (PPF) implemented by increasing the pulse frequency.

Figure 5-11 shows the evolution of the device current and conductance with repeated application of voltage pulses of different frequency. The device conductance again mimics the short-term potentiation observed in biological synapses in which the application of paired pulses induces an increase in synaptic weight (Figure 5-11(b)). Shorter inter-pulse intervals cause greater increases in conductance than longer inter-pulse intervals (see Figure 5-11(b) inset). Relaxation times ranged from 430 ms to 340 ms for inter-pulse intervals of 110 ms and 1.75 s, respectively. For longer inter-pulse intervals, the relaxation time remained at around 300-340 ms. Long-term potentiation (describing prolonged high conductance after removal of applied voltage) did not occur during any swept or pulsed *I-V* measurements performed on the devices. Nevertheless, the 'bio-realistic' relaxation of the devices remained similar after prolonged operation. This consistency coupled with the sensitivity of the SnO_x memristors to input voltage amplitude and pulse-width indicated suitability for signal processing tasks.
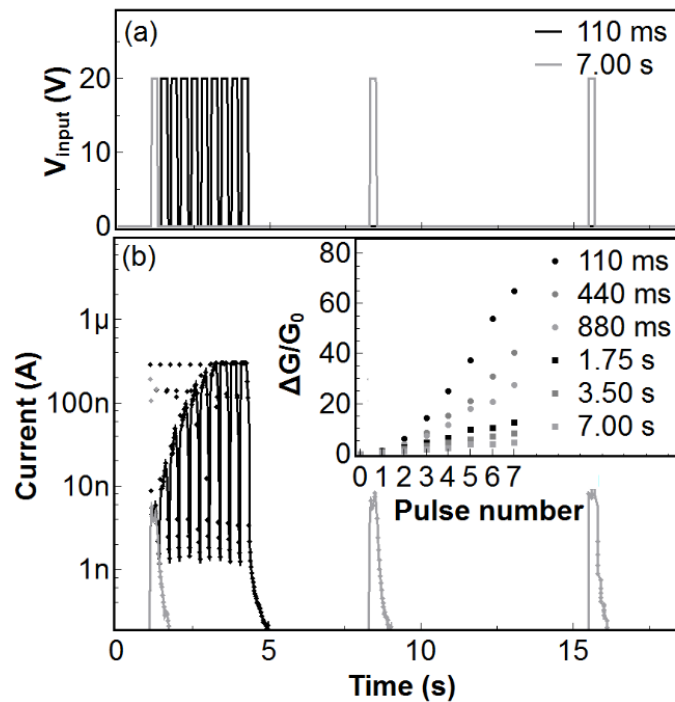
Figure 5-11: (a) Input voltage pulse sequences applied to the SnO_x memristor device with 110 ms and 7.0 s inter-pulse intervals, (b) evolution of device current and (inset) conductance as a function of the inter-pulse interval, resembling PPF. (Pulse amplitude = 20 V and pulse width = 200 ms).

5.3.5 Harmonic generation

Filamentary memristors have been demonstrated to generate second-order harmonic under sinusoidal voltage stimulus [274]. Figure 5-12(a) shows the frequency response of a memristive tin oxide device to 8V peak-to-peak, 9.25 Hz sinusoidal inputs – this frequency was chosen for comparison with similar experiments performed in [275]. Only second-order harmonics were observed in the device when the peak-to-peak voltage varied from 3 V to 13V (not shown). The sharpness of the fundamental and second-order harmonic peaks is indicative of single filamentary devices with transport-limiting Schottky barriers rather than recurrent neural networks with multiple active pathways that change spontaneously during operation [194]. Nevertheless, second-order harmonic generation from memristive devices has been suggested for use in some areas of analog signal processing [276]. Figure 5-12(b) demonstrates the increase of the relative amplitude with the increase of the peak-to-peak voltage. Whilst filamentary memristors have been reported to provide relatively low harmonic power but in combination (such as in four memristor bridges), they can offer a higher ratios [274].
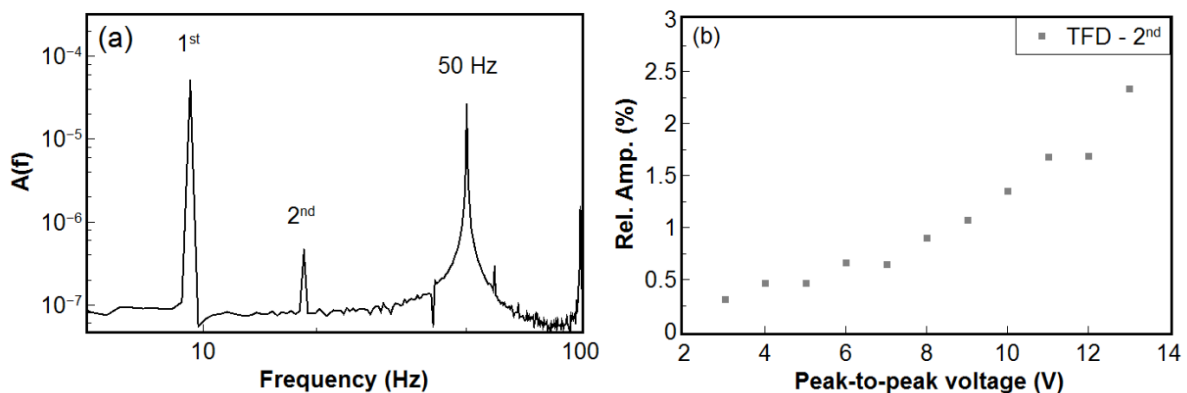
Figure 5-12: (a) Amplitude spectra obtained after Fourier transformation of responses from a memristive tin oxide device to 8V, 9.25 Hz sinusoidal input signals. (b) Relative amplitudes of second-order harmonics generated in the device as a function of bias voltage.

5.3.6 Implementation of the memristive tin oxide thin film devices

The memristive SnO_x thin film devices exhibit sensitivity to the intensity, and duty cycle of input voltage pulses, enabling operation suitable for signal processing. In this section, pulse sequence recognition and spectrum analysis applications are demonstrated as examples of capabilities of the devices. This work shows there is potential for the memristive tin oxide devices to be exploited in reservoir computing circuits, a neural network-based computing paradigm that enables efficient processing of time varying inputs [277].

Figure 5-13 shows a typical device response to six different 4-bit binary input voltage pulse sequences. One such sequence (0110) is shown for example in Figure 5-13(a). The pulses representing logic state '1' were 250 ms duration with 22.0 V amplitude (which exceeded the threshold voltage for switching to LRS). Non-perturbative read-out was performed using a 2.5 V DC potential. The device exhibited the same systematic PPF exemplified in Figure 5-11 and after the six differing input pulse sequences, unique conductance states were returned (Figure 5-13(b)). Three similar memristor devices were operated with the same voltage pulsed input sequences and these all provided the same pattern recognition outcome; unique conductance states ordered identically from low to high according to the input sequence (as shown in Figure 5-13(b)). In a recent report, Du et al. demonstrated memristors with active layers of WO_x exhibiting similar pattern recognition capability [200]. It is stated that with consistent short-term memory storage and relaxation, the devices were suitable elements for reservoir computing [277].
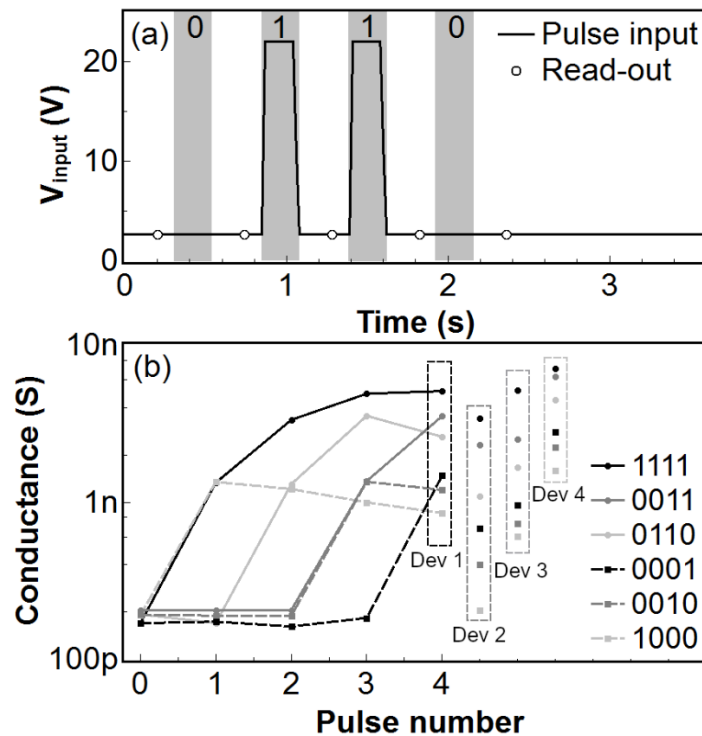
*Figure 5-13: **(a)** Typical input voltage pulse sequence (representing 0110) applied to tin oxide memristors with post-pulse conductance read-outs shown as unfilled dots and **(b)** the evolution of the device conductance during and after six different four-pulse input sequences with the final states of three similar devices also shown.*

Finally, the analysis of spectral data using single SnO_x devices was explored. Figure 5-14 shows the device currents measured shortly after input of two sequential overlapping Gaussian pulses. This could represent a set of arbitrary XPS 1*s* spectra showing two different chemical states with varying composition, each spectrum being normalised with respect to intensity and converted to an input voltage

wit the binding energy converted to time to simulate real time analysis during XPS data collection (with the higher binding energy Peak 'A' input arriving sooner than Peak 'B'). Figure 5-14 shows that unique output currents are observed for each spectrum, enabling approximate quantification. The output current is higher when the two peaks are similar in magnitude than when they are dissimilar. The higher curent results from the larger spectral integral. Larger output currents are observed for equivalent spectral integrals when Peak 'B' is larger than Peak 'A' (e.g. ratios of 1:0.2 and 0.2:1). This is due to the longer relaxation times resulting when a higher voltage pulse is more-recently applied. Similar signal processing methods should be applicable to restricted ranges of spectra from different techniques (e.g. mass spectrometry, Raman spectroscopy). Importantly, this highlights the potential for rapid spectrum image analysis using multiple memristive SnO_x devices.
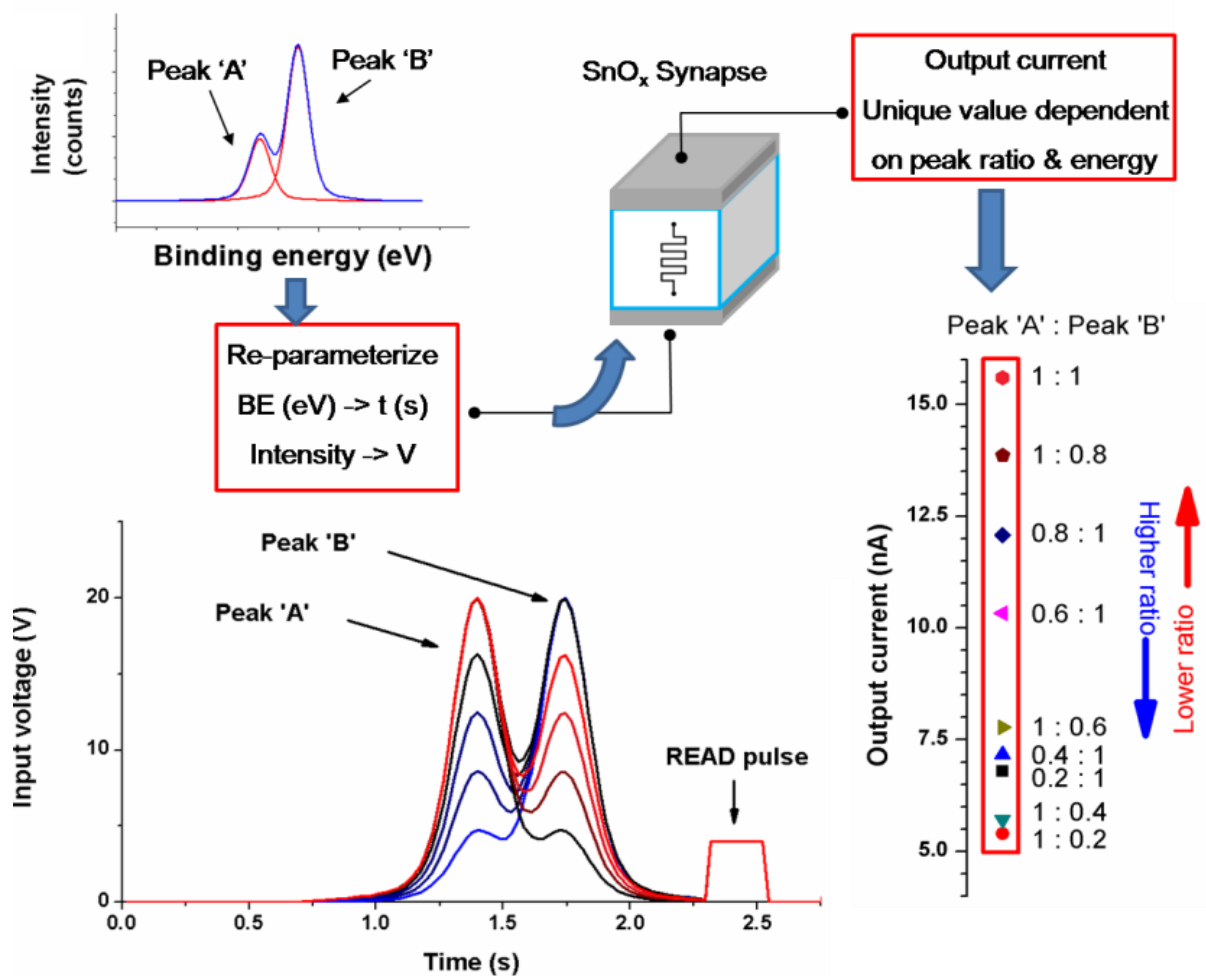
Figure 5-14: Example of spectral analysis using a single SnO_x device. The simulated 1s XPS data is re-parameterized so that its normalised peak intensity is converted to input voltage (V) and the binding energy (BE) is converted to the input time parameter (t).

5.4   Summary

In summary, lateral memristors consisting of Pt electrodes supported on mixed phase tin oxide and separated by sub-micron gaps have exhibited forming-free volatile bidirectional resistive switching and activity dependent conductance. In the LRS, a nanoscale conducting filament forms within the device layer after Joule heating induced decomposition of the minority SnO phase and passivation of Sn (II) acceptor states. When the voltage and current are removed, relaxation occurs due to back-diffusion of oxygen into the filament and quenching. With consistent short-term potentiation and relaxation characteristics, the devices return unique conductance states from differing logic pulse input sequences. Tin oxide is a low-cost material with proven suitability for p- and n- doped thin film transistors but as this work shows, it also supports memristive behaviour suitable for bio-inspired pattern recognition systems.

Chapter 6:

Resistive switching nanoparticle networks self-assembled in mixed phase tin oxide

In this chapter, a facile, top-down, method for assembling electrically-contacted, resistive-switching random networks is reported. This involves the investigation of formation of the nanoparticle networks in mixed phase tin oxide thin films, their resistive switching mechanism and the synaptic-like behaviour of such self-assembled nanoparticle network devices. The aim of this work was to determine the memristive characteristics of the networks and their potential for use in applications including reservoir computing.

Chapter 6: Resistive switching nanoparticle networks self-assembled in mixed phase tin oxide

6.1 Introduction

With potential applications in next generation non-volatile random-access memories and bio-inspired computing, memristors have attracted significant research interest over several years [141, 142, 250]. Numerous materials have been employed as active memristive layers and in most of these, the defects/impurities migrate in the applied electric field to produce high resistance state (HRS) and low resistance state (LRS) device switching. Examples include metal oxides such as TiO_2 [141, 160, 278], $HfO_{2-x}N_x$ [261], NbO [266, 279] and others such as Si [280] and C [281]. In addition, distinctly different memristive devices can be formed from networks of nanoparticles or nanowires [194, 282-284]. These nanoparticles or nanowires are normally metallic with surrounding shells composed of an insulating or semiconducting material. The nanoparticles/wires are typically formed remotely then deposited as a film onto an appropriate surface, often with pre-formed electrodes [283, 284]. This can be achieved in vacuum, using apparatus such as inert gas aggregation systems [283], by drop-casting [285], dielectrophoresis [286], or by other wet chemical methods [287]. The resistive switching mechanism is normally attributed to lowering/removal of the potential barriers separating the individual nanoparticles or nanowires and formation of conduction path(s) through the (initially) highly-resistive network. Application of electric-field and/or passage of current is an effective means to achieve this by inducing electromigration and/or Joule heating related defect/impurity motion [194, 283]. Devices based on this architecture have demonstrated rich memristive behaviour including quantized conduction [288, 289], emulation of biological synaptic functions such as short- and long- term plasticity [194-196], photo-sensitive memristance [275, 290] and memristance modulated by bio-molecule attachment [291, 292]. Perhaps most significantly, these complex networks are suited to reservoir computing [194, 275] in which the term 'reservoir' describes a complex network of switching elements that transform input signals into a higher dimensional space [197, 277, 293]. After suitable training of their "output layers", reservoir computing circuits have completed tasks such as pattern recognition, signal processing and disease detection [200, 210-213] with high efficiency.

This chapter presents resistive switching nanoparticle networks self-assembled in films of tin oxide deposited at room temperature. It was shown in Chapter 5 that semi-insulating mixed-phase tin oxide ($SnO_{1.9}$) can exhibit memristance caused by decomposition of the SnO phase and formation of Sn-rich conducting filament(s). The memristive properties reported here (Chapter 6) arise due to a different mechanism and device morphology. The as-deposited semi-insulating (flat) tin oxide film is transformed, by the application of an electric field and passage of current, into a dense nanoparticle network exhibiting bidirectional threshold switching and other memristive characteristics. Lateral device architectures were employed to facilitate morphological and compositional analysis pre/post formation which is then discussed in relation to the electrical characteristics.

6.2   Experimental details

The network devices were fabricated between pre-formed planar electrical contacts on the tin oxide thin film. The film was deposited at room temperature using a high-power impulse magnetron sputtering (HiPIMS) system with process parameters described in Chapter 5. The 20 nm thick platinum contacts to the devices were defined using electron beam lithography (FEI Nova NanoSEM) and Pt coating (Gatan PECS ion-beam deposition system). An atomic force micrograph of a four – electrode device is presented in Figure 6-1. The separations between (opposite) contacts of the two and four – electrode devices ranged from approximately 300 nm to 500 nm.

The compositions of the as-deposited tin oxide samples were determined using a Thermo Scientific K-alpha X-ray photoelectron spectroscopy (XPS) system with mono-chromated Al K-α source. The oxidation states were revealed using Auger electron spectroscopy performed on a PHI 710 Scanning Auger Nanoprobe (SAN) (Physical Electronics, Chanhassen, USA) utilising a field emission electron source and a coaxial single pass cylindrical mirror analyser for electron energy analysis. The source was operated at 10 kV, 1 nA for spectroscopy and microscopy studies. Transmission electron microscopy (TEM) and electron energy loss spectroscopy performed in a JEOL 2100F system operating at 200 kV were also used to identify the composition of the tin oxide region between contacts after electrical forming and switching. An Asylum Research MFP-3D Infinity atomic force microscope (AFM) provided surface topography and step-height measurements.

With the device mounted on a probe-station, a Keysight B2902A twin channel source-measurement unit (SMU) enabled both initial electroforming and subsequent acquisition of two-probe current-voltage (I-V) characteristics. For four – electrode memristors, the second channel of the SMU was employed. A current limit (I_{limit}) of 100 nA was imposed during the measurement. Unless otherwise stated, all electrical and scanning-probe measurements were performed at room-temperature in air.
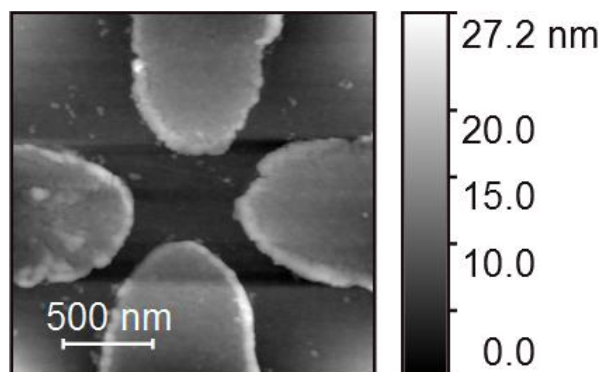
Figure 6-1: Atomic force micrograph of a pristine four Pt-contacted SnO$_x$ memristor:

6.3 Result and Discussion

6.3.1 Compositional analysis of the as-deposited tin oxide film

XPS did not reveal any features attributable to metallic Sn but based on other reported work [114], Sn clusters are expected to exist in the mixed phase, as-deposited films. The concentration of these Sn clusters is expected to be higher in tin oxide device layers containing less oxygen and as shown later, the off-axis deposition method has enabled investigation of the significant effects of stoichiometry on the device characteristics. Despite the small variations in the Sn:O composition caused by the off-axis deposition, very similar Sn 3d, O 1s and VB spectra were observed from all the device layers (Figure 5-6 and Figure 6-2). The dominance of Sn^{4+} (or SnO_2) and the presence of the minority SnO phase are illustrated in the XPS spectra. All films exhibited mixed phase composition with SnO_2:SnO ranging from 1:0.30 to 1:0.18 from Sn-rich to O-rich sides of the wafer. The difference in Sn:O composition leads to the formation of two different devices, referred to as filamentary devices (FDs) (described in Chapter 5) and nanoparticle network devices (NNDs) (see later). Devices described in this chapter were fabricated using HiPIMS deposited tin oxide with composition of 1(Sn):1.85(O) and SnO_2:SnO of 1:0.18, calculated from XPS.
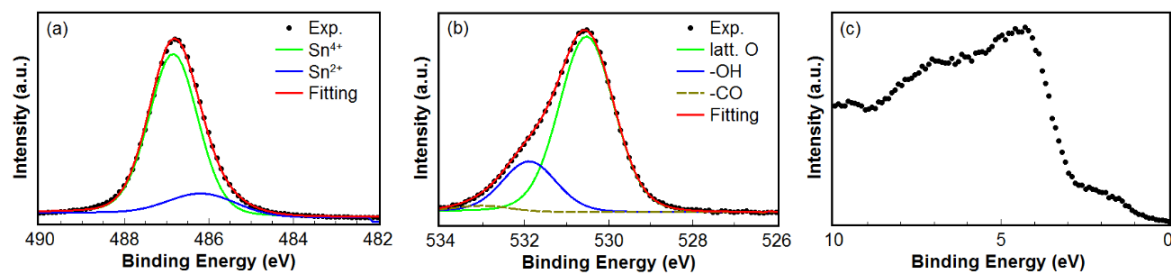
Figure 6-2: X-ray photoelectron spectra from the SnO_x film in the (a) Sn 3d, (b) O 1s and (c) valence band regions. Fitting of the peaks indicates the phase composition and surface adsorbates.

6.3.2 Dual-electrode memristive nanoparticle network devices

6.3.2.1 Electroforming process in memristive nanoparticle network tin oxide devices

The memristive devices described in this chapter show similar volatile bidirectional threshold switching behavior as FDs described in Chapter 5. However, when higher-than-usual voltage (or electric field) or high voltage for a long time is applied, an electroforming process is observed in these devices. The evolution of the electrical characteristics during electroforming are shown in Figure 6-3. The pristine device (with Sn:O of 1:1.85 and SnO_2:SnO of 1:0.18) exhibits high resistance (>10 GΩ, path 1) at low bias and the I-V relationship is approximately linear. The data has a unity slope in the natural logarithm I-V plot (see inset of Figure 6-3). This is consistent with transport limited by back-to-back (Pt-SnO_x-

Pt) Schottky diodes. In this device configuration, carrier emission over the potential barriers is excluded and direct tunneling is the dominant transport mechanism. With an applied voltage of 27 V, the current increases sharply and negative differential resistance (NDR) is observed (path 2). Immediately after forming, the device enters its LRS (path 3) but at a higher voltage (and power) it returns to the HRS (path 4). When the voltage is decreased, there is a return to the LRS (path 5) followed by a return to the HRS (path 6). This chaotic and volatile behavior suggests the conduction path(s) established in the forming/set process are thermodynamically unstable. Different samples exhibit different electroforming behaviors (shape, electric fields where the transitions occur) although most often, they are composed of HRS (path 1), NDR (path 2), LRS (path 3) and volatile property (path 6). Post electroforming, the threshold voltage decreased significantly, and the device exhibited stable I-V hysteresis with distinct HRS and LRS separated by more than two-orders of magnitude (shown later).
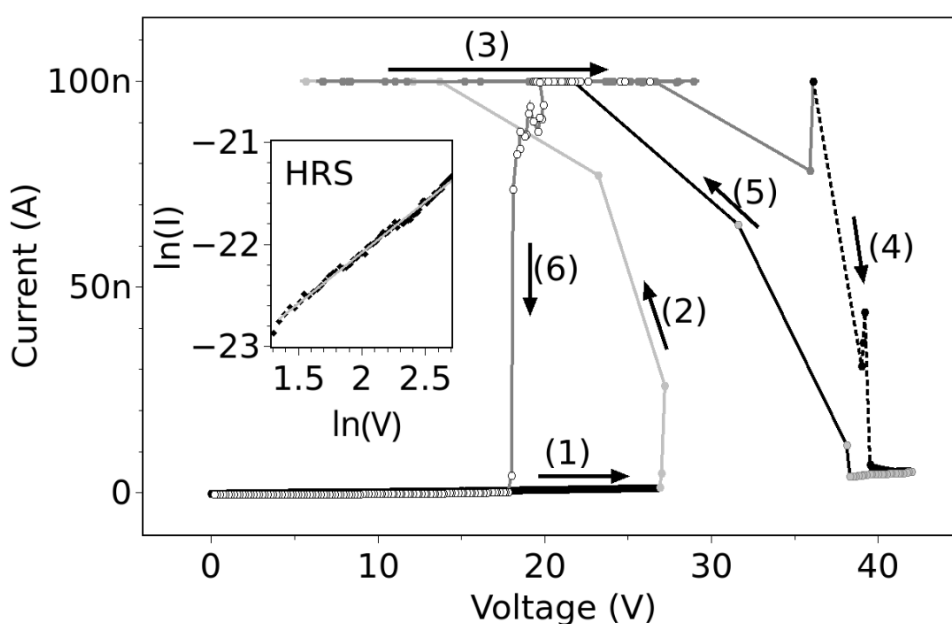
Figure 6-3: Current-voltage characteristic (V swept from 0 to 42 to 0 V, I_{limit} = 100 nA) showing the forming event and subsequent reset/set events. The inset shows that in the pristine state, current transport initially fits a direct tunnelling model with I proportional to V.

6.3.2.2 *Morphological/compositional analysis of memristive nanoparticle network tin oxide devices*

After the electroforming process, the morphological/compositional changes that accompany the onset of resistive switching were determined as shown in Figure 6-4. The region between the planar Pt electrodes is very different to the surrounding unmodified tin oxide layer. In contrast to the (as-deposited) flat film, it resembles a densely packed but porous network of nanoparticles. This change in morphology was observed immediately following the electroforming sweep in several similar devices. A nanoparticle network could be formed in a small area (Figure 6-4 (a)) or the whole region (Figure

6-4 (b)) between two contacts, depending on the applied electric field and the electroforming time. Figure 6-4 (c) illustrates the evolution of particle size and number after additional sweeps. The particle analysis result shows that further sweeps initially increase the number of particles (area of particle network), and then cause significant coalescence, resulting in larger average nanoparticle diameter. Theses morphological changes are due to partial melting by Joule heating.
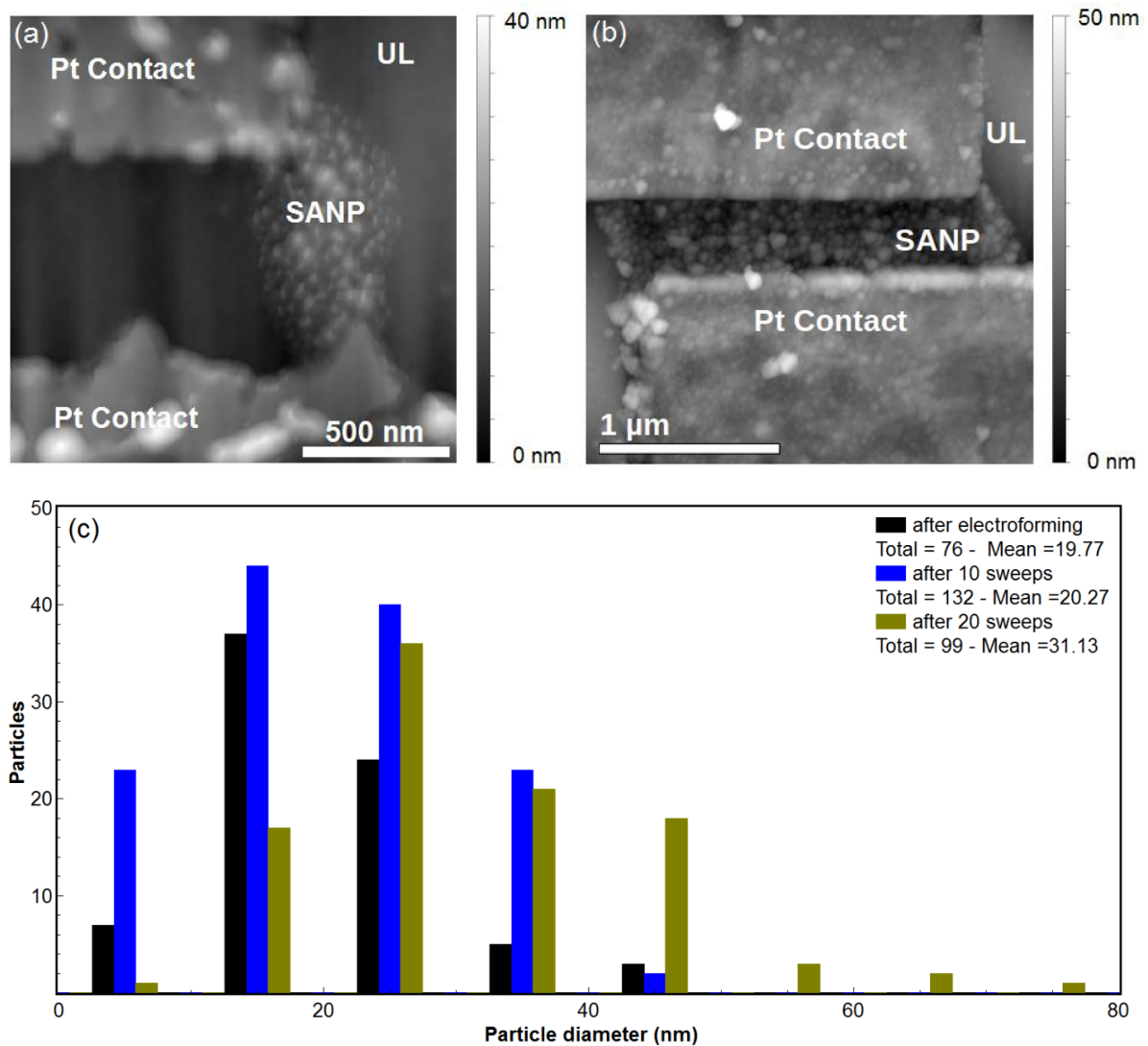
Figure 6-4: Atomic force micrograph taken for two devices after electroforming to give a nanoparticle network (a) in a small area (device #1) and (b) in the whole region between two contacts (device #2). The self-assembled nanoparticle network (SANP) and unmodified layer (UL) are visible. (c) Particle analysis based on AFM images of the SANP device #1 after electroforming and numbers of sweeps.

Joule heating has been reported to cause local temperature exceeding 1000°C within many memristive devices [268]. Decomposition of SnO (the minority phase in the device layer) is known to occur above 300°C [242] and when SnO decomposes, its products are SnO_2 and Sn [242]. Since interstitial Sn is an n-type donor in SnO_2, this leads to significantly increased conductivity. In the device electroforming

characteristics in Figure 6-3, this expected rapid increase in conduction is consistent with 'Path 2' and again, the morphological change is attributed to partial melting by Joule heating. In the ambient conditions, this melting is followed by rapid cooling and re-oxidation of the nanoparticles when the voltage and current are reduced. Hence, relaxation back to the HRS occurs within the nanoparticle network. Interestingly, this transformation does not occur in films that are relatively oxygen poor. Samples taken from locations on the wafer that were closer to the Sn magnetron gun during deposition and therefore with higher Sn relative to O exhibit resistive-switching but as shown in section 5.3.1, this arises due to a filamentary conduction path within a substantially unmodified device layer.

The composition of the nanoparticle network was investigated using Auger electron spectroscopy (AES). Figure 6-5 shows spectra obtained from the as-deposited layer and from the nanoscale area between the Pt contacts after electroforming. The alterations in peak intensities and positions before/after electroforming are consistent with a change in AES, the dominant oxidation state from SnO_2 to SnO [294]. Hence, the film loses oxygen as it is transformed into the network. The method employed lacked sufficient resolution to determine the composition of the individual nanoparticles but given that all electrical measurements were performed in air, it is most probable that the nanoparticles were more oxidized at their surfaces i.e. they possessed a compositionally graded structure with the core being Sn-rich and the outer surface being more O-rich.
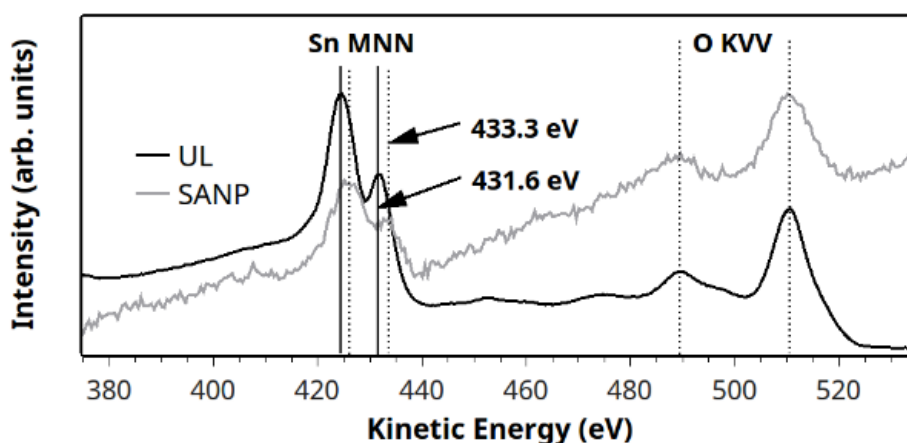
Figure 6-5: Auger electron spectra taken from the NND after electroforming. UL and SANP denote for unmodified layer and self-assembled nanoparticle network.

To support the AES measurements, high resolution transmission electron microscope (HR-TEM), electron dispersive X-ray spectroscopy (EDS) and (c) electron energy loss spectroscopy (EELS) analyses were carried out. The nanoparticle network is well-observed in the scanning electron microscope (SEM) image of the NND (Figure 6-6 (a)) obtained in a FEI Verios 460L field-emisson (FE) SEM. A region including contacts and the nanoparticle network, called a region of interest (ROI)

(dashed box in Figure 6-6 (a)), was cross-sectioned using mechanical polishing followed by ion beam thinning. The cross-section of this ROI is illustrated in the HR-TEM micrograph (Figure 6-6(b)). Electric field and Joule heating have little or no influence on the areas which are far away from the clustered region (e.g. close to the left or right edge in Figure 6-6(b)). Therefore, the structure of this region remains Pt/SnO$_x$/SiO$_2$/Si where Pt and SnO$_x$ film (both are dark) do not have a high contrast with each other but can be distinguished from the bottom SiO$_2$ (light grey) and Si layer (dark grey) in Figure 6-6(b). Closer to the highly active layer (right on the left of the clustered region in Figure 6-6(b)), nanoparticles start appearing and diffuse to the SiO$_2$ layer. This is thought to be attributed to Joule heating which causes a partial melting for both SnO$_x$ and SiO$_2$ layers. The melting temperatures of tin oxide (1630 °C) and silicon dioxide (1710 °C) are similar. This is consistent with the imperceptible SnO$_x$ layer and the existence of a clustered zone within the SiO$_2$ layer in the active region between two contacts.

Elemental analyses acquired from the EDS mapping along the TEM cross-sectional line scan passing over the clustered region (indicated in Figure 6-6(b)) are illustrated in Figure 6-6(c). The region from 0 to 15 nm is a part of the Si substrate, hence Si is the dominant element. Below the interface between the SnO$_x$ and SiO$_2$ layers (~65 – 70 nm consistent with 50 nm thick SiO$_2$ grown on Si substrate), a small amount of Sn is observed. This is in a good agreement with diffusion of Sn into SiO$_2$ in the discussion of Figure 6-6(b). The SnO$_x$ layer is hardly seen in the active region between two Pt contacts in Figure 6-6(b), however, the considerable amount of Sn and O above the SiO$_2$ layer (from 70 to 90 nm in distance axis) implies the existence of Sn and O combination with a thickness of ~20 nm. Pt is also detected in the Sn-O layer as it was deposited to protect the device from damage due to the FIB milling process.

Figure 6-6(d) shows the electron energy loss spectra of Sn-M$_{5,4}$ and O-K edges along the EELS cross-sectional line scan passing over the clustered region (indicated in Figure 6-6(b)). Also, an EELS spectrum in core-loss region taken from a small area of the unmodified SnO$_x$ film of the device (close to the right edge in Figure 6-6(b)) is illustrated in Figure 6-6(d) as a reference (black curve in the top panel). According to the reference spectrum, the difference in energy loss between the Sn - M_5 edge (at ~493 eV) and the first peak of O – K edge (at ~540 eV) is estimated to be 46 eV which is close to the value for SnO or intermediate tin oxide phase (a mixture of Sn(II) and Sn(IV)) reported in [295] and larger than that of SnO$_2$ which is in the range of 42.4 to 43.6 eV [295]. Moreover, the rounded peaks at 523 and 531 eV, due to the M_5 and M_4 edges (known as delayed edges) are hardly visible in the pure SnO phase [295]. Therefore, the measurements show that the unmodified SnO$_x$ region of the device is of intermediate tin oxide phase. This agrees with the XPS and Auger results described before (Section 6.3.1).
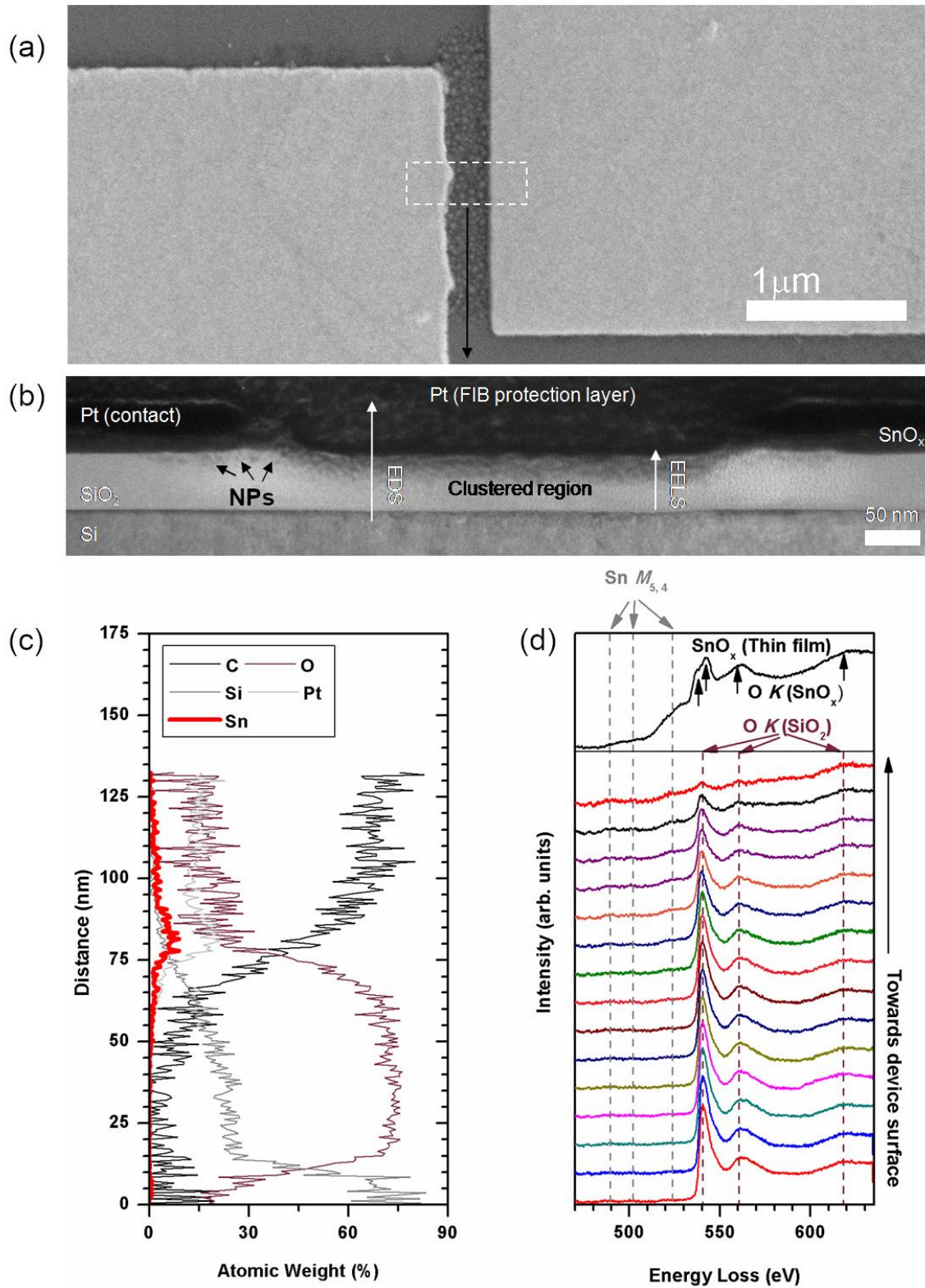
Figure 6-6: (a) SEM image of a two-contact tin oxide NND (the dashed box indicates the milling part of the device using FIB). (b) HR-TEM image of the NND cross-section. (c) The energy-dispersive X-ray spectroscopy (EDS) elemental analysis and (d) the Sn $M_{5,4}$ and O K edge profiles along line scans across the Pt/SnO$_x$/SiO$_2$/Si structure indicated in (b) using electron energy loss spectroscopy (EELS). The top black line in the upper panel of (d) is collected from a small area of the unswitched SnO$_x$ film.

Turning to the EELS spectra of the core-loss edges along the EELS cross-sectional line scan, the features due to Sn - M_5 and Sn – M_4 edges at 489, 502 and ~525 eV become more obvious toward the device surface. This is again evidence of Sn existing in the clustered region [295, 296]. However, it is difficult to identify oxidation states since $M_{5,4}$ edge spectra are weak in intensity and broad in energy.

Figure 6-7 demonstrate the referenced electron energy loss (EEL) spectrum of tin (Sn) [297] and the EEL spectra of SiO_2 and nanoparticles of the NND in the low-loss region where the energy loss is up to few tens of electron volts and is caused by inelastic scattering by conduction and valence electrons [298]. The low-loss spectrum collected from the nanoparticles has an additional peak at ~14 eV, when compared to the SiO_2 spectrum. This peak is thought to be attributed to Sn as its position corresponds to the Sn peak in the reference data. As a result, the nanoparticles are identified as Sn rich nanoparticles.
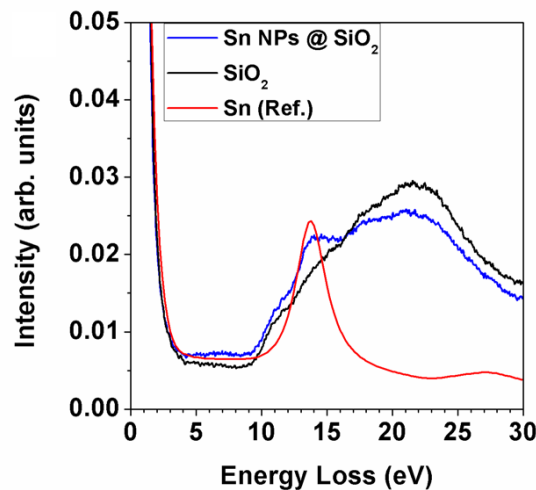
Figure 6-7: EELS data of the SiO₂, and the tin nanoparticles in the NND and the reference EELS data for Sn [297] in the low-loss energy region

6.3.2.3   *Resistive switching in memristive nanoparticle network tin oxide devices*

Figure 6-8(a) shows typical I-V characteristics obtained after the forming sweep shown in Figure 6-3. These measurements, taken with a 100 nA current limit imposed and with one complete sweep taking 18 s, show I-V hysteresis characteristic of memristors. The device again exhibits volatile resistive switching behaviour. The dominant transport mechanisms in the HRS and LRS differ as shown in Figure 6-8(c) and (d). In the low-bias region of the HRS (Figure 6-8(d)), transport is limited by Schottky emission but at higher bias close to the switching threshold, direct tunnelling (not shown) dominates. In the LRS (Figure 6-8(d)), the I-V characteristics are initially consistent with transport limited by Fowler-Nordheim tunnelling. Based on equation eq. 5-2, the barrier width corresponding to the IV data is ~4.8 nm, which is thin enough for tunnelling and is in agreement with prior work [256-258]. This indicates that in the LRS, there is(are) critical tunnel junction(s) within the conduction path that limit

the current flow. As the voltage across the device falls below 2.0 V, the current diminishes rapidly, and the device relaxes back to the HRS (as shown in Figure 6-3).

To assist in determining the mechanisms causing the memristance in the tin oxide nanoparticle network devices (NNDs), comparison between NNDs and tin oxide FDs which are formed in similar (but not identical) mixed-phase material is made. These distinctly different memristive mechanisms are caused by the (slightly) different phase compositions of the as-deposited layers in the NNDs and FDs. The more Sn-rich FD tin oxide layers likely contain a higher concentration of Sn clusters relative to the tin oxide NND layers and it is believed that the higher density of clusters assists in establishing an initial conduction path. Joule heating along this conduction path then results in cluster-linking and a filament which localizes the device current and the associated Joule heating. The surrounding layer passes little current and therefore remains unaltered. The FDs can be operated with higher current limits (up to 300 nA) without morphological transformation occurring (see chapter 5). Above this limit, the filamentary region melts and the FDs then either exhibit no switching or chaotic switching. In either case, formation of nanoparticle networks like those in Figure 6-4(a) and (b) does not occur.

In the NNDs, switching to the LRS occurs (during electroforming) at a higher (~30%) threshold voltage/field related to the FDs. The density of Sn clusters is expected to be lower in the more oxygen-rich as-deposited layer in the NNDs. With a higher current, the NPD device reaches a higher temperature during the electroforming process. Decomposition of the SnO phase is expected to increase conductivity and as the temperature rises further, the entire region of the device layer between the contacts becomes molten. Surface-energy minimisation and Ostwald ripening processes ultimately lead to the nanoparticle network morphology shown in Figure 6-4(a) and (b)
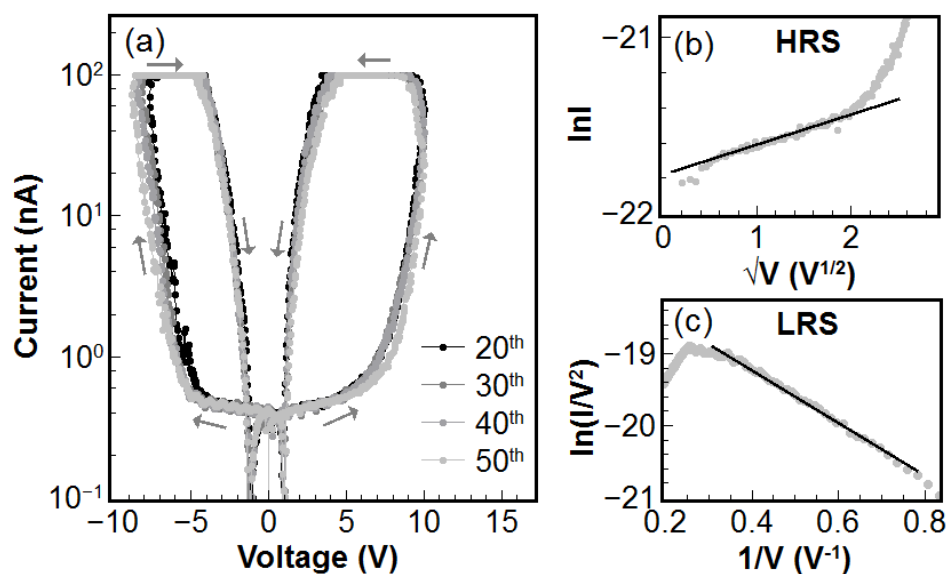
Figure 6-8: (a) I-V characteristics of the lateral memristor with 100 nA current limit imposed during measurement, (b) fitting of HRS and (c) Fowler-Nordheim fitting of averaged (20th,30th,40th,50th) LRS characteristics.

Bidirectional resistive switching characteristics from a FD (Figure 5-2(a)) resemble those of the NND but differences provide some insight into the underlying mechanisms. In the HRS (Figure 6-8(b)), the transport mechanism is characteristic of Schottky emission, as it is in NNDs. In the LRS (Figure 5-3(b)), the FDs produce ohmic I-V characteristics. In these devices, a filament extends between the contacts when the LRS is entered. This filament must short out the Schottky barriers at the contacts for ohmic conduction to occur. When the voltage/field is removed fitting show that the device current is once again limited by Schottky barriers. This is consistent with rupture of the filament and removal of the parallel connection across the Schottky barriers. Importantly, this memristive mechanism prevents the recurrent behaviour exhibited by some neural networks and by some atomic/nanoparticle switching networks [194].

Switching from HRS to LRS in the NNDs could occur by multiple mechanisms. As the voltage and current increase in the HRS, Joule heating causes an increase in the free electron concentration and a corresponding increase in the tunnelling current. Thermal expansion will occur within the network and this may narrow the tunnel gap. Again, there may also be decomposition of the minority phase, as in the FDs. Significant re-configuration of the network or relocation of the conduction path seems unlikely when inspecting the highly reproducible switching characteristics shown in Figure 6-8(a). AFM images and particle size analysis performed after 1, 10, 20 sweeps support this assertion.

Temperature-dependent current-controlled I-V characteristics in air for an NND are shown in Figure 6-9(a), s-type negative differential resistance (NDR), similar to those in tin oxide FD (Figure 5-4) and in other metal oxides (e.g. VO_2 [260], Ti_4O_7 [262] and NbO_2 [263]) is observed clearly. As mentioned in Section 5.3.2, this behaviour can result from a temperature-induced Mott insulator-to-metal transition (IMT) or a combination of Joule-heating and Poole-Frenkel conduction.

Differing from the current-controlled NDR (CC-NDR) of the tin oxide FD (Section 5.3.2) and other metal oxides in which voltage decreases with the increase of device temperature, the CC-NDR of the NND (Figure 6-9(a)) has two stages: (i) the increase of voltage (or resistance) as temperature is increased from 283 K to 308 K and (ii) the decrease of voltage (or resistance) as temperature is increased from 308 K to 348 K. The first state is thought to result from the oxygen adsorption occurring on the surface of the tin oxide layer of the device. At low temperatures, molecular forms (i.e. neutral adsorbed $O_{2(ads)}$ or charged adsorbed $O_{2(ads)}^-$) are produced on the SnO_2 surface, while atomic forms (i.e. neutral adsorbed $O_{(ads)}$ or charged adsorbed $O_{(ads)}^-$ or $O_{(ads)}^{2-}$) are dissociated from neutral adsorbed $O_{2(ads)}$ at high temperature (eq. 6-1) [299, 300].

$$O_{2(g)} + e^- \rightarrow O_{2(ads)}^-$$

$$O_{(ads)} + e^- \rightarrow \ O_{(ads)}^- \ \ or \ \ O_{(ads)} + 2e^- \rightarrow \ O_{(ads)}^{2-} \tag{6-1}$$
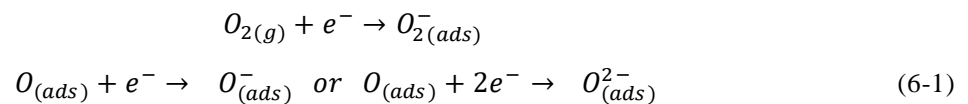
where $O_{2(g)}$ is oxygen in its free state.
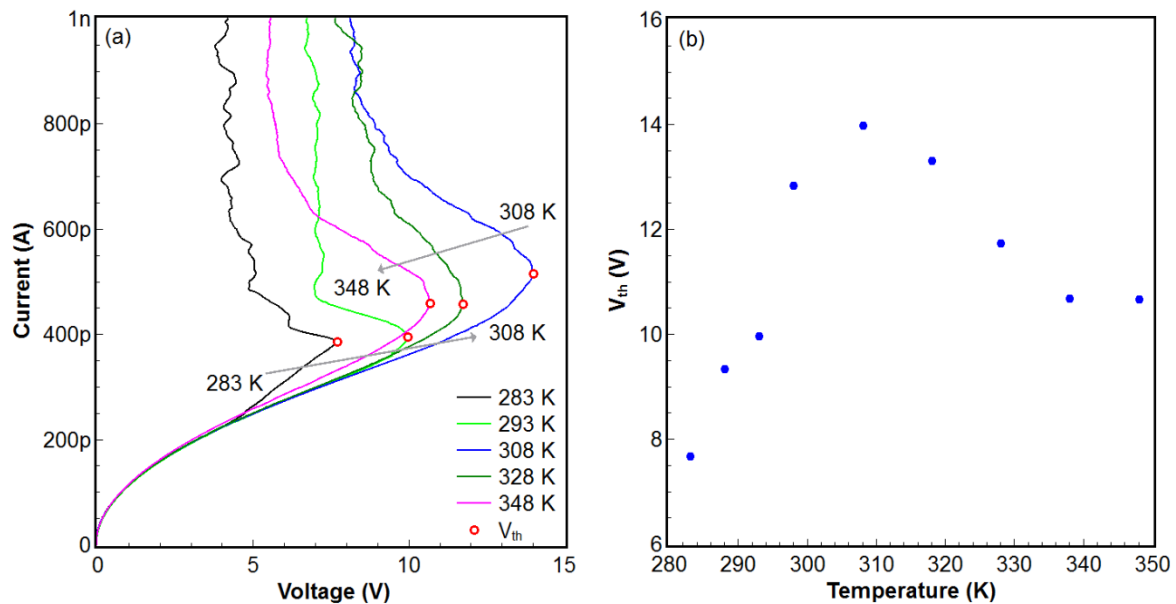
Figure 6-9: (a) Temperature-dependent I-V characteristics of the lateral memristive tin oxide NND with 15 V voltage limit imposed during measurement. (b) Threshold voltage V_{th} as a function of device temperature.

The oxygen adsorption leads to the increased upward band bending and the broader depletion region [299, 301], and consequently the decrease of electron density near the surface and/or the widening of the oxygen-rich separating layers between nanoparticles. As a result, the device conductance drops at low temperature. The stage (ii) which has been observed in reports of tin oxide [302, 303] is due to thermal excitation of charge carriers. Figure 6-9(b) shows the threshold voltage as a function of the device temperature. The threshold voltage increases with the increased temperature, and then reaches a peak at 308 K before reducing when temperature is higher than 308 K.

6.3.2.4 Light sensitivity of tin oxide nanoparticle network devices

Figure 6-10 shows the I-V characteristics of an NND when exposed to UV illumination (wavelength = 310 nm, power density 100 μW/cm^2) and in dark environment. These results show that the response (in LRS and HRS) exhibited by the NND upon illumination is not solely due to (parasitic) photoconductivity in the surrounding unmodified film. More importantly, the higher sensitivity to UV in the NPD is consistent with the tunnelling-limited conduction discussed prior.

The current in the HRS below the threshold voltage is increased less significantly in the FD (shown in Figure 5-8). This increase is due to photo-conductivity in the unmodified semi-insulating device layer. In the NND, the HRS current increases more significantly upon illumination. This higher response is

attributed to the porous structure and the tunnel barriers between the nanoparticles. In the NND, the excitation of free carriers by the UV illumination causes both an increase in carrier concentration and an increase in tunnelling probability (since the energy of the free carriers relative to the tunnel barrier increases as states in the CB are filled).

The NND also exhibits a greater increase in LRS current relative to the FD (Figure 5-8). This difference is consistent with expected behaviour for devices with metallic-like filaments versus devices with transport limited by tunnel-barrier(s) between adjoining nanoparticles. In the LRS, the FD has a large free carrier concentration due to the heavily doped filament connecting the contacts. Hence, the promotion of carriers into the conduction band alters the conductance of the FD (filament) less significantly. In the NND, the free carrier concentration in the semiconducting nanoparticles is more significantly increased by the UV illumination and this causes a corresponding increase in the tunnelling current.
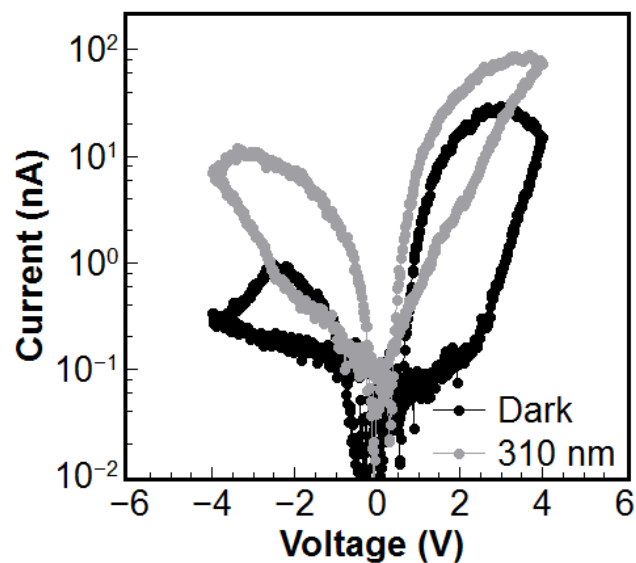
Figure 6-10: I-V characteristics for a SnOx thin film device in dark and ultraviolet – illuminated (310 nm, 100 μW/cm²) conditions.

6.3.2.5 Activity – dependent conductance of tin oxide nanoparticle network devices

As emulation of biological synaptic functions such as short- and long- term plasticity is reported in several nanoparticle/nanowire network devices [195, 196], tin oxide NNDs are expected to mimic some aspects of synaptic behaviour. The temporal dynamics of NNDs were hence investigated. Figure 6-11 shows the evolution of the conductance of an NND during 5 trains of 10 consecutive pulses with amplitude of 10 V, pulse width of 100 ms an inter-pulse interval varied from 100 ms to 500 ms. The conductance is increased according to the number of pulses and the frequency at which the pulses are

applied. The increased current following successive pulses is analogous to paired-pulse facilitation (PPF) in biological synapses and follows a similar trend to these systems in that shorter inter-pulse intervals result in increased conductivity [252, 304].

It is believed that with longer inter-pulse intervals, heat dissipation increases, causing the conductance increase to be smaller. In the first few pulses, the device conductance increases rapidly due to the gradual formation of conduction path(s). After that, additional pulses appear to provide insufficiently high current and heat to generate more carriers and/or to reduce the gap between nanoparticles. However, they do maintain the conductance level, as shown by conductance saturation in Figure 6-11. Other measurements carried out on FDs (Figure 5-9 and 5-10) were employed on NNDs to explore the dependence of NNDs on the intensity and time of stimuli. Like FDs, NNDs exhibit their sensitivity to input voltage in addition to temporal effects, therefore amenable to signal processing appllications.
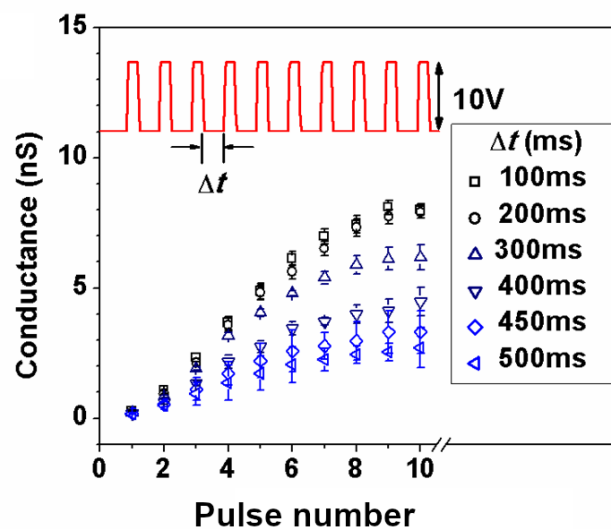
Figure 6-11: Conductance evolution in response to voltage pulse trains of varied inter-pulse interval Δt.

6.3.2.6   *Harmonic generation and recurrent network dynamics*

It has been demonstrated in atomic switching networks [194, 275] and single memristors [274] that second-order harmonic generation occurs under sinusoidal voltage stimulus. Figure 6-12(a) shows the frequency response of an NND to 8.0 V peak-to-peak, 9.25 Hz sinusoidal inputs. The inputs were chosen to compare with the performance of FDs. Generation of second-order harmonics is observed using both the NND and FD (Figure 6-12(a) and Figure 5-8), but third-order harmonics are only observed in the NND (Figure 6-12(a)). The relative amplitude of higher harmonic generation in neural networks increases with the number of switching junctions [194, 305]. Here, the NND exhibits an order of magnitude higher second harmonic at a bias of 8.0 V when compared with the FD (Figure 6-12(a)

and Figure 5-8). It has been suggested that NNDs such as these could be exploited in circuits requiring passive generation of higher-order harmonics. Theoretical modelling has shown that interconnected memristor circuits could achieve more than 40% power conversion rates for second-order harmonics, compared with 4.5% for optimal diode bridges [274]. The NNDs shown here generate second-order harmonics with voltage amplitudes up to 18% of the fundamental with no optimisation performed.

The relative amplitude of the second-order harmonics rises steeply in the NND as the applied voltage approaches the threshold voltage. In recurrent neural networks, asynchronous feedback inhibition [306, 307] arises due to delayed, opposing signals that occur across the same network junction, leading to voltage cancellation and associated damping of signals. Figure 6-12(a) and Figure 5-8 show that while the harmonics in the NND are of higher amplitude than those produced by the FD, they are noticeably damped as a result of the recurrent dynamics inherent to the NND. In a fully recurrent network, complete signal cancellation occurs and therefore no harmonics are generated. Since higher order harmonics are observed in the NND, 'feedforward' pathways must be present and these must transmit the majority of the device current [194, 308].
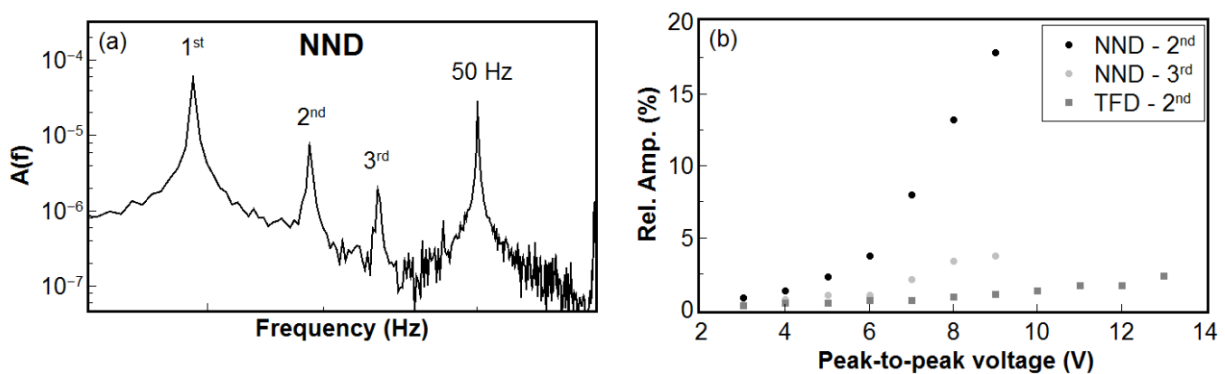
Figure 6-12: (a) Amplitude spectra obtained after Fourier transformation of responses from the NND and FD to 8V, 9.25 Hz sinusoidal input signals. (b) Relative amplitudes of harmonics generated in the NND and FD as a function of bias voltage.

6.3.3 Four-contact memristive nanoparticle network devices

From a technological point of view, the most interesting features of random network devices are their network-specific characteristics [194]. The network structure and connectivity greatly influence the device functions and have proved capable of supporting brain-like behaviour [194, 309]. Hence, random networks of nanoparticles or nanowires may enable facile fabrication of brain-like computing architectures [283]. In the following sections, multi-contact devices were used to investigate network-specific properties of self-assembled nanoparticle networks within tin oxide thin films.

Metal oxide nanoparticle networks were realised between four preformed planar Pt contacts using the high voltage electroforming process described above in section Electroforming process in memristive

nanoparticle network tin oxide devices6.3.2.1. This was done sequentially, beginning with the top and bottom contacts and then the right and left contacts. Afterwards, the nanoparticle networks were electrically connected to all four planar electrodes (Figure 6-13). Once again, the facile electroforming process resulted in a memristive nanoparticle network within a semi-insulating SnO_x film located only between the electrical contacts.
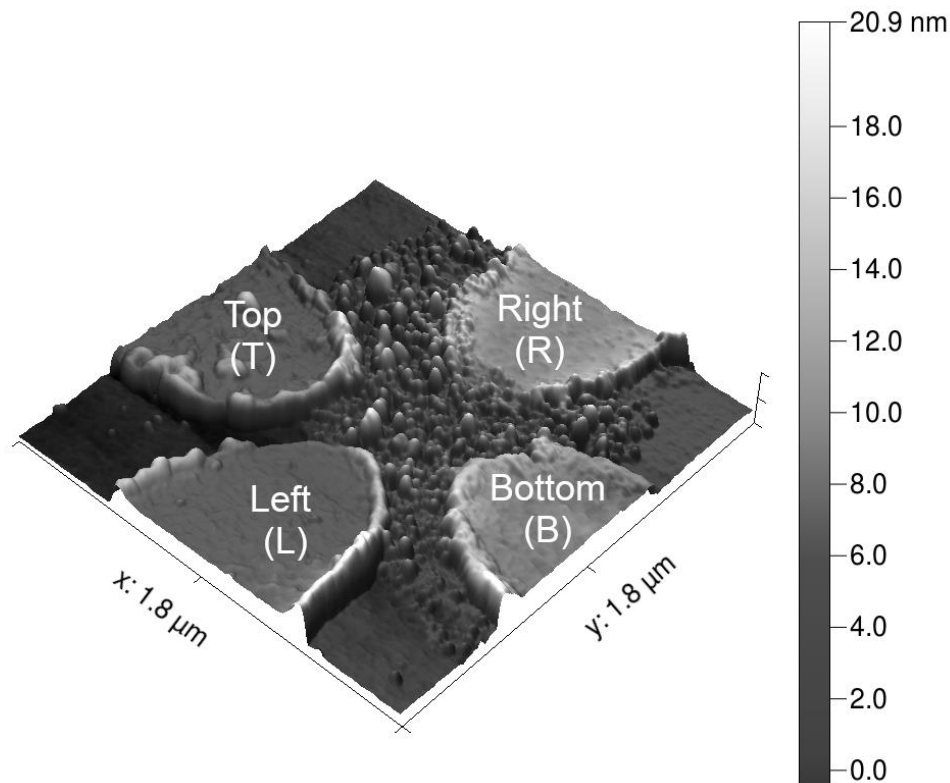
Figure 6-13: Atomic force micrograph of a self-assembled nanoparticle network formed between four planar electrodes.

6.3.3.1 Electrode resistance cross-correlation in multi-contact tin oxide nanoparticle network devices

Identification of the relationships between contact pair combinations plays an important role in the study of interactions within the network. The simplest technique is cross-correlation which can detect possible connections between a pair of electrodes. Figure 6-14 demonstrates the correlation between two pairs of electrodes of a four-contact NND: channel 1 (Ch1 = top and bottom) and channel 2 (Ch2 = right and left), when a double linear sweep with an amplitude of 4 V and duration of ~26 s was applied on one pair of the electrodes (top and bottom electrodes in (a) and (b) or right and left electrodes in (c) and (d)) while a constant non-perturbative voltage of 100 mV was maintained at the other pair. Positive bias across the top and bottom electrodes enabled resistive switching between these two electrodes but

did not significantly influence conduction between the other two electrodes, and vice versa. This indicated that there was no common path for these electrode pairs. However, when negative bias was applied to one pair, weaker but similar switching behaviours were observed both in that pair and the remaining pair, implying the existence of common path(s). The characteristics in (b) of Figure 6-14 could have been produced by current flowing through the electrodes in the order of bottom – right – left – top. However, the mechanisms could be more complicated and influenced by many factors, such as differing tunnel gaps between particles in the network, particle density and differing Joule heating effects across the network. In general, the conduction paths, existing when sufficient positive and negative biases were applied, were different, implying that different combinations of memristive junctions were activated under different stimuli. This is consistent with the asymmetric resistive switching behaviour observed in Figure 6-14. Furthermore, the network shows a high stability with the same results obtained when the test was repeated multiple times Figure A-1 (Appendix A). More correlation plots between combinations of two electrodes are presented in Table A-1 (Appendix A).
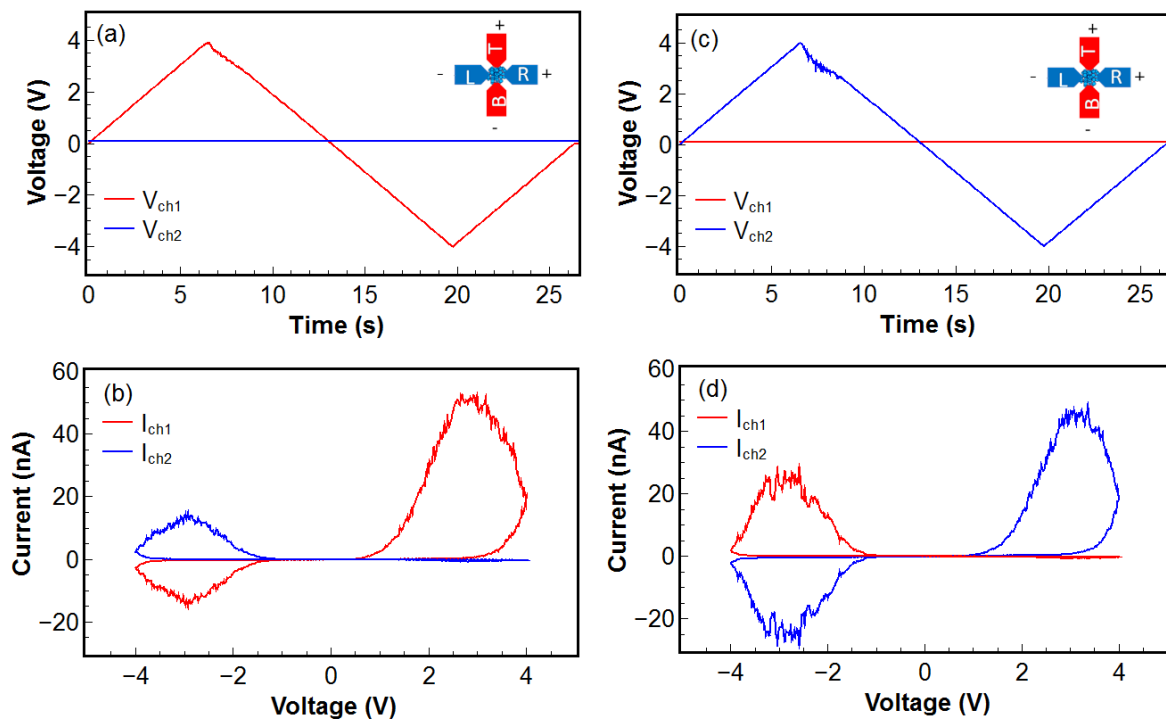
Figure 6-14: (a) and (c) Voltages applied on two pairs of electrodes, channel 1 (ch1) denotes for top and bottom, channel 2 (ch2) denotes for right and left. (b) and (d) Currents passing through two channels. Diagrams (insets) are colour-coded to show the input/output contact pairs. (+) denotes V_{Input}

The cross-correlations of all combinations of contact pairs were calculated from the measured resistances between the contact pairs under the application of a sequence of 10 pulses with pulse

amplitude of 3 V (above threshold) and pulse width of 500 ms. The values varied from 0 (no correlation) to 1 (strong correlation) and are presented in Table A-2 (Appendix A).

6.3.3.2 *Spiking-timing dependent plasticity (STDP)*

In artificial synaptic devices made of memristors, the bottom and top electrodes respectively work as the pre- and post-synaptic neurons in a biological synapse [189]. In this work, pre- and post-spikes were applied on two electrodes of a four-contact NND (e.g. left and top respectively) to demonstrate the STDP property of the device while these other two electrodes were connected to ground. Figure 6-15 illustrates the current response of channel 1 (Ch1= left and right) and channel 2 (Ch2 = top and bottom) to spikes as a function of the relative timing between the pre- and post-spikes ($\Delta t = t_{post} - t_{pre}$). The fitting curve of channel 1 (Figure 6-15(a)) resembles the asymmetric Hebbian rule described in [189]. This means that if the post-spike arrives after the pre-spike ($\Delta t < 0$), the conductivity of channel 1 (Ch1= left and right) increases, indicating long-term potential (LTP). In contrast, long term depression (LTD) represented by the decrease of the channel conductivity occurs if the post-spike is repeated before the pre-spike ($\Delta t < 0$). Current response of channel 2 (Ch2 = top and bottom) resembles the symmetric Hebbian rule [189] that show the occurrence of LTD despite of the relative time between two spikes. In short, two channels Ch1 and Ch2 exhibited different STDP behaviours, confirming the activation of different memristive junctions under stimuli.
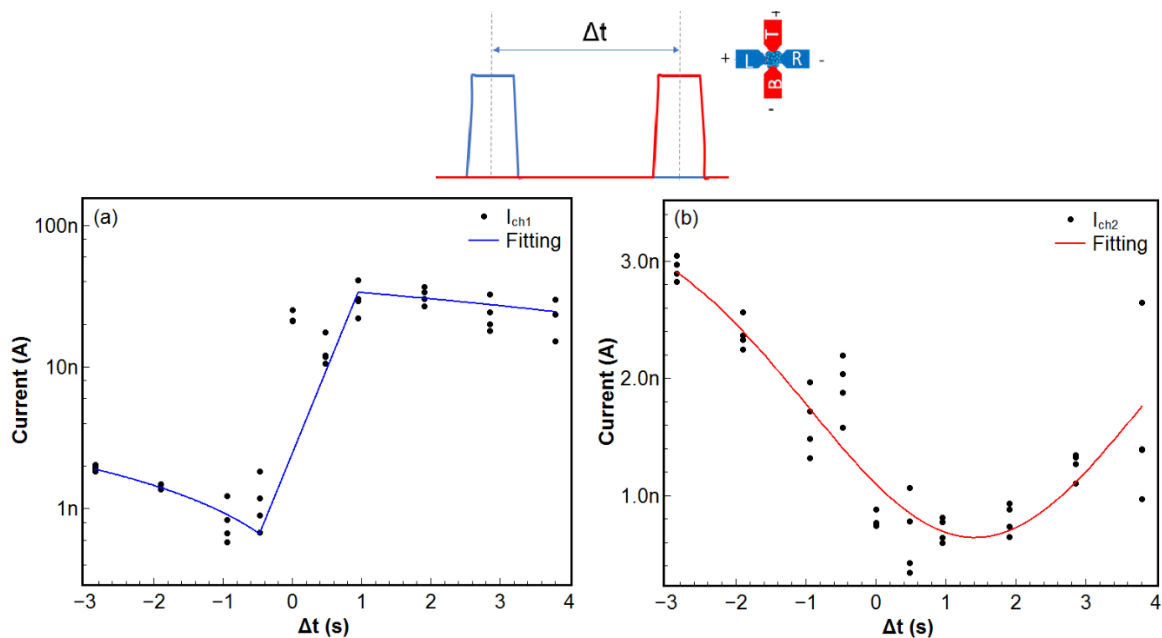
Figure 6-15: Spiking-time dependent plasticity (STDP) on two channels of a four-contact NND when the pre-spike was applied on the channel 1 (the right and left electrodes) and the post-spike was applied on the channel 2 (the top and bottom electrodes)

6.3.3.3 *Temporal coincidence detection using a multi-input multi-output network*

The multi-input multi-output reservoir computer is shown schematically in Figure 6-16. Input voltage pulses are supplied to each of the contacts in the input layer (with the output layer contacts grounded). The output state of the reservoir is measured by the current at the output layer. The input/output connections to the contacts on the nanoparticle device are labelled on the AFM image (shown in Figure 6-16(b)). The detection of coincident voltage inputs is enabled by the short-term memory dynamics of the nanoparticle reservoir. Figure 6-16(c) shows the output currents (I_{Output} *1*, I_{Output} *2*, denoted in Figure 6-16(b)), resulting from a voltage pulse train (4V, 200ms duration, 200ms inter-pulse intervals) applied to V_{input} *2* (denoted in Figure 6-16(b)). Using V_{input} *2* as a reference channel, a series of coincident 2V pulses were applied intermittently to V_{input} *1*. A 0.1 V non-perturbative read voltage was used to record the output current during non-correlated (non-coincident) events on I_{Output} *1*. Paired-pulse facilitation (PPF) was observed during both temporally correlated and non-correlated pulses applied across channel 1 (Ch1 with V_{Input}, I_{Ouput} = L, R); however, the conductance was significantly reduced in both output channels during correlated pulses. This suggests that the decreased conductance is due to voltage cancellation across inter-nanoparticle junctions rather than an active physical 'switching off' mechanism, such as ionic drift [310] or charge de-trapping [311] observed in other memristive devices. It is likely that current flow between contact pairs is also affected by capacitive crosstalk and local shunting along recurrent conduction pathways. During non-coincident pulses, the current flowed across Ch1 (V_{Input}, I_{Ouput} = L, R) in the direction counter to the 0.1V read voltage. This effect was studied in more detail using a series of 5×5 V pulses applied across Ch2 (V_{Input}, I_{Ouput} = B, T) (with 0.1 V across Ch1 (V_{Input}, I_{Ouput} = L, R)), followed immediately by 5×5 V pulses applied across Ch2 (V_{Input}, I_{Ouput} = B, T) with five coincident pulses applied across Ch1 with varying pulse heights (Figure A-2). PPF is observed across both contact pairs during the first five pulses, however, a negative current is induced across Ch1. During the following coincident pulses the current across Ch1 transitions from negative to positive as the pulse height is increased and with successive pulses (Figure A-2(b)). The current suppression occurs across Ch2 as a function of Ch1 pulse height (Figure A-2(c)).
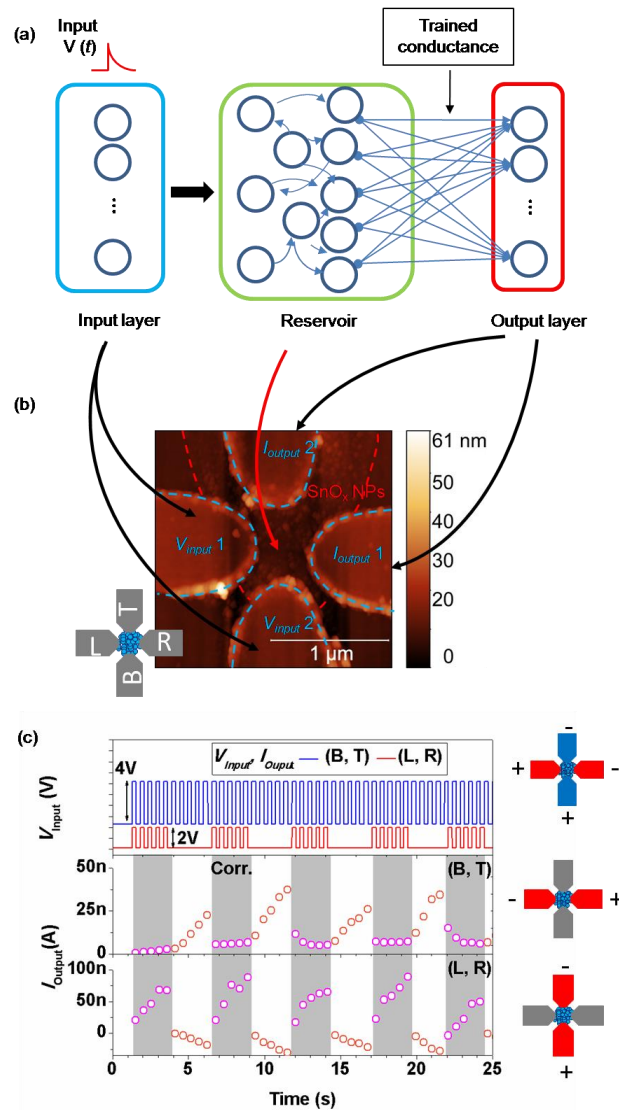
Figure 6-16: Implementation of multi-input/multi-output functions using four-terminal nanoparticle reservoirs. (a) Schematic representation of the reservoir computer. (b) AFM image of the four-terminal system with labels and diagram showing the contact setup. (c) Response of the four-terminal nanoparticle reservoir to correlated/non-correlated voltage input trains.

6.3.3.4 Investigation of Boolean logic functions in the NNDs

It was previously shown by Bose *et al.* that atomic switching networks can be reconfigured into any of the two-terminal Boolean logic operators by using multiple static gate electrodes and tuning the operating voltages [282]. Here, the nanoparticle networks display threshold switching behaviour that prevents logic operators where $p = q = 0$ from returning a *true* output (i.e. the network always begins a process in the 'off' state). However, the remaining three most commonly used Boolean logic operations were demonstrated in the NNDs by selecting the appropriate V_{Input}, I_{Ouput} electrodes and voltages. Figure 6-17 shows XOR, OR and AND operations realised using one NND. Voltage pulse trains (5 pulses, 500 ms duration, 500 ms intervals) were applied across the indicated electrode pairs. The XOR and OR

gates were configured by reversing the polarity of one of the electrode pairs. The AND gate was implemented by reducing the individual V_{Input} values to below the threshold voltage such that the voltage from one electrode pair was insufficient to change the internal state of the reservoir. PPF was still evident in each logical *true* case, indicating that the Boolean functions of the device were partially dependent on recently received inputs to the device. This is a point of distinction from previous demonstrations of logic functionality using random nanoparticle switching networks which violate the *echo state* (short-term memory) property requirement for reservoir computers.
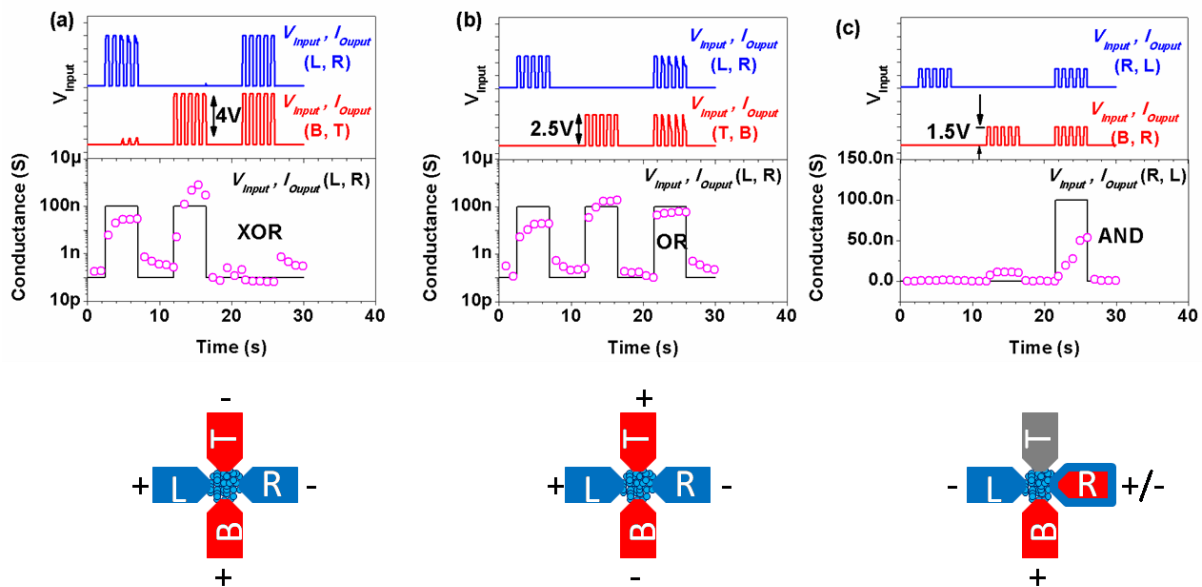
Figure 6-17: Implementation of Boolean logic gates. Time varying input voltages (top panels) and conductance values (bottom panels for (a) XOR, (b) OR and (c) AND logic gates. The electrode configurations for each gate are shown schematically below.

This combination of the *echo state* property and XOR gates can be used to demonstrate the linear separability and classification of input signals based on coincidence. Figure 6-18(a) shows a schematic representation of the experiment. The appropriate electrodes were selected to implement an XOR function. The search for conicident inputs was performed using Ch2 (V_{Input}, I_{Ouput} = B, T) as a reference input (input state [1 1 1 1 1]) and altering the input sequence on Ch1 (V_{Input}, I_{Ouput} = L, R). The output currents across both channels after 5 pulses were monitored and are displayed in Figure 6-18(b). The input states were arranged (1-9) based on the number of coincident input pulse pairs occurring at the end of the sequence. The output current depended strongly on both the number of coincident voltage pulses and the time at which the coincidence occurred. Each of the input states was classifiable due to the linear separability of the resultant output currents.

One example application for this behaviour is spatial correlation image processing. Figure 6-18(c) shows the experimental design for creating negative correlation images using the nanoparticle network in the XOR gate configuration. Binary inputs (black pixels $= 0$, white pixels $= 1$) are entered sequentially by row number into Ch1(L, R). Ch2(B, T) serves as the reference image (5 rows x [1 1 1 1]). The negative correlation image is encoded as the 'Result'. Figure 6-18(d) shows the evolution of the conductance during this process. The conductance rises according to the negatively correlated pixels (i.e. the 'Result' image) and the conductance state for each row is unique, which allows the image to be successfully recognised.
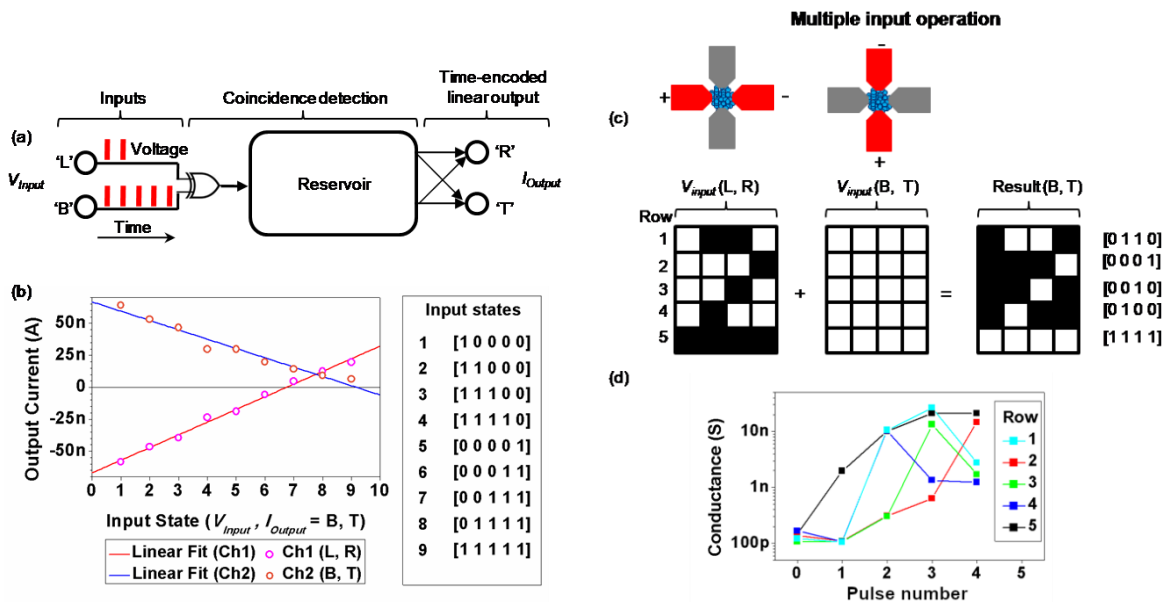
Figure 6-18: Time-encoded data classification. (a) Schematic illustration of the experimental setup used for classifying 5-digit input strings. (b) Output currents corresponding to each of the Ch1 input states. The output values are linearly separable. (c) Digit-recognition task implemented using an XOR gate to identify negative correlations in two input images. The electrode configurations used for each image are shown schematically above. (d) Conductance states of the nanoparticle network in response to the encoding of the input images in c.

6.4 Summary

In summary, a facile method for fabrication of memristive nanoparticle networks in sub-stoichiometric (mixed phase) tin oxide has been described. Stable, volatile, bidirectional resistive switching was observed in ambient and at room-temperature immediately after the formation of the nanoparticle networks. Higher-order harmonic generation and damping observed in the network devices are consistent with recurrent network behaviour rather than filamentary memristance. These characteristics suggest potential for similar devices to be exploited in applications requiring efficient passive harmonic generation.

Chapter 6: Resistive switching nanoparticle networks self-assembled in mixed phase tin oxide

The nanoparticle networks exhibit internal, short-term memory effects governed by Joule heating-induced resistance switching that satisfy the required behaviours for reservoir computing. A computing system based on emergent nanoparticle reservoirs using a top-down electro-forming process on multi-contact devices was also demonstrated. By selecting appropriate input and output electrodes and voltages, the system can perform Boolean logic gates, including XOR, OR and AND gates or implement spatial correlation image processing.

Chapter 7:

Conclusions and future work

The research work carried out in this dissertation aimed to explore characteristics and applications of energetically deposited tin oxide thin films. This chapter provides a brief summary of the significant outcomes of the research work and outlines the scope of future work related to the field.

7.1   Conclusions

Energetically deposited tin oxide thin films have been structurally, optically and electronically characterised. These films have also been incorporated in metal/oxide/metal devices to explore their resistive switching and biomimetic characteristics.

HiPIMS tin oxide deposited at room temperature with a 1:1 Ar:O_2 process pressure of 6.0 mTorr was found to exist as mixed phase nanocrystalline SnO and SnO_2, in which SnO_2 was the dominant phase. The off-axis deposition process provided a small but quantifiable variation in film composition (Sn:O), ranging from 1:1.7 to 1:1.9 from the Sn-rich to Sn-poor sides of the wafer. A wide optical bandgap of ~3.5 - 3.6 eV and high refraction index of 2.1 (at 550 nm) were estimated based on spectroscopic ellipsometry measurements. High resistivity was obtained in the as-deposited HiPIMS SnO_x but decreased with increased post-deposition annealing temperature. After annealing in the range 250°C - 350°C, samples exhibited weak p-type conductivity. However, as the annealing temperature was higher than 350°C, n-type characteristics prevailed. This is attributed to the disproportionation reaction of SnO into Sn and SnO_2 at high temperature. HiPIMS can be used to grow films in microstructural forms at low temperature by trading energy for growth temperature. However, with a narrow deposition window of SnO, SnO films were not observed after HiPIMS deposition at room temperature.

Filamentary memristors were fabricated on the mixed-phase (semi-insulating) tin oxide thin films prepared by HiPIMS. These memristors exhibited stable volatile bidirectional resistive switching with a ratio between high resistance and low resistance of more than two orders of magnitude. Evidence of a filamentary path bridging the electrodes of a memristor was provided after operation with elevated current limit enable imaging of the filamentary path by AFM. The resistive switching mechanism of these filamentary memristors is believed to relay on a minority phase change originating from Joule heating induced decomposition of SnO and oxygen diffusion. CC-NDR, second-order harmonic generation and gradual conductance modulation were observed in filamentary tin oxide memristors, suggesting suitability for various applications including selectors, memristive oscillators, harmonic generators, and signal processing. Pulse sequence recognition and spectrum analysis applications were demonstrated as example device capabilities.

Random switching networks of nanoparticles were formed within thin films of mixed phase tin oxide prepared by HiPIMS. The formation of these nanoparticle networks during electroforming was found to be sensitive to the stoichiometry of the as-deposited tin oxide film. The networks only formed in films that were oxygen rich relative to the films in which memristance was facilitated by the formation of filaments. The evolution in particle size and network size was observed after successive I-V sweeps using atomic force microscopy and image analysis. The morphological changes were attributed to partial melting by Joule heating. The nanoparticles were identified as Sn-rich nanoparticles by using advanced material characterisation tools including AES, EDS and EELS. Self-assembled nanoparticle

network memristors showed bidirectional volatile threshold-switching with more than two orders of magnitude separating the high- and low- resistance states. The switching from the HRS to the LRS likely involves enhanced conduction at the 'necks' between the nanoparticles. This could occur by multiple thermal/field induced mechanisms including reduction of the average tunnel barrier width and/or decomposition of SnO due to Joule heating to provide higher average carrier concentration within the network. The nanoparticle network devices exhibited CC-NDR, characteristics of recurrent neural networks, second and higher-order harmonic generation, and activity-dependent conductance, suggesting potential for these devices to be exploited in applications requiring efficient passive harmonic generation and in reservoir computing. Implementation of the devices for temporal coincidence detection using a multi-input multi-output network, Boolean logic functions and data processing were demonstrated.

Chapters 5 and 6 showed that filamentary and nanoparticle network memristors could be fabricated in similar films of mixed phase tin oxide deposited using HiPIMS. However, the as-deposited films possessed slightly differing stoichiometries and the characteristics of the filamentary and network devices differed significantly.

- The differences in device morphology and behaviour resulted directly from their different stoichiometries. Resistive switching behaviour caused by a filamentary conduction path was observed in the Sn-rich samples with a wide range of stoichiometry 1(Sn):1.7(O) - 1(Sn):1.84(O), while nanoparticle networks were formed within only SnO_x films in which $1.84 < x < 1.86$. This suggests that other behaviours may be observed in tin oxide films with a broader range of Sn:O ratios.

- Filamentary memristors exhibited electroforming-free switching while an electroforming step was necessary for nanoparticle network devices (NNDs) to form and invoke the evolution of the nanoparticle networks. No morphological transformations were observed in the filamentary devices (FDs), except when higher current was intentionally allowed through the device. A feature resembling a filamentary path was then observed between the device's electrodes. In NNDs, a densely packed but porous network of nanoparticles was observed in the region between the electrodes.

- Bidirectional resistive switching characteristics from the FDs resemble those of the NNDs but observable differences provide some insight into the underlying mechanisms of both the FDs and NNDs. A filament existing in LRS of FDs consisted of highly (Sn) doped SnO_2, originating from decomposition of SnO at high temperature while a combination of increased tunnelling current, narrowing tunnel gap and SnO decomposition are probable candidates for the switching mechanism of the NNDs. This assertion is also supported by the smaller threshold voltages,

greater increase in LRS current and higher sensitivity to UV of an NND relative to the FD which has similar gap between the electrodes.

- Generation of second-order harmonics was observed using both the NNDs and FDs, but third-order harmonics were only observed in the NNDs. Only the NND exhibited the characteristics of recurrent neural networks.

- In summary, while the FDs exhibit short-term memory and classification properties suitable for individual cells in reservoir computing circuits, only the NND provides the inter-connectivity required for reservoir computing. Hence, there is great potential to explore reservoir computing functions using these simple-to-fabricate NNDs.

7.2 Future work

The research work carried out in this thesis has provided significant insights into the fabrication and characterization of tin oxide deposited by HiPIMS as well as those of filamentary and nanoparticle network memristors formed within these tin oxide films. There are several aspects remaining for further investigation.

7.2.1 P-type tin oxide deposition using HiPIMS at high temperature

After deposition using HiPIMS at room temperature, the film existed as a mixed phase of SnO and SnO$_2$. Furthermore, some films exhibited p-type conductivity after annealing in vacuum at $250 - 350$°C. This indicates the possibility of fabricating p-type SnO by using HiPIMS at higher temperature. It is expected that moderately elevated deposition temperature could lead to the formation of films with higher crystallinity, lower resistivity and higher mobility.

7.2.2 FDs and NNDs with SU-8 capsulation

Both FDs and NNDs exhibited bidirectional threshold switching behaviour in ambient conditions. Many environmental factors such as presence of oxygen, moisture, etc. are likely to affect the switching characteristics of these devices, especially oxygen diffusion when switching from LRS to HRS. In the work, the devices were encapsulated using poly methyl methacrylate (PMMA) to isolate them from the air. However, PMMA has been known as a thermally unstable material and PMMA depolymerization is commonly observed at ~300 °C. Hence, in the device LRS, Joule heating may lead to damage and/or porosity in the PMMA layer. This may explain why no significant difference was observed in the switching characteristics of the devices before and after encapsulation. SU-8 is a more thermally stable capping layer that could be spin-coated or drop cast for device encapsulation. With SU-8 encapsulation, deeper insights into the switching mechanisms could be revealed.

7.2.3 Gas sensitivity of FDs and NNDs

Tin oxide has been investigated extensively as a gas sensor material. The number of studies found on gas sensors using SnO_2 was about 37.4% out of more than 8000 papers on oxide semiconductor – based gas sensors (up to July 2013 [44]). SnO_2 has been applied to detect various gases, including hydrogen [45], oxygen [46], carbon monoxide [46, 47], ethanol [47, 48], etc. Figure 7-1 illustrates the behaviour of a SnO_x filamentary device in air and nitrogen environments.
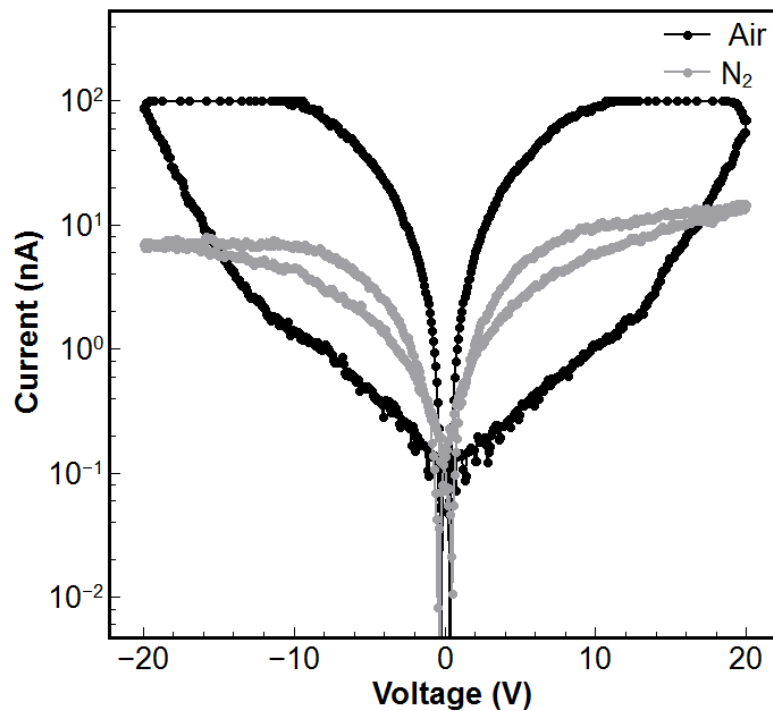
Figure 7-1: I-V characteristics for a SnO_x filamentary device in air and N_2 environment

Oxygen adsorption is a major mechanism of conduction change reported for tin oxide gas sensor studies [49, 50]. At low temperatures (T < 450 – 500 K), neutral adsorbed $O_{2\,(ads)}$ or charged adsorbed $O_{2\,(ads)}^-$ are produced on the SnO_2 surface, while neutral adsorbed $O_{(ads)}$ or charged adsorbed $O_{(ads)}^-$ or $O_{(ads)}^{2-}$) are dissociated from neutral adsorbed $O_{2\,(ads)}$ at high temperature (as shown in eq. 6-1) [51, 52].

The occurrence of oxygen adsorption processes in O-rich environment increases the upward band bending in the layer and hence, widens the depletion region [51, 53]. As a result, the electron concentration near the surface decreases, and in turn the conductivity is low. In N_2 gas, oxygen adsorption is limited, hence, both the electron concentration and the conductivity are higher compared to those in air. Thus, under the same bias, the current passing through the device when in its HRS is higher in an N_2 environment than in air, as shown in Figure 7-1.

In LRS, the increase in conductance of the device in an N_2 environment is less than one order of magnitude above that of the HRS. It is thought that adsorption of water on the SnO_x film occurs in ambient conditions. Hydroxyl attachment is proven to cause downward band-bending in the HiPIMS deposited SnO_x film (see section 4.3.2). Electron transfer is known to occur from water to SnO_x, leading to increased conductivity of the SnO_x film in moist air. However, further experiments and analysis on the behaviors of the SnO_x film with/without SU-8 encapsulation and during exposure to ultra-low humidity synthetic air need to be carried out to investigate the role of humidity in determining the device switching characteristics.

Experiments with exposure to other gases such as H_2, CO, NO, ethanol, methanol could also be executed to compare the performance of HiPIMS tin oxide memristive devices with conventional tin oxide sensors [45-49].

7.2.4 Single crystalline SnO based memristive devices

Both filamentary and nanoparticle network devices were achieved in the mixed phase tin oxide thin film deposited by HiPIMS, indicating the possibility of finding more interesting characteristics in tin oxide based memristor. Switching characteristics and mechanism of the memristors fabricated on single crystalline SnO_x samples with more precisely controlled stoichiometry (provided by a collaborator) could be investigated to further elucidate the effects of stoichiometry and crystallinity.

7.2.5 Memristive arrays for information processing

The demonstrated implementation single FDs for information processing (chapter 5) highlighted the potential for arrays of such memristors to be used to simultaneously process many inputs. This represents hardware-implementation of the "reservoir" in reservoir computing. Arrayed filamentary devices could be produced and this aspect explored. The NNDs are potentially a reservoir. For this aspect to be explored using the self-assembled networks, higher resolution electron-beam lithography and a greater number of device contacts would be required. This work could result in a very significant finding if it reveals that the devices offer a facile method for self-assembly of a suitable interconnected nanoparticle reservoir.

References

[1] D. S. Ginley and J. D. Perkins, "Transparent conductors," in *Handbook of Transparent Conductors*, D. S. Ginley, Ed. Boston, MA: Springer US, 2011, pp. 1-25.

[2] K. Nomura, H. Ohta, A. Takagi, T. Kamiya, M. Hirano, and H. Hosono, "Room-temperature fabrication of transparent flexible thin-film transistors using amorphous oxide semiconductors," *Nature,* 10.1038/nature03090 vol. 432, no. 7016, pp. 488-492, 11/25/print 2004.

[3] E. Fortunato and R. Martins, "Where science fiction meets reality? With oxide semiconductors!," *Physica Status Solidi (RRL) – Rapid Research Letters,* vol. 5, no. 9, pp. 336-339, 2011.

[4] K. Toshio, N. Kenji, and H. Hideo, "Present status of amorphous In–Ga–Zn–O thin-film transistors," *Science and Technology of Advanced Materials,* vol. 11, no. 4, p. 044305, 2010.

[5] P. Barquinha, R. Martins, L. Pereira, and E. Fortunato, "Introduction," in *Transparent Oxide Electronics*: John Wiley & Sons, Ltd, 2012, pp. 1-7.

[6] S. Corp. (2012). *Sharp begins production of world's first*1 LCD panels incorporating IGZO oxide semiconductors* [Online]. Available: http://www.sharp-world.com/corporate/news/120413.html.

[7] E. Fortunato, P. Barquinha, and R. Martins, "Oxide semiconductor thin-film transistors: A review of recent advances," *Advanced Materials,* vol. 24, no. 22, pp. 2945-2986, 2012.

[8] T. Comp. (2006). *Toppan demonstrates flexible elctronic paper driven by Oxide Semiconductor TFT-enables next generation, thin and flexible displays* [Online]. Available: http://www.toppan.co.jp/en/news/2006/03/newsrelease446.html.

[9] Z. Wang, P. K. Nayak, J. A. Caraveo-Frescas, and H. N. Alshareef, "Recent developments in p-type oxide semiconductor materials and devices," *Advanced Materials,* vol. 28, no. 20, pp. 3831-3892, 2016.

[10] J. Karlsson and A. Roos, "Annual energy window performance vs. glazing thermal emittance — the relevance of very low emittance values," *Thin Solid Films,* vol. 392, no. 2, pp. 345-348, 2001.

[11] H. L. Z. Kelvin, X. Kai, G. B. Mark, and G. E. Russell, "P -type transparent conducting oxides," *Journal of Physics: Condensed Matter,* vol. 28, no. 38, p. 383002, 2016.

[12] P. D. C. King *et al.*, "Surface band-gap narrowing in quantized electron accumulation layers," *Physical Review Letters,* vol. 104, no. 25, p. 256803, 2010.

[13] J. J. Mudd *et al.*, "Hard x-ray photoelectron spectroscopy as a probe of the intrinsic electronic properties of CdO," *Physical Review B,* vol. 89, no. 3, p. 035203, 2014.

[14] M. Batzill and U. Diebold, "The surface and materials science of tin oxide," *Progress in Surface Science,* vol. 79, no. 2, pp. 47-154, 2005.

[15] P. Barquinha, R. Martins, L. Pereira, and E. Fortunato, "N-type transparent semiconducting oxides," in *Transparent Oxide Electronics*: John Wiley & Sons, Ltd, 2012, pp. 9-61.

[16] J. R. Bellingham, W. A. Phillips, and C. J. Adkins, "Amorphous indium oxide," *Thin Solid Films,* vol. 195, no. 1, pp. 23-32, 1991.

[17] Y. Shigesato, "In based TCOs," in *Handbook of Transparent Conductors*, D. S. Ginley, Ed. Boston, MA: Springer US, 2011, pp. 149-169.

[18] M. Thirumoorthi and J. J. P. Thomas, "Structure, optical and electrical properties of indium tin oxide ultra thin films prepared by jet nebulizer spray pyrolysis technique," *Journal of Asian Ceramic Societies,* vol. 4, no. 1, pp. 124-132, 2016.

[19] Y. Shigesato, S. Takaki, and T. Haranoh, "Electrical and structural properties of low resistivity tin-doped indium oxide films," *Journal of Applied Physics,* vol. 71, no. 7, pp. 3356-3364, 1992.

[20] Y. Shigesato and D. C. Paine, "Study of the effect of Sn doping on the electronic transport properties of thin film indium oxide," *Applied Physics Letters,* vol. 62, no. 11, pp. 1268-1270, 1993.

[21]   I. Hamberg and C. G. Granqvist, "Evaporated Sn-doped In_2O_3 films: Basic optical properties and applications to energy-efficient windows," *Journal of Applied Physics,* vol. 60, no. 11, pp. R123-R160, 1986.

[22]   Y. Shigesato, I. Yasui, Y. Hayashi, S. Takaki, T. Oyama, and M. Kamei, "Effects of water partial pressure on the activated electron beam evaporation process to deposit tin-doped indium-oxide films," *Journal of Vacuum Science & Technology A: Vacuum, Surfaces, and Films,* vol. 13, no. 2, pp. 268-275, 1995.

[23]   B. G. Lewis and D. C. Paine, "Applications and processing of transparent conducting oxides," *MRS Bulletin,* vol. 25, no. 8, pp. 22-27, 2011.

[24]   J. C. Manifacier, "Thin metallic oxides as transparent conductors," *Thin Solid Films,* vol. 90, no. 3, pp. 297-308, 1982.

[25]   G. Neri, A. Bonavita, G. Micali, G. Rizzo, E. Callone, and G. Carturan, "Resistive CO gas sensors based on In_2O_3 and $InSnO_x$ nanopowders synthesized via starch-aided sol–gel process for automotive applications," *Sensors and Actuators B: Chemical,* vol. 132, no. 1, pp. 224-233, 2008.

[26]   M. G. McDowell and I. G. Hill, "Influence of channel stoichiometry on zinc indium oxide thin-film transistor performance," *IEEE Transactions on Electron Devices,* vol. 56, no. 2, pp. 343-347, 2009.

[27]   G. Bernardo *et al.*, "Polymer light-emitting diodes with amorphous indium-zinc oxide anodes deposited at room temperature," *Synthetic Metals,* vol. 159, no. 11, pp. 1112-1115, 2009.

[28]   N. Ito, Y. Sato, P. K. Song, A. Kaijio, K. Inoue, and Y. Shigesato, "Electrical and optical properties of amorphous indium zinc oxide films," *Thin Solid Films,* vol. 496, no. 1, pp. 99-103, 2006.

[29]   H. Hosono, "Ionic amorphous oxide semiconductors: Material design, carrier transport, and device application," *Journal of Non-Crystalline Solids,* vol. 352, no. 9, pp. 851-858, 2006.

[30]   Q. Xin, L. Yan, Y. Luo, and A. Song, "Study of breakdown voltage of indium-gallium-zinc-oxide-based Schottky diode," *Applied Physics Letters,* vol. 106, no. 11, p. 113506, 2015.

[31]   S.-H. K. Park *et al.*, "4.3: Transparent ZnO thin film transistor array for the application of transparent AM-OLED display," *SID Symposium Digest of Technical Papers,* vol. 37, no. 1, pp. 25-28, 2006.

[32]   M. Nakano *et al.*, "Transparent polymer Schottky contact for a high performance visible-blind ultraviolet photodiode based on ZnO," *Applied Physics Letters,* vol. 93, no. 12, p. 123309, 2008.

[33]   Y. Ryu *et al.*, "Next generation of oxide photonic devices: ZnO-based ultraviolet light emitting diodes," *Applied Physics Letters,* vol. 88, no. 24, p. 241108, 2006.

[34]   X. Wu *et al.*, "Ultraviolet photonic crystal laser," *Applied Physics Letters,* vol. 85, no. 17, pp. 3657-3659, 2004.

[35]   R. L. Hoffman, B. J. Norris, and J. F. Wager, "ZnO-based transparent thin-film transistors," *Applied Physics Letters,* vol. 82, no. 5, pp. 733-735, 2003.

[36]   E. Fortunato *et al.*, "Recent advances in ZnO transparent thin film transistors," *Thin Solid Films,* vol. 487, no. 1–2, pp. 205-211, 9/1/ 2005.

[37]   C. G. Lee and A. Dodabalapur, "Solution-processed zinc-tin oxide thin-film transistors with high performance and improved uniformity," in *Device Research Conference (DRC)*, 2010, pp. 123-124.

[38]   H. Hosono, K. Nomura, Y. Ogo, T. Uruga, and T. Kamiya, "Factors controlling electron transport properties in transparent amorphous oxide semiconductors," *Journal of Non-Crystalline Solids,* vol. 354, no. 19, pp. 2796-2800, 2008.

[39]   E. M. C. Fortunato *et al.*, "High mobility indium free amorphous oxide thin film transistors," *Applied Physics Letters,* vol. 92, no. 22, p. 222103, 2008.

[40]   T. Minami, T. Miyata, and T. Yamamoto, "Work function of transparent conducting multicomponent oxide thin films prepared by magnetron sputtering," *Surface and Coatings Technology,* vol. 108, pp. 583-587, 1998.

[41] H. Ohta, M. Orita, M. Hirano, H. Tanji, H. Kawazoe, and H. Hosono, "Highly electrically conductive indium–tin–oxide thin films epitaxially grown on yttria-stabilized zirconia (100) by pulsed-laser deposition," *Applied Physics Letters,* vol. 76, no. 19, pp. 2740-2742, 2000.

[42] R. Mamazza, D. L. Morel, and C. S. Ferekides, "Transparent conducting oxide thin films of Cd_2SnO_4 prepared by RF magnetron co-sputtering of the constituent binary oxides," *Thin Solid Films,* vol. 484, no. 1, pp. 26-33, 2005.

[43] R. Gupta, N. Mamidi, K. Ghosh, S. Mishra, and P. Kahol, "Growth and characterization of In_2O_3 thin films prepared by pulsed laser deposition," *Journal of Optoelectronics and Advanced Materials,* vol. 9, no. 7, pp. 2211-2216, 2007.

[44] P. F. Carcia, R. S. McLean, M. H. Reilly, and G. N. Jr., "Transparent ZnO thin-film transistor fabricated by rf magnetron sputtering," *Applied Physics Letters,* vol. 82, no. 7, pp. 1117-1119, 2003.

[45] S. K. V. Farahani, T. D. Veal, P. D. C. King, J. Zúñiga-Pérez, V. Muñoz-Sanjosé, and C. F. McConville, "Electron mobility in CdO films," *Journal of Applied Physics,* vol. 109, no. 7, p. 073712, 2011.

[46] V. K. Jain, P. Kumar, M. Kumar, P. Jain, D. Bhandari, and Y. K. Vijay, "Study of post annealing influence on structural, chemical and electrical properties of ZTO thin films," *Journal of Alloys and Compounds,* vol. 509, no. 8, pp. 3541-3546, 2011.

[47] D.-J. Son, Y.-D. Ko, D.-G. Jung, J.-H. Boo, S.-H. Choa, and Y.-S. Kim, "Thermal effect on characteristics of IZTO thin films deposited by pulsed DC magnetron sputtering," *Bulletin of the Korean Chemical Society,* vol. 32, no. 3, pp. 847-851, 2011.

[48] B. Macco, Y. Wu, D. Vanhemel, and W. M. M. Kessels, "High mobility In_2O_3:H transparent conductive oxides prepared by atomic layer deposition and solid phase crystallization," *Physica status solidi (RRL) – Rapid Research Letters,* vol. 8, no. 12, pp. 987-990, 2014.

[49] M. Morales-Masis, S. M. De Nicolas, J. Holovsky, S. De Wolf, and C. Ballif, "Low-temperature high-mobility amorphous IZO for silicon heterojunction solar cells," *IEEE Journal of Photovoltaics,* vol. 5, no. 5, pp. 1340-1347, 2015.

[50] C.-H. Wu, F.-C. Yang, W.-C. Chen, and C.-L. Chang, "Influence of oxygen/argon reaction gas ratio on optical and electrical characteristics of amorphous IGZO thin films coated by HiPIMS process," *Surface and Coatings Technology,* vol. 303, pp. 209-214, 2016.

[51] C. Guillén and J. Herrero, "Structural and plasmonic characteristics of sputtered SnO_2:Sb and ZnO:Al thin films as a function of their thickness," *Journal of Materials Science,* vol. 51, no. 15, pp. 7276-7285, 2016.

[52] O. S. Elsherif, G. E. A. Muftah, O. Abubaker, and I. M. Dharmadasa, "Structural, optical and electrical properties of SnO_2:F thin films deposited by spray pyrolysis for application in thin film solar cells," *Journal of Materials Science: Materials in Electronics,* vol. 27, no. 12, pp. 12280-12286, 2016.

[53] B. Xiao, Z. Ye, Y. Zhang, Y. Zeng, L. Zhu, and B. Zhao, "Fabrication of p-type Li-doped ZnO films by pulsed laser deposition," *Applied Surface Science,* vol. 253, no. 2, pp. 895-897, 2006.

[54] O. Lopatiuk-Tirpak *et al.*, "Studies of minority carrier diffusion length increase in p-type ZnO:Sb," *Journal of Applied Physics,* vol. 100, no. 8, p. 086101, 2006.

[55] H. Kawazoe, M. Yasukawa, H. Hyodo, M. Kurita, H. Yanagi, and H. Hosono, "P-type electrical conduction in transparent thin films of $CuAlO_2$," *Nature,* vol. 389, no. 6654, pp. 939-942, 1997.

[56] X. Zou, G. Fang, L. Yuan, M. Li, W. Guan, and X. Zhao, "Top-gate low-threshold voltage p-Cu_2O thin-film transistor grown on SiO_2/Si substrate using a high-k HfON gate dielectric," *IEEE Electron Device Letters,* vol. 31, no. 8, pp. 827-829, 2010.

[57] H. Yanagi, S. Inoue, K. Ueda, H. Kawazoe, H. Hosono, and N. Hamada, "Electronic structure and optoelectronic properties of transparent p-type conducting $CuAlO_2$," *Journal of Applied Physics,* vol. 88, no. 7, pp. 4159-4163, 2000.

[58] K. Ueda *et al.*, "Epitaxial growth of transparent p-type conducting $CuGaO_2$ thin films on sapphire (001) substrates by pulsed laser deposition," *Journal of Applied Physics,* vol. 89, no. 3, pp. 1790-1793, 2001.

[59] H. Yanagi, T. Hase, S. Ibuki, K. Ueda, and H. Hosono, "Bipolarity in electrical conduction of transparent oxide semiconductor $CuInO_2$ with delafossite structure," *Applied Physics Letters,* vol. 78, no. 11, pp. 1583-1585, 2001.

[60] T. Arnold *et al.*, "X-ray spectroscopic study of the electronic structure of $CuCrO_2$," *Physical Review B,* vol. 79, no. 7, p. 075102, 2009.

[61] M. K. Jayaraj, A. D. Draeseke, J. Tate, and A. W. Sleight, "P-type transparent thin films of $CuY_{1-x}Ca_xO_2$," *Thin Solid Films,* vol. 397, no. 1, pp. 244-248, 2001.

[62] N. Duan, A. W. Sleight, M. K. Jayaraj, and J. Tate, "Transparent p-type conducting $CuScO_{2+x}$ films," *Applied Physics Letters,* vol. 77, no. 9, pp. 1325-1326, 2000.

[63] A. Kudo, H. Yanagi, H. Hosono, and H. Kawazoe, "$SrCu_2O_2$: A p-type conductive oxide with wide band gap," *Applied Physics Letters,* vol. 73, no. 2, pp. 220-222, 1998.

[64] K. Ueda, S. Inoue, H. Hosono, N. Sarukura, and M. Hirano, "Room-temperature excitons in wide-gap layered-oxysulfide semiconductor: LaCuOS," *Applied Physics Letters,* vol. 78, no. 16, pp. 2333-2335, 2001.

[65] H. Hiramatsu, K. Ueda, H. Ohta, M. Hirano, T. Kamiya, and H. Hosono, "Degenerate p-type conductivity in wide-gap $LaCuOS_{1-x}Se_x$ (x=0–1) epitaxial films," *Applied Physics Letters,* vol. 82, no. 7, pp. 1048-1050, 2003.

[66] H. Hiramatsu, M. Orita, M. Hirano, K. Ueda, and H. Hosono, "Electrical conductivity control in transparent p-type (LaO)CuS thin films prepared by rf sputtering," *Journal of Applied Physics,* vol. 91, no. 11, pp. 9177-9181, 2002.

[67] H. Hiramatsu *et al.*, "Intrinsic excitonic photoluminescence and band-gap engineering of wide-gap p-type oxychalcogenide epitaxial films of LnCuOCh (Ln=La, Pr, and Nd; Ch=S or Se) semiconductor alloys," *Journal of Applied Physics,* vol. 94, no. 9, pp. 5805-5808, 2003.

[68] R. Nagarajan, A. D. Draeseke, A. W. Sleight, and J. Tate, "P-type conductivity in $CuCr_{1-x}Mg_xO_2$ films and powders," *Journal of Applied Physics,* vol. 89, no. 12, pp. 8022-8025, 2001.

[69] T. Mine, H. Yanagi, K. Nomura, T. Kamiya, M. Hirano, and H. Hosono, "Control of carrier concentration and surface flattening of $CuGaO_2$ epitaxial films for a p-channel transparent transistor," *Thin Solid Films,* vol. 516, no. 17, pp. 5790-5794, 2008.

[70] Z. Q. Yao *et al.*, "Energy band engineering and controlled p-type conductivity of $CuAlO_2$ thin films by nonisovalent Cu-O alloying," *Applied Physics Letters,* vol. 100, no. 6, p. 062102, 2012.

[71] J. Luo, Y. J. Lin, H. C. Hung, C. J. Liu, and Y. W. Yang, "Tuning the formation of p-type defects by peroxidation of $CuAlO_2$ films," *Journal of Applied Physics,* vol. 114, no. 3, p. 5, 2013.

[72] Y. Ogo *et al.*, "Tin monoxide as an s-orbital-based p-type oxide semiconductor: Electronic structures and TFT application," *Physica Status Solidi (a),* vol. 206, no. 9, pp. 2187-2191, 2009.

[73] E. Fortunato *et al.*, "Transparent p-type SnO_x thin film transistors produced by reactive rf magnetron sputtering followed by low temperature annealing," *Applied Physics Letters,* vol. 97, no. 5, p. 052105, 2010.

[74] Y. Pei, W. Liu, J. Shi, Z. Chen, and G. Wang, "Fabrication and characterization of p-type SnO thin film with high c-axis preferred orientation," *Journal of Electronic Materials,* vol. 11, no. 45, pp. 5967-5973, 2016.

[75] H. Yabuta *et al.*, "Sputtering formation of p-type SnO thin-film transistors on glass toward oxide complimentary circuits," *Applied Physics Letters,* vol. 97, no. 7, p. 072111, 2010.

[76] E. Fortunato *et al.*, "Thin-film transistors based on p-type Cu_2O thin films produced at room temperature," *Applied Physics Letters,* vol. 96, no. 19, p. 192102, 2010.

[77] V. Figueiredo *et al.*, "P-type Cu_xO films deposited at room temperature for thin-film transistors," *Journal of Display Technology,* vol. 8, no. 1, pp. 41-47, 212 2012.

[78] H. Qin, W. Liu, and B. Xiaofang, "On the dependence of hole concentration and its mobility on crystallization degree in p-type cuprous oxide film," *Journal of Physics D: Applied Physics,* vol. 46, no. 50, p. 505101, 2013.

[79] Z. Chen *et al.*, "Fabrication of p-type copper oxide thin-film transisters at different oxygen partial pressure," in *2014 12th IEEE International Conference on Solid-State and Integrated Circuit Technology (ICSICT)*, 2014, pp. 1-3.

[80] J. Yu Sup, C. Hyung Wook, and K. Kyung Hwan, "Properties of p-type N-doped Cu_2O thin films prepared by reactive sputtering," *Japanese Journal of Applied Physics,* vol. 53, no. 11S, p. 11RA10, 2014.

[81] T. Minami, Y. Nishi, and T. Miyata, "Impact of incorporating sodium into polycrystalline p-type Cu_2O for heterojunction solar cell applications," *Applied Physics Letters,* vol. 105, no. 21, p. 212104, 2014.

[82] M. Dekkers, G. Rijnders, and D. H. A. Blank, "ZnIr2O4, a p-type transparent oxide semiconductor in the class of spinel zinc-d6-transition metal oxide," *Applied Physics Letters,* vol. 90, no. 2, p. 021903, 2007.

[83] A. A. Bolzan, C. Fong, B. J. Kennedy, and C. J. Howard, "Structural studies of rutile-type metal dioxides," *Acta Crystallographica Section B: Structural Science,* vol. 53, no. 3, pp. 373-380, 1997.

[84] Y. Li *et al.*, "Optical properties of the high-pressure phases of SnO_2: first-principles calculation," *The Journal of Physical Chemistry A,* vol. 114, no. 2, pp. 1052-1059, 2009.

[85] S. Mehraj and M. S. Ansari, "Annealed SnO_2 thin films: structural, electrical and their magnetic properties," *Thin Solid Films,* vol. 589, pp. 57-65, 2015.

[86] K. Ellmer, "Transparent conductive zinc oxide and its derivatives," in *Handbook of Transparent Conductors*, D. S. Ginley, Ed. Boston, MA: Springer US, 2011, pp. 193-263.

[87] J. Robertson and B. Falabretti, "Electronic structure of transparent conducting oxides," in *Handbook of Transparent Conductors*: Springer, 2011, pp. 27-50.

[88] K. Chopra, S. Major, and D. Pandya, "Transparent conductors—a status review," *Thin Solid Films,* vol. 102, no. 1, pp. 1-46, 1983.

[89] C. Fonstad and R. Rediker, "Electrical properties of high-quality stannic oxide crystals," *Journal of Applied Physics,* vol. 42, no. 7, pp. 2911-2918, 1971.

[90] Z. Chen *et al.*, "Recent advances in tin dioxide materials: some developments in thin films, nanowires, and nanorods," *Chemical Reviews,* vol. 114, no. 15, pp. 7442-7486, 2014.

[91] S. Das and V. Jayaraman, "SnO_2: A comprehensive review on structures and gas sensors," *Progress in Materials Science,* vol. 66, pp. 112-255, 2014.

[92] H. Kim and A. Pique, "Transparent conducting Sb-doped SnO_2 thin films grown by pulsed-laser deposition," *Applied Physics Letters,* vol. 84, no. 2, pp. 218-220, 2004.

[93] H. S. Randhawa, M. D. Matthews, and R. F. Bunshah, "SnO_2 films prepared by activated reactive evaporation," *Thin Solid Films,* vol. 83, no. 2, pp. 267-271, 1981.

[94] R. G. Gordon, "Criteria for choosing transparent conductors," *MRS Bulletin,* vol. 25, no. 8, pp. 52-57, 2000.

[95] R. Presley, C. Munsee, C. Park, D. Hong, J. Wager, and D. Keszler, "Tin oxide transparent thin-film transistors," *Journal of Physics D: Applied Physics,* vol. 37, no. 20, p. 2810, 2004.

[96] G. Huang, L. Duan, G. Dong, D. Zhang, and Y. Qiu, "High-mobility solution-processed tin oxide thin-film transistors with high-κ alumina dielectric working in enhancement mode," *ACS Applied Materials and Interfaces,* vol. 6, no. 23, pp. 20786-20794, 2014.

[97] J. Cheng, J. Wang, Q. Li, H. Liu, and Y. Li, "A review of recent developments in tin dioxide composites for gas sensing application," *Journal of Industrial and Engineering Chemistry,* vol. 44, pp. 1-22, 2016.

[98] R. Ab Kadir *et al.*, "Electrospun granular hollow SnO_2 nanofibers hydrogen gas sensors operating at low temperatures," *The Journal of Physical Chemistry C,* vol. 118, no. 6, pp. 3129-3139, 2014.

[99]   A. Kolmakov, Y. Zhang, G. Cheng, and M. Moskovits, "Detection of CO and O_2 using tin oxide nanowire sensors," *Advanced Materials,* vol. 15, no. 12, pp. 997-1000, 2003.

[100]   A. Sharma, M. Tomar, and V. Gupta, "Enhanced response characteristics of SnO_2 thin film based NO_2 gas sensor integrated with nanoscaled metal oxide clusters," *Sensors and Actuators B: Chemical,* vol. 181, pp. 735-742, 2013.

[101]   E. Comini, G. Faglia, and G. Sberveglieri, "UV light activation of tin oxide thin films for NO_2 sensing at low temperatures," *Sensors and Actuators B: Chemical,* vol. 78, no. 1-3, pp. 73-77, 2001.

[102]   E. Comini, G. Faglia, G. Sberveglieri, Z. Pan, and Z. L. Wang, "Stable and highly sensitive gas sensors based on semiconducting oxide nanobelts," *Applied Physics Letters,* vol. 81, no. 10, pp. 1869-1871, 2002.

[103]   H. R. Kim, K. I. Choi, K. M. Kim, I. D. Kim, G. Cao, and J. H. Lee, "Ultra-fast responding and recovering C_2H_5OH sensors using SnO_2 hollow spheres prepared and activated by Ni templates," *Chemical Communications,* vol. 46, no. 28, pp. 5061-5063, 2010.

[104]   P. Li, H. Fan, and Y. Cai, "In_2O_3/SnO_2 heterojunction microstructures: Facile room temperature solid-state synthesis and enhanced Cl_2 sensing performance," *Sensors and Actuators B: Chemical,* vol. 185, pp. 110-116, 2013.

[105]   S. S. Kim, H. G. Na, S.-W. Choi, D. S. Kwak, and H. W. Kim, "Novel growth of CuO-functionalized, branched SnO_2 nanowires and their application to H_2S sensors," *Journal of Physics D: Applied Physics,* vol. 45, no. 20, p. 205301, 2012.

[106]   N. F. Quackenbush *et al.*, "Origin of the bipolar doping behavior of SnO from x-ray spectroscopy and density functional theory," *Chemistry of Materials,* vol. 25, no. 15, pp. 3114-3123, 2013.

[107]   A. Togo, F. Oba, I. Tanaka, and K. Tatsumi, "First-principles calculations of native defects in tin monoxide," *Physical Review B,* vol. 74, no. 19, p. 195128, 2006.

[108]   J. P. Allen, D. O. Scanlon, L. F. J. Piper, and G. W. Watson, "Understanding the defect chemistry of tin monoxide," *Journal of Materials Chemistry C,* vol. 1, no. 48, pp. 8194-8208, 2013.

[109]   J. B. Varley, A. Schleife, A. Janotti, and C. G. Van de Walle, "Ambipolar doping in SnO," *Applied Physics Letters,* vol. 103, no. 8, p. 082118, 2013.

[110]   A. M.-J. Matti and T. R. Tapio, "Possible structures of nonstoichiometric tin oxide: the composition Sn_2O_3," *Modelling and Simulation in Materials Science and Engineering,* vol. 12, no. 1, p. 33, 2004.

[111]   Y. Ogo *et al.*, "P-channel thin-film transistor using p-type oxide semiconductor, SnO," *Applied Physics Letters,* vol. 93, no. 3, p. 032113, 2008.

[112]   P. C. Hsu, C. C. Wu, H. Hiramatsu, T. Kamiya, and H. Hosono, "Film texture, hole transport and field-effect mobility in polycrystalline SnO thin films on glass," *ECS Journal of Solid State Science and Technology,* vol. 3, no. 9, pp. Q3040-Q3044, 2014.

[113]   D. B. Granato, J. A. Caraveo-Frescas, H. N. Alshareef, and U. Schwingenschlögl, "Enhancement of p-type mobility in tin monoxide by native defects," *Applied Physics Letters,* vol. 102, no. 21, p. 212105, 2013.

[114]   J. A. Caraveo-Frescas, P. K. Nayak, H. A. Al-Jawhari, D. B. Granato, U. Schwingenschlögl, and H. N. Alshareef, "Record mobility in transparent p-type tin monoxide films and devices by phase engineering," *ACS Nano,* vol. 7, no. 6, pp. 5160-5167, 2013.

[115]   K. J. Saji, Y. V. Subbaiah, K. Tian, and A. Tiwari, "P-type SnO thin films and SnO/ZnO heterostructures for all-oxide electronic and optoelectronic device applications," *Thin Solid Films,* vol. 605, pp. 193-201, 2016.

[116]   J. Pannetier and G. Denes, "Tin (II) oxide: structure refinement and thermal expansion," *Acta Crystallographica Section B: Structural Crystallography and Crystal Chemistry,* vol. 36, no. 11, pp. 2763-2765, 1980.

[117]   F. Izumi, "Pattern-fitting structure refinement of tin(II) oxide," *Journal of Solid State Chemistry,* vol. 38, no. 3, pp. 381-385, 1981.

[118] M. S. Moreno and R. C. Mercader, "Mossbauer study of SnO lattice dynamics," *Physical Review B,* vol. 50, no. 14, pp. 9875-9881, 1994.

[119] E. P. y Blancá, A. Svane, N. Christensen, C. Rodriguez, O. Cappannini, and M. Moreno, "Calculated static and dynamic properties of β-Sn and Sn-O compounds," *Physical Review B,* vol. 48, no. 21, p. 15712, 1993.

[120] Y. Duan, "Electronic properties and stabilities of bulk and low-index surfaces of SnO in comparison with SnO_2: A first-principles density functional approach with an empirical correction of van der Waals interactions," *Physical Review B,* vol. 77, no. 4, p. 045332, 2008.

[121] Q.-J. Liu, Z.-T. Liu, and L.-P. Feng, "First-principles calculations of structural, electronic and optical properties of tetragonal SnO_2 and SnO," *Computational Materials Science,* vol. 47, no. 4, pp. 1016-1022, 2010.

[122] J. P. Allen, D. O. Scanlon, S. C. Parker, and G. W. Watson, "Tin monoxide: structural prediction from first principles calculations with Van der Waals corrections," *The Journal of Physical Chemistry C,* vol. 115, no. 40, pp. 19916-19924, 2011.

[123] C. Kim, S. Kim, and S. E. Kim, "Transparent SnO_x thin films fabricated by radio frequency reactive sputtering with a SnO/Sn composite target," *Thin Solid Films,* vol. 634, pp. 175-180, 2017.

[124] K. Nomura, T. Kamiya, and H. Hosono, "Ambipolar oxide thin-film transistor," *Advanced Materials,* vol. 23, no. 30, pp. 3431-3434, 2011.

[125] X. Li *et al.*, "Determination of some basic physical parameters of SnO based on SnO/Si pn heterojunctions," *Applied Physics Letters,* vol. 106, no. 13, p. 132102, 2015.

[126] Z. Wang, P. K. Nayak, A. Albar, N. Wei, U. Schwingenschlögl, and H. N. Alshareef, "Transparent $SnO–SnO_2$ p–n junction diodes for electronic and sensing applications," *Advanced Materials Interfaces,* vol. 2, no. 18, pp. 1500374, 2015.

[127] T. Yang *et al.*, "Preparation and characterization of p-type transparent conducting SnO thin films," *Materials Letters,* vol. 139, pp. 39-41, 2015.

[128] P. K. Nayak, J. A. Caraveo-Frescas, Z. Wang, M. N. Hedhili, Q. X. Wang, and H. N. Alshareef, "Thin film Complementary Metal Oxide Semiconductor (CMOS) device using a single-step deposition of the channel layer," *Scientific Report*, p. 4672, 2014.

[129] I. C. Chiu, Y. S. Li, M. S. Tu, and I. C. Cheng, "Complementary oxide semiconductor-based circuits with n-channel ZnO and p-channel SnO thin-film transistors," *IEEE Electron Device Letters,* vol. 35, no. 12, pp. 1263-1265, 2014.

[130] L. Ho-Nyeon, K. Hyung-Jung, and K. Chang-Kyo, "P-channel tin monoxide thin film transistor fabricated by vacuum thermal evaporation," *Japanese Journal of Applied Physics,* vol. 49, no. 2R, p. 020202, 2010.

[131] L. Y. Liang, Z. M. Liu, H. T. Cao, and X. Q. Pan, "Microstructural, optical, and electrical properties of SnO thin films prepared on quartz via a two-step method," *ACS Applied Materials & Interfaces,* vol. 2, no. 4, pp. 1060-1065, 2010.

[132] L. Ling Yan *et al.*, "The structural, optical and electrical properties of Y-doped SnO thin films and their p-type TFT application," *Journal of Physics D: Applied Physics,* vol. 45, no. 8, p. 085101, 2012.

[133] H. Po-Ching *et al.*, "Fabrication of p-type SnO thin-film transistors by sputtering with practical metal electrodes," *Japanese Journal of Applied Physics,* vol. 52, no. 5S1, p. 05DC07, 2013.

[134] P.-C. Hsu *et al.*, "Sputtering deposition of p-type SnO films with SnO_2 target in hydrogen-containing atmosphere," *ACS Applied Materials & Interfaces,* vol. 6, no. 16, pp. 13724-13729, 2014.

[135] J. H. Han *et al.*, "Growth of p-type tin(II) monoxide thin films by atomic layer deposition from Bis(1-dimethylamino-2-methyl-2propoxy)tin and H_2O," *Chemistry of Materials,* vol. 26, no. 21, pp. 6088-6091, 2014.

[136] M. Liao, Z. Xiao, F.-Y. Ran, H. Kumomi, T. Kamiya, and H. Hosono, "Effects of Pb doping on hole transport properties and thin-film transistor characteristics of SnO thin films," *ECS Journal of Solid State Science and Technology,* vol. 4, no. 3, pp. Q26-Q30, 2015.

[137] B. Mohammad *et al.*, "State-of-the-art of metal-oxide memristor devices," *Nanotechnology Reviews,* vol. 5, pp. 311-329, 2015.

[138] L. Chua, "Memristor-the missing circuit element," *IEEE Transactions on Circuit Theory,* vol. 18, no. 5, pp. 507-519, 1971.

[139] R. Tetzlaff, *Memristors and memristive systems*. Springer, 2013.

[140] L. O. Chua and S. M. Kang, "Memristive devices and systems," *Proceedings of the IEEE,* vol. 64, no. 2, pp. 209-223, 1976.

[141] D. B. Strukov, G. S. Snider, D. R. Stewart, and R. S. Williams, "The missing memristor found," *Nature,* vol. 453, p. 80, 2008.

[142] H. Abunahla and B. Mohammad, "Memristor device overview," in *Memristor Technology: Synthesis and Modeling for Sensing and Security Applications*: Springer, 2018, pp. 1-29.

[143] Z. Hu *et al.*, "Ferroelectric memristor based on Pt/BiFeO$_3$/Nb-doped SrTiO$_3$ heterostructure," *Applied Physics Letters,* vol. 102, no. 10, p. 102901, 2013.

[144] D. Kim *et al.*, "Ferroelectric tunnel memristor," *Nano Letters,* vol. 12, no. 11, pp. 5697-5702, 2012.

[145] R. Waser, R. Dittmann, G. Staikov, and K. Szot, "Redox-based resistive switching memories—nanoionic mechanisms, prospects, and challenges," *Advanced materials,* vol. 21, no. 25-26, pp. 2632-2663, 2009.

[146] J. P. Strachan *et al.*, "Direct identification of the conducting channels in a functioning memristive device," *Advanced Materials,* vol. 22, no. 32, pp. 3573-3577, 2010.

[147] D.-H. Kwon *et al.*, "Atomic structure of conducting nanofilaments in TiO$_2$ resistive switching memory," *Nature Nanotechnology,* vol. 5, no. 2, p. 148, 2010.

[148] J. J. Yang *et al.*, "The mechanism of electroforming of metal oxide memristive switches," *Nanotechnology,* vol. 20, no. 21, p. 215201, 2009.

[149] D. Liu, H. Cheng, X. Zhu, G. Wang, and N. Wang, "Analog memristors based on thickening/thinning of Ag nanofilaments in amorphous manganite thin films," *ACS Applied Materials & Interfaces,* vol. 5, no. 21, pp. 11258-11264, 2013.

[150] H. N. Tran *et al.*, "Observation and characterization of memristive silver filaments in amorphous zinc-tin-oxide," *MRS Communications,* vol. 8, no. 3, pp. 1104-1110, 2018.

[151] I. Valov, R. Waser, J. R. Jameson, and M. N. Kozicki, "Electrochemical metallization memories—fundamentals, applications, prospects," *Nanotechnology,* vol. 22, no. 25, p. 254003, 2011.

[152] D. Kuzum, R. G. Jeyasingh, B. Lee, and H.-S. P. Wong, "Nanoelectronic programmable synapses based on phase change materials for brain-inspired computing," *Nano letters,* vol. 12, no. 5, pp. 2179-2186, 2011.

[153] M. Wuttig and N. Yamada, "Phase-change materials for rewriteable data storage," *Nature Materials,* vol. 6, no. 11, p. 824, 2007.

[154] J. J. Yang, D. B. Strukov, and D. R. Stewart, "Memristive devices for computing," *Nature Nanotechnology,* vol. 8, p. 13, 2012.

[155] K. Nagashima *et al.*, "Intrinsic mechanisms of memristive switching," *Nano Letters,* vol. 11, no. 5, pp. 2114-2118, 2011.

[156] J. He *et al.*, "Prediction of high-temperature point defect formation in TiO$_2$ from combined ab initio and thermodynamic calculations," *Acta Materialia,* vol. 55, no. 13, pp. 4325-4337, 2007.

[157] Y. B Nian, J. Strozier Jr, N. J Wu, X. Chen, and A. Ignatiev, "Evidence for an oxygen diffusion model for the electric pulse induced resistance change effect in transition-metal oxides," *Physical Review Letters,* vol. 98, p. 146403, 2007.

[158] J. R. Jameson and Y. Nishi, "Role of hydrogen ions in TiO$_2$-based memory devices," *Integrated Ferroelectrics,* vol. 124, no. 1, pp. 112-118, 2011.

[159] B. Magyari-Köpe, M. Tendulkar, S.-G. Park, H. D. Lee, and Y. Nishi, "Resistive switching mechanisms in random access memory devices incorporating transition metal oxides: TiO_2, NiO and $P_{r0.7}Ca_{0.3}MnO_3$," *Nanotechnology,* vol. 22, no. 25, p. 254029, 2011.

[160] S. J. Song *et al.*, "Real-time identification of the evolution of conducting nano-filaments in TiO_2 thin film ReRAM," *Scientific Reports,* vol. 3, p. 3443, 2013.

[161] E. Covi, S. Brivio, A. Serb, T. Prodromakis, M. Fanciulli, and S. Spiga, "HfO_2-based memristors for neuromorphic applications," in *2016 IEEE International Symposium on Circuits and Systems (ISCAS)*, 2016: IEEE, pp. 393-396.

[162] S. Seo *et al.*, "Reproducible resistance switching in polycrystalline NiO films," *Applied Physics Letters,* vol. 85, no. 23, pp. 5655-5657, 2004.

[163] H. Mähne, H. Wylezich, F. Hanzig, S. Slesazeck, D. Rafaja, and T. Mikolajick, "Analog resistive switching behavior of $Al/Nb_2O_5/Al$ device," *Semiconductor Science and Technology,* vol. 29, no. 10, p. 104002, 2014.

[164] Y. Pan *et al.*, "Mimicking synaptic plasticity and learning behaviours in solution processed SnO_2 memristor," *Journal of Alloys and Compounds,* vol. 757, pp. 496-503, 2018.

[165] K. Szot, W. Speier, G. Bihlmayer, and R. Waser, "Switching the electrical resistance of individual dislocations in single-crystalline $SrTiO_3$," *Nature Materials,* vol. 5, no. 4, p. 312, 2006.

[166] L. Chen, Y.-W. Dai, Q.-Q. Sun, J.-J. Guo, P. Zhou, and D. W. Zhang, "Al_2O_3/HfO_2 functional stack films based resistive switching memories with controlled SET and RESET voltages," *Solid State Ionics,* vol. 273, pp. 66-69, 2015.

[167] G. D. Wilk, R. M. Wallace, and J. Anthony, "High-κ gate dielectrics: Current status and materials properties considerations," *Journal of Applied Physics,* vol. 89, no. 10, pp. 5243-5275, 2001.

[168] S. Clima *et al.*, "RRAMs based on anionic and cationic switching: A short overview," *Physica Status Solidi (RRL)–Rapid Research Letters,* vol. 8, no. 6, pp. 501-511, 2014.

[169] N. Banno, T. Sakamoto, T. Hasegawa, K. Terabe, and M. Aono, "Effect of ion diffusion on switching voltage of solid-electrolyte nanometer switch," *Japanese Journal of Applied Physics,* vol. 45, no. 4S, p. 3666, 2006.

[170] X. Liang, Y. Chen, L. Shi, J. Lin, J. Yin, and Z. Liu, "Resistive switching and memory effects of AgI thin film," *Journal of Physics D: Applied Physics,* vol. 40, no. 16, p. 4767, 2007.

[171] C.-J. Kim *et al.*, "Characterization of silver-saturated Ge–Te chalcogenide thin films for nonvolatile random access memory," *Journal of Vacuum Science & Technology B: Microelectronics and Nanometer Structures Processing, Measurement, and Phenomena,* vol. 24, no. 2, pp. 721-724, 2006.

[172] M. Haemori, T. Nagata, and T. Chikyow, "Impact of Cu electrode on switching behavior in a $Cu/HfO_2/Pt$ structure and resultant Cu ion diffusion," *Applied Physics Express,* vol. 2, no. 6, p. 061401, 2009.

[173] C. Schindler, S. C. P. Thermadam, R. Waser, and M. N. Kozicki, "Bipolar and unipolar resistive switching in Cu-doped SiO_2," *IEEE Transactions on Electron Devices,* vol. 54, no. 10, pp. 2762-2768, 2007.

[174] H. Lv *et al.*, "Forming process investigation of Cu_xO memory films," *IEEE Electron Device Letters,* vol. 29, pp. 47-49, 2008.

[175] C. Chen, Y. Yang, F. Zeng, and F. Pan, "Bipolar resistive switching in Cu/AlN/Pt nonvolatile memory device," *Applied Physics Letters,* vol. 97, no. 8, p. 083502, 2010.

[176] F. Zhuge *et al.*, "Nonvolatile resistive switching memory based on amorphous carbon," *Applied Physics Letters,* vol. 96, no. 16, p. 163505, 2010.

[177] S. H. Jo, K.-H. Kim, and W. Lu, "Programmable resistance switching in nanoscale two-terminal devices," *Nano Letters,* vol. 9, no. 1, pp. 496-500, 2008.

[178] I. Valov *et al.*, "Atomically controlled electrochemical nucleation at superionic solid electrolyte surfaces," *Nature materials,* vol. 11, no. 6, p. 530, 2012.

[179] Y. Ogawa, S. Shindo, Y. Sutou, and J. Koike, "Molybdenum oxide-base phase change resistive switching material," *Applied Physics Letters,* vol. 111, no. 16, p. 163105, 2017.

[180] N. Yamada, E. Ohno, N. Akahira, K. i. Nishiuchi, K. i. Nagata, and M. Takao, "High speed overwritable phase change optical disk material," *Japanese Journal of Applied Physics,* vol. 26, no. S4, p. 61, 1987.

[181] S.-L. Wang, C.-Y. Chen, M.-K. Hsieh, W.-C. Lee, A. H. Kung, and L.-H. Peng, "Phase-change memory devices based on gallium-doped indium oxide," *Applied Physics Letters,* vol. 94, no. 11, p. 113503, 2009.

[182] M. Buchanan, J. B. Webb, and D. F. Williams, "The influence of target oxidation and growth-related effects on the electrical properties of reactively sputtered films of tin-doped indium oxide," *Thin Solid Films,* vol. 80, no. 4, pp. 373-382, 1981.

[183] K. Nagashima, T. Yanagida, K. Oka, and T. Kawai, "Unipolar resistive switching characteristics of room temperature grown SnO_2 thin films," *Applied Physics Letters,* vol. 94, no. 24, p. 242902, 2009.

[184] S. Almeida, B. Aguirre, N. Marquez, J. McClure, and D. Zubia, "Resistive Switching of SnO_2 Thin Films on Glass Substrates," *Integrated Ferroelectrics,* vol. 126, no. 1, pp. 117-124, 2011.

[185] M. Hota, J. Caraveo-Frescas, M. McLachlan, and H. N. Alshareef, "Electroforming-free resistive switching memory effect in transparent p-type tin monoxide," *Applied Physics Letters,* vol. 104, no. 15, p. 152104, 2014.

[186] J. Jin *et al.*, "Effects of annealing conditions on resistive switching characteristics of SnO_x thin films," *Journal of Alloys and Compounds,* vol. 673, pp. 54-59, 2016.

[187] C. Hsu, P. Chuang, and Y. Chen, "Resistive switching characteristic of low-temperature top-electrode-free tin-oxide memristor," *IEEE Transactions on Electron Devices,* vol. 64, no. 9, pp. 3951-3954, 2017.

[188] X. Yan *et al.*, "Memristor with Ag-cluster-doped TiO_2 films as artificial synapse for neuroinspired computing," *Advanced Functional Materials,* vol. 28, no. 1, p. 1705320, 2018.

[189] Z. Xiao and J. Huang, "Energy-efficient hybrid perovskite memristors and synaptic devices," *Advanced Electronic Materials,* vol. 2, no. 7, p. 1600100, 2016.

[190] Y. Li *et al.*, "Activity-dependent synaptic plasticity of a chalcogenide electronic synapse for neuromorphic systems," *Scientific Reports,* vol. 4, p. 4906, 2014.

[191] S. Saïghi *et al.*, "Plasticity in memristive devices for spiking neural networks," *Frontiers in Neuroscience,* vol. 9, p. 51, 2015.

[192] R. C. Froemke and Y. Dan, "Spike-timing-dependent synaptic modification induced by natural spike trains," *Nature,* vol. 416, no. 6879, p. 433, 2002.

[193] G.-q. Bi and M.-m. Poo, "Synaptic modifications in cultured hippocampal neurons: dependence on spike timing, synaptic strength, and postsynaptic cell type," *Journal of Neuroscience,* vol. 18, no. 24, pp. 10464-10472, 1998.

[194] A. V. Avizienis *et al.*, "Neuromorphic atomic switch networks," *PloS One,* vol. 7, no. 8, p. e42772, 2012.

[195] T. Hasegawa *et al.*, "Learning abilities achieved by a single solid-state atomic switch," *Advanced materials,* vol. 22, no. 16, pp. 1831-1834, 2010.

[196] T. Ohno, T. Hasegawa, T. Tsuruoka, K. Terabe, J. K. Gimzewski, and M. Aono, "Short-term plasticity and long-term potentiation mimicked in single inorganic synapses," *Nature Materials,* vol. 10, no. 8, pp. 591-595, 2011.

[197] M. S. Kulkarni and C. Teuscher, "Memristor-based reservoir computing," in *Proceedings of the 2012 IEEE/ACM International Symposium on Nanoscale Architectures*, 2012: ACM, pp. 226-232.

[198] L. Appeltant *et al.*, "Information processing using a single dynamical node as complex system," *Nature Communications,* vol. 2, p. 468, 2011.

[199] G. Tanaka *et al.*, "Recent advances in physical reservoir computing: A review," *Neural Networks,* 2018.

[200] C. Du, F. Cai, M. A. Zidan, W. Ma, S. H. Lee, and W. D. Lu, "Reservoir computing using dynamic memristors for temporal information processing," *Nature Communications,* vol. 8, no. 1, p. 2204, 2017.

[201] M. Lukoševičius and H. Jaeger, "Reservoir computing approaches to recurrent neural network training," *Computer Science Review,* vol. 3, no. 3, pp. 127-149, 2009.

[202] H. Jaeger, "Short term memory in echo state networks. ," in *GMD-German National Research Institute for Computer Science*, 2002.

[203] W. Maass, T. Natschläger, and H. Markram, "Real-time computing without stable states: A new framework for neural computation based on perturbations," *Neural Computation,* vol. 14, no. 11, pp. 2531-2560, 2002.

[204] M. C. Soriano *et al.*, "Delay-based reservoir computing: Noise effects in a combined analog and digital implementation," *IEEE Transactions on Neural Networks and Learning Systems,* vol. 26, no. 2, pp. 388-393, 2015.

[205] Y. Yi *et al.*, "FPGA based spike-time dependent encoder and reservoir design in neuromorphic computing processors," *Microprocessors and Microsystems,* vol. 46, pp. 175-183, 2016.

[206] B. Schrauwen, M. D'Haene, D. Verstraeten, and J. V. Campenhout, "Compact hardware liquid state machines on FPGA for real-time speech recognition," *Neural Networks,* vol. 21, no. 2, pp. 511-523, 2008.

[207] Q. Wang, Y. Li, and P. Li, "Liquid state machine based pattern recognition on FPGA with ring-activity dependent power gating and approximate computing," *2016 IEEE International Symposium on Circuit and Systems,* pp. 361-364, 2016.

[208] K. Vandoorne *et al.*, "Experimental demonstration of reservoir computing on a silicon photonics chip," *Nature Communications,* vol. 5, p. 3541, 2014.

[209] X. Yang, W. Chen, and F. Z. Wang, "Investigations of the staircase memristor model and applications of memristor-based local connections.," *Analog Integrated Circuits and Signal Processing,* vol. 87, pp. 263-273, 2016.

[210] D. Kudithipudi, Q. Saleh, C. Merkel, J. Thesing, and B. Wysocki, "Design and analysis of a neuromemristive reservoir computing architecture for biosignal processing," *Frontiers in Neuroscience,* vol. 9, p. 502, 2016.

[211] J. P. Carbajal, J. Dambre, M. Hermans, and B. Schrauwen, "Memristor models for machine learning," *Neural Computation,* vol. 27, no. 3, pp. 725-747, 2015.

[212] C. Merkel, Q. Saleh, C. Donahue, and D. Kudithipudi, "Memristive reservoir computing architecture for epileptic seizure detection," *Procedia Computer Science,* vol. 41, pp. 249-254, 2014.

[213] B. Schrauwen, J. Defour, D. Verstraeten, and J. Van Campenhout, "The introduction of time-scales in reservoir computing, applied to isolated digits recognition," in *International Conference on Artificial Neural Networks*, 2007: Springer, pp. 471-479.

[214] J.-H. Park, T. Sudarshan, Ed. *Chemical vapor deposition*. ASM international, 2001.

[215] J. A. Greer, "History and current status of commercial pulsed laser deposition equipment," *Journal of Physics D: Applied Physics,* vol. 47, no. 3, p. 034005, 2013.

[216] A. Anders, "A structure zone diagram including plasma-based deposition and ion etching," *Thin Solid Films,* vol. 518, no. 15, pp. 4087-4090, 2010.

[217] Y.-H. Jiang *et al.*, "Influence of rapid-thermal-annealing temperature on properties of rf-sputtered SnO$_x$ thin films," *Applied Surface Science,* vol. 327, pp. 358-363, 2015.

[218] P.-C. Hsu *et al.*, "Preparation of p-type SnO thin films and transistors by sputtering with robust Sn/SnO$_2$ mixed target in hydrogen-containing atmosphere," *Thin Solid Films,* vol. 585, pp. 50-56, 2015.

[219] P.-C. Hsu *et al.*, "Sputtering deposition of p-type SnO films using robust Sn/SnO$_2$ mixed target," *Thin Solid Films,* vol. 555, pp. 57-61, 2014.

[220] P. J. Kelly and R. D. Arnell, "Magnetron sputtering: a review of recent developments and applications," *Vacuum,* vol. 56, no. 3, pp. 159-172, 2000.

[221] K. Sarakinos, J. Alami, and S. Konstantinidis, "High power pulsed magnetron sputtering: A review on scientific and engineering state of the art," *Surface and Coatings Technology,* vol. 204, no. 11, pp. 1661-1684, 2010.

[222] A. Anders, "Tutorial: Reactive high power impulse magnetron sputtering (R-HiPIMS)," *Journal of Applied Physics,* vol. 121, no. 17, p. 171101, 2017.

[223] J. G. Partridge, E. L. H. Mayes, N. L. McDougall, M. M. M. Bilek, and D. G. McCulloch, "Characterization and device applications of ZnO films deposited by high power impulse magnetron sputtering (HiPIMS)," *Journal of Physics D: Applied Physics,* vol. 46, no. 16, p. 165105, 2013.

[224] Y. P. Purandare, A. P. Ehiasarian, M. M. Stack, and P. E. Hovsepian, "CrN/NbN coatings deposited by HIPIMS: A preliminary study of erosion–corrosion performance," *Surface and Coatings Technology,* vol. 204, no. 8, pp. 1158-1162, 2010.

[225] S. Chinchanikar and S. Choudhury, "Hard turning using HiPIMS-coated carbide tools: Wear behavior under dry and minimum quantity lubrication (MQL)," *Measurement,* vol. 55, pp. 536-548, 2014.

[226] R. Ganesan, B. Akhavan, J. G. Partridge, D. G. McCulloch, D. R. McKenzie, and M. M. Bilek, "Evolution of target condition in reactive HiPIMS as a function of duty cycle: An opportunity for refractive index grading," *Journal of Applied Physics,* vol. 121, no. 17, p. 171909, 2017.

[227] R. Ganesan *et al.*, "The role of pulse length in target poisoning during reactive HiPIMS: application to amorphous HfO_2," *Plasma Sources Science and Technology,* vol. 24, no. 3, p. 035015, 2015.

[228] T. Scientific. *What is X-Ray Photoelectron Spectroscopy (XPS)?* [Online]. Available: http://xpssimplified.com/whatisxps.php.

[229] M. W. Allen, C. H. Swartz, T. H. Myers, T. D. Veal, C. F. McConville, and S. M. Durbin, "Bulk transport measurements in ZnO: The effect of surface electron layers," *Physical Review B,* vol. 81, no. 7, p. 075211, 2010.

[230] J. F. Watts and J. Wolstenholme, *An introduction to surface analysis by XPS and AES* (An Introduction to Surface Analysis by XPS and AES). Wiley-VCH, 2003, p. 224.

[231] N. media. (2016). *The transmission electron microscope* [Online]. Available: http://www.nobelprize.org/educational/physics/microscopes/tem/.

[232] M. Chung and T. Everhart, "Simple calculation of energy distribution of low-energy secondary electrons emitted from metals under electron bombardment," *Journal of Applied Physics,* vol. 45, no. 2, pp. 707-709, 1974.

[233] G. E. Lloyd, "Atomic number and crystallographic contrast images with the SEM: a review of backscattered electron techniques," *Mineralogical Magazine,* vol. 51, no. 359, pp. 3-19, 1987.

[234] Warwick. (2010). *Transmission Electron Microscopy (TEM)* [Online]. Available: https://www2.warwick.ac.uk/fac/sci/physics/current/postgraduate/regs/mpags/ex5/techniques/structural/tem/.

[235] U. Maver, T. Velnar, M. Gaberšček, O. Planinšek, and M. Finšgar, "Recent progressive use of atomic force microscopy in biomedical applications," *TrAC Trends in Analytical Chemistry,* vol. 80, pp. 96-111, 2016.

[236] W. R. Thurber. (2016). *The Hall Effect* [Online]. Available: https://www.nist.gov/pml/engineering-physics-division/popular-links/hall-effect/hall-effect.

[237] Y. Suda, H. Kawasaki, K. Iwatsuji, and T. Ohshima, "Preparation of tin oxide (SnO_2) thin film gas sensor by PLD method," *IEEJ Transactions on Electronics, Information and Systems,* vol. 123, pp. 222-227, 2003.

[238] A. Rosental *et al.*, "Gas sensing properties of epitaxial SnO_2 thin films prepared by atomic layer deposition," *Sensors and Actuators B: Chemical,* vol. 93, no. 1-3, pp. 552-555, 2003.

[239] A. Anders, "Discharge physics of high power impulse magnetron sputtering," *Surface and Coatings Technology,* vol. 205, pp. S1-S9, 2011.

[240] R. Barik, N. Devi, D. Nandi, S. Siwal, S. K. Ghosh, and K. Mallick, "Multifunctional performance of nanocrystalline tin oxide," *Journal of Alloys and Compounds,* vol. 723, pp. 201-207, 2017.

[241] A. L. Patterson, "The Scherrer formula for X-ray particle size determination," *Physical Review,* vol. 56, no. 10, pp. 978-982, 1939.

[242] H. Giefers, F. Porsch, and G. Wortmann, "Kinetics of the disproportionation of SnO," *Solid State Ionics,* vol. 176, no. 1-2, pp. 199-207, 2005.

[243] X. Q. Pan and L. Fu, "Oxidation and phase transitions of epitaxial tin oxide thin films on ($\bar{1}$012) sapphire," *Journal of Applied Physics,* vol. 89, no. 11, pp. 6048-6055, 2001.

[244] J. Themlin, M. Chtaïb, L. Henrard, P. Lambin, J. Darville, and J. Gilles, "Characterization of tin oxides by x-ray-photoemission spectroscopy," *Physical Review B,* vol. 46, no. 4, pp. 2460-2466, 1992.

[245] H. Luo, L. Y. Liang, H. T. Cao, Z. M. Liu, and F. Zhuge, "Structural, chemical, optical, and electrical evolution of SnO x films deposited by reactive rf magnetron sputtering," *ACS Applied Materials & Interfaces,* vol. 4, no. 10, pp. 5673-5677, 2012.

[246] B. J. Murdoch, D. G. McCulloch, and J. G. Partridge, "Relationship between microstructure and electronic properties of energetically deposited zinc tin oxide," *Applied Physics Express,* vol. 9, no. 6, p. 065501, 2016.

[247] S. K. V. Farahani *et al.*, "Valence-band density of states and surface electron accumulation in epitaxial SnO_2 films," *Physical Review B,* vol. 90, no. 15, p. 155413, 2014.

[248] J. Tauc, R. Grigorovici, and A. Vancu, "Optical properties and electronic structure of amorphous germanium," *Physica Status Solidi,* vol. 15, no. 2, pp. 627-637, 1966.

[249] S. Baco, A. Chik, and F. M. Yassin, "Study on optical properties of tin oxide thin film at different annealing temperature," *Journal of Science and Technology,* vol. 4, no. 1, 2012.

[250] R. Kozma, R. E. Pino, and G. E. Pazienza, *Advances in neuromorphic memristor science and applications*. Springer Science & Business Media, 2012.

[251] A. Sebastian, M. L. Gallo, G. W. Burr, S. Kim, M. BrightSky, and E. Eleftheriou, "Tutorial: Brain-inspired computing using phase-change memory devices," *Journal of Applied Physics,* vol. 124, no. 11, p. 111101, 2018.

[252] Z. Wang *et al.*, "Memristors with diffusive dynamics as synaptic emulators for neuromorphic computing," *Nature Materials,* vol. 16, no. 1, p. 101, 2017.

[253] J. Borghetti *et al.*, "A hybrid nanomemristor/transistor logic circuit capable of self-programming," *Proceedings of the National Academy of Sciences,* vol. 106, no. 6, pp. 1699-1703, 2009.

[254] S. Tappertzhofen and S. Hofmann, "Embedded nanoparticle dynamics and their influence on switching behaviour of resistive memory devices," *Nanoscale,* vol. 9, no. 44, pp. 17494-17504, 2017.

[255] J. C. Adenilson, A. A. Cleber, M. B. Olivia, S. A. Luana, P. B. Eric, and R. L. Edson, "Back-to-back Schottky diodes: the generalization of the diode theory in analysis and extraction of electrical parameters of nanodevices," *Journal of Physics: Condensed Matter,* vol. 24, no. 22, p. 225303, 2012.

[256] M. Lenzlinger and E. H. Snow, "Fowler-Nordheim tunneling into thermally grown SiO_2," *Journal of Applied Physics,* vol. 40, no. 1, pp. 278-283, 1969.

[257] J. Maserjian and N. Zamani, "Behavior of the Si/SiO_2 interface observed by Fowler-Nordheim tunneling," *Journal of Applied Physics,* vol. 53, no. 1, pp. 559-567, 1982.

[258] M. Müller, G. X. Miao, and J. S. Moodera, "Exchange splitting and bias-dependent transport in EuO spin filter tunnel barriers," *EPL (Europhysics Letters),* vol. 88, no. 4, p. 47006, 2009.

[259] R. G. Forbes, "On the need for a tunneling pre-factor in Fowler–Nordheim tunneling theory," *Journal of Applied Physics,* vol. 103, no. 11, p. 114911, 2008.

[260] S. Kumar, M. D. Pickett, J. P. Strachan, G. Gibson, Y. Nishi, and R. S. Williams, "Local Temperature Redistribution and Structural Transition During Joule-Heating-Driven Conductance Switching in VO2," *Advanced Materials,* vol. 25, no. 42, pp. 6128-6132, 2013.

[261] B. J. Murdoch, D. G. McCulloch, R. Ganesan, D. R. McKenzie, M. M. M. Bilek, and J. G. Partridge, "Memristor and selector devices fabricated from $HfO_{2-x}N_x$," *Applied Physics Letters,* vol. 108, no. 14, p. 143504, 2016.

[262] M. D. Pickett, J. Borghetti, J. J. Yang, G. Medeiros-Ribeiro, and R. S. Williams, "Coexistence of memristance and negative differential resistance in a nanoscale metal-oxide-metal system," *Advanced Materials,* vol. 23, no. 15, pp. 1730-1733, 2011.

[263] S. K. Nandi, S. Li, X. Liu, and R. G. Elliman, "Temperature dependent frequency tuning of NbO_x relaxation oscillators," *Applied Physics Letters,* vol. 111, no. 20, p. 202901, 2017.

[264] S. Slesazeck *et al.*, "Physical model of threshold switching in NbO_2 based memristors," *RSC Advances,* vol. 5, no. 124, pp. 102318-102322, 2015.

[265] X. Liu, S. K. Nandi, D. K. Venkatachalam, K. Belay, S. Song, and R. G. Elliman, "Reduced threshold current in NbO_2 selector by engineering device structure," *IEEE Electron Device Letters,* vol. 35, no. 10, pp. 1055-1057, 2014.

[266] X. Liu, S. Li, S. K. Nandi, D. K. Venkatachalam, and R. G. Elliman, "Threshold switching and electrical self-oscillation in niobium oxide films," *Journal of Applied Physics,* vol. 120, no. 12, p. 124102, 2016.

[267] Y. Li, Z. Wang, R. Midya Midya, Q. Xia, and J. J. Yang, "Review of memristor devices in neuromorphic computing: Materials sciences and device challenges," *Journal of Physics D: Applied Physics,* vol. 51, p. 503002, 2018.

[268] J. P. Strachan, D. B. Strukov, J. Borghetti, J. J. Yang, G. Medeiros-Ribeiro, and R. S. Williams, "The switching location of a bipolar memristor: chemical, thermal and structural mapping," *Nanotechnology,* vol. 22, no. 25, p. 254015, 2011.

[269] A. K. Singh, A. Janotti, M. Scheffler, and C. G. Van de Walle, "Sources of electrical conductivity in SnO_2," *Physical Review Letters,* vol. 101, no. 5, p. 055502, 2008.

[270] F. Martínez *et al.*, "Optical properties and structure of HfO2 thin films grown by high pressure reactive sputtering," *Journal of Physics D: Applied Physics,* vol. 40, no. 17, p. 5256, 2007.

[271] E. Burstein, "Anomalous optical absorption limit in InSb," *Physical Review,* vol. 93, no. 3, p. 632, 1954.

[272] T. Minami, "New n-Type Transparent Conducting Oxides," *MRS Bulletin,* vol. 25, no. 8, pp. 38-44, 2000.

[273] P. Maier *et al.*, "Light sensitive memristor with bi-directional and wavelength-dependent conductance control," *Applied Physics Letters,* vol. 109, no. 2, p. 023501, 2016.

[274] G. Z. Cohen, Y. V. Pershin, and M. Di Ventra, "Second and higher harmonics generation with memristive systems," *Applied Physics Letters,* vol. 100, no. 13, p. 133109, 2012.

[275] Y. Viero *et al.*, "Light-stimulatable molecules/nanoparticles networks for switchable logical functions and reservoir computing," *Advanced Functional Materials,* vol. 28, no. 39, p. 1801506, 2018.

[276] D. Biolek, V. Biolkova, and Z. Kolka, "Memristive systems for analog signal processing," in *2014 IEEE International Symposium on Circuits and Systems (ISCAS),* 2014: IEEE, pp. 2588-2591.

[277] B. Schrauwen, D. Verstraeten, and J. Van Campenhout, "An overview of reservoir computing: theory, applications and implementations," in *Proceedings of the 15th European Symposium on Artificial Neural Networks. p. 471-482 2007,* 2007, pp. 471-482.

[278] D. S. Jeong, H. Schroeder, and R. Waser, "Coexistence of bipolar and unipolar resistive switching behaviors in a Pt∕TiO₂∕Pt stack," *Electrochemical and Solid-State Letters,* vol. 10, no. 8, pp. G51-G53, 2007.

[279] S. Li, X. Liu, S. K. Nandi, and R. G. Elliman, "Anatomy of filamentary threshold switching in amorphous niobium oxide," *Nanotechnology,* vol. 29, no. 37, p. 375705, 2018.

[280] S. H. Jo, K.-H. Kim, T. Chang, S. Gaba, and W. Lu, "Si memristive devices applied to memory and neuromorphic circuits," in *Proc. of 2010 IEEE International Symposium on Circuits and Systems,* 2010: IEEE, pp. 13-16.

[281] T. J. Raeber, Z. Zhao, B. J. Murdoch, D. R. McKenzie, D. G. McCulloch, and J. G. Partridge, "Resistive switching and transport characteristics of an all-carbon memristor," *Carbon,* vol. 136, pp. 280-285, 2018.

[282] S. K. Bose *et al.*, "Evolution of a designless nanoparticle network into reconfigurable boolean logic," *Nature Nanotechnology,* vol. 10, no. 12, pp. 1048-1052, 2015.

[283] C. Minnai, A. Bellacicca, S. A. Brown, and P. Milani, "Facile fabrication of complex networks of memristive devices," *Scientific Reports,* vol. 7, no. 1, p. 7955, 2017.

[284] S. Fostner and S. A. Brown, "Neuromorphic behavior in percolating nanoparticle films," *Physical Review E,* vol. 92, no. 5, p. 052134, 2015.

[285] F. Chávez *et al.*, "Sensing performance of palladium-functionalized WO3 nanowires by a drop-casting method," *Applied Surface Science,* vol. 275, pp. 28-35, 2013.

[286] B. C. Gierhart, D. G. Howitt, S. J. Chen, R. L. Smith, and S. D. Collins, "Frequency dependence of gold nanoparticle superassembly by dielectrophoresis," *Langmuir,* vol. 23, no. 24, pp. 12450-12456, 2007.

[287] F. Wang, C. He, M. Y. Han, J. H. Wu, and G. Q. Xu, "Chemical controlled reversible gold nanoparticles dissolution and reconstruction at room-temperature," *Chemical Communications,* vol. 48, no. 49, pp. 6136-6138, 2012.

[288] S. K. Bose, J. B. Mallinson, R. M. Gazoni, and S. A. Brown, "Stable Self-Assembled Atomic-Switch Networks for Neuromorphic Applications," *IEEE Transactions on Electron Devices,* vol. 64, no. 12, pp. 5194-5201, 2017.

[289] K. Terabe, T. Hasegawa, T. Nakayama, and M. Aono, "Quantized conductance atomic switch," *Nature,* vol. 433, no. 7021, pp. 47-50, 2005.

[290] W. Wang *et al.*, "MoS$_2$ memristor with photoresistive switching," *Scientific Reports,* vol. 6, p. 31224, 2016.

[291] B. Ibarlucea *et al.*, "Gating hysteresis as an indicator for silicon nanowire FET biosensors," *Applied Sciences,* vol. 8, no. 6, p. 950, 2018.

[292] S. Carrara, D. Sacchetto, M.-A. Doucey, C. Baj-Rossi, G. De Micheli, and Y. Leblebici, "Memristive-biosensors: A new detection method by using nanofabricated memristors," *Sensors and Actuators B: Chemical,* vol. 171, pp. 449-457, 2012.

[293] D. Verstraeten, B. Schrauwen, M. d'Haene, and D. Stroobandt, "An experimental unification of reservoir computing methods," *Neural Networks,* vol. 20, no. 3, pp. 391-403, 2007.

[294] L. Kövér *et al.*, "Electronic structure of tin oxides: High-resolution study of XPS and Auger spectra," *Surface and Interface Analysis,* vol. 23, no. 7-8, pp. 461-466, 1995.

[295] M. Moreno, R. Egerton, and P. Midgley, "Differentiation of tin oxides using electron energy-loss spectroscopy," *Physical Review B,* vol. 69, no. 23, p. 233304, 2004.

[296] H. Kabbara *et al.*, "Synthesis of nanocrystals by discharges in liquid nitrogen from Si–Sn sintered electrode," *Scientific Reports,* vol. 5, p. 17477, 2015.

[297] G. Corporate. *EELS Atlas - Sn* [Online]. Available: http://www.eels.info/atlas/tin.

[298] R. F. Egerton, "Electron energy-loss spectroscopy in the TEM," *Reports on Progress in Physics,* vol. 72, no. 1, p. 016502, 2008.

[299] E. Viana, J. González, G. Ribeiro, and A. De Oliveira, "Photoluminescence and high-temperature persistent photoconductivity experiments in SnO$_2$ nanobelts," *The Journal of Physical Chemistry C,* vol. 117, no. 15, pp. 7844-7849, 2013.

[300] N. B rsan and U. Weimar, "Understanding the fundamental principles of metal oxide based gas sensors; the example of CO sensing with SnO$_2$ sensors in the presence of humidity," *Journal of Physics: Condensed Matter,* vol. 15, no. 20, pp. R813-R839, 2003/05/09 2003.

[301] A. Kar, M. A. Stroscio, M. Meyyappan, D. J. Gosztola, G. P. Wiederrecht, and M. Dutta, "Tailoring the surface properties and carrier dynamics in SnO$_2$ nanowires," *Nanotechnology,* vol. 22, no. 28, p. 285709, 2011.

[302]   J. Samà *et al.*, "Site-selectively grown SnO_2 NWs networks on micromembranes for efficient ammonia sensing in humid conditions," *Sensors and Actuators B: Chemical,* vol. 232, pp. 402-409, 2016.

[303]   S. Ahlers, T. Becker, W. Hellmich, C. B.-v. Braunmühl, and G. Müller, "Temperature-and field-effect-modulation techniques for thin-film metal oxide gas sensors," in *Advanced Gas Sensing*: Springer, 2003, pp. 123-159.

[304]   J. H. Yoon *et al.*, "An artificial nociceptor based on a diffusive memristor," *Nature Communications,* vol. 9, no. 1, p. 417, 2018.

[305]   E. Nedaaee Oskoee and M. Sahimi, "Electric currents in networks of interconnected memristors," *Physical Review E,* vol. 83, no. 3, p. 031105, 2011.

[306]   J. Kremkow, A. Aertsen, and A. Kumar, "Gating of signal propagation in spiking neural networks by balanced and correlated excitation and inhibition," *Journal of Neuroscience,* vol. 30, no. 47, pp. 15760-15768, 2010.

[307]   B. K. Murphy and K. D. Miller, "Balanced amplification: a new mechanism of selective amplification of neural activity patterns," *Neuron,* vol. 61, no. 4, pp. 635-648, 2009.

[308]   S. Ganguli, D. Huh, and H. Sompolinsky, "Memory traces in dynamical systems," *Proceedings of the National Academy of Sciences,* vol. 105, no. 48, pp. 18970-18975, 2008.

[309]   A. Z. Stieg, A. V. Avizienis, H. O. Sillin, C. Martin-Olmos, M. Aono, and J. K. Gimzewski, "Emergent criticality in complex turing B-type atomic switch networks," *Advanced Materials,* vol. 24, no. 2, pp. 286-293, 2012.

[310]   D. B. Strukov and S. Williams, "Exponential ionic drift: Fast switching and low volatility of thin-film memristors," *Applied Physics A,* vol. 94, pp. 515-519, 2009.

[311]   X. Zou *et al.*, "Charge trapping-detrapping induced resistive switching in $Ba_{0.7}Sr_{0.3}TiO_3$," *AIP Advances,* vol. 2, p. 032166, 2012.

[312]   B. Choi *et al.*, "Resistive switching mechanism of TiO_2 thin films grown by atomic-layer deposition," *Journal of Applied hysics,* vol. 98, no. 3, p. 033715, 2005.

[313]   T. Bak, J. Nowotny, M. Rekas, and C. Sorrell, "Defect chemistry and semiconducting properties of titanium dioxide: I. Intrinsic electronic equilibrium☆," *Journal of Physics and Chemistry of Solids,* vol. 64, no. 7, pp. 1043-1056, 2003.

[314]   A. Sattar, S. Fostner, and S. A. Brown, "Quantized conductance and switching in percolating nanoparticle films," *Physical Review Letters,* vol. 111, no. 13, p. 136808, 2013.

[315]   H. O. Sillin *et al.*, "A theoretical and experimental study of neuromorphic atomic switch networks for reservoir computing," *Nanotechnology,* vol. 24, no. 38, p. 384004, 2013.

[316]   M. S. Kulkarni and C. Teuscher, "Memristor-based reservoir computing," in *2012 IEEE/ACM International Symposium on Nanoscale Architectures (NANOARCH)*, 2012: IEEE, pp. 226-232.

[317]   M. Prezioso, F. Merrikh-Bayat, B. Hoskins, G. C. Adam, K. K. Likharev, and D. B. Strukov, "Training and operation of an integrated neuromorphic network based on metal-oxide memristors," *Nature,* vol. 521, no. 7550, pp. 61-64, 2015.

Appendix A:

Supporting Information for Chapter 6

The correlation between two pairs of electrodes of a four-contact NND: channel 1 (Ch1 = top and bottom) and channel 2 (Ch2 = right and left) was investigated by applying double linear sweeps with an amplitude of 4 V and duration of ~26 s on one pair (control pair/channel) of the electrodes while a constant non-perturbative voltage of 100 mV was maintained at the other pair (driven pair/channel). Similar correlation between top-bottom channel and right-left channel were observed within 15 sweeps. Figure A-1 shows the correlation between two pairs of electrodes channel 1 (Ch1 = top and bottom) and channel 2 (Ch2 = right and left) in 5th, 10th and 15th sweeps.
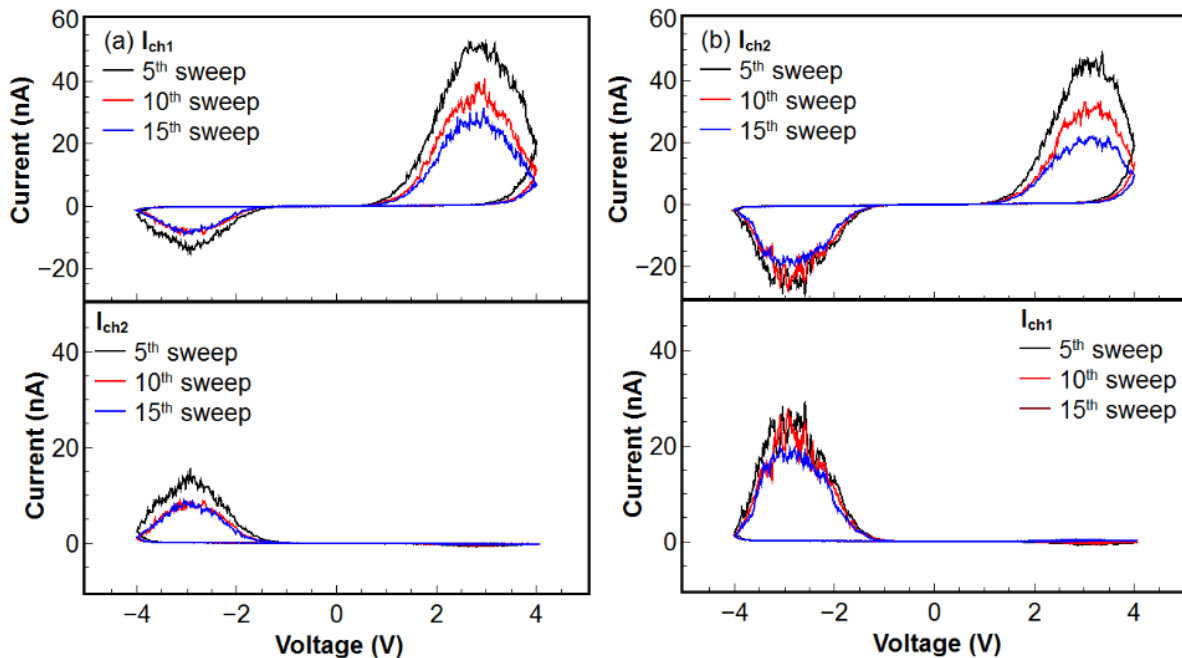
Figure A-1: Current response of two pairs of electrodes of a tin oxide NND when the 5th, 10th and 15th voltage sweeps applied on one electrode pair and a constant 100 mV was maintained at the other pair. Channel 1 (Ch1 = top and bottom) and channel 2 (Ch2 = right and left). (a) Channel 1 is control channel while channel 2 is a driven one. (b) Channel 2 is control channel while channel 1 is a driven one.

Similar measurements were carried out to explore the cross-correlation between combinations of two electrodes with double linear sweeps with an amplitude of 5 V and duration of ~26 s applied on one pair of the electrodes (name in blue in Table A-1) while a constant non-perturbative voltage of 100 mV kept at the

other pair (name in orange in Table A-1). Each plot contains IV characteristics of the control electrode pair (blue curve) and the driven electrode pair (orange curve). The cross-correlation plots show differently strong or weak correlation between the control pair and the driven pair. Based on these plots, the appropriate input and output electrodes can be selected to perform Boolean logic operations. An example was demonstrated in section 6.3.3.4.

Table A-2 shows the cross-correlations of all combinations of contact pairs were calculated from the measured resistances between the contact pairs under the application of a sequence of 10 pulses with pulse amplitude of 3 V (above threshold) and pulse width of 500 ms. Due to different responses obtained on the control (blue) and driven (orange) pairs when positive or negative bias was applied on the control pair, a sequence of 10 pulses of -3 V were also applied for correlation calculation. The voltage across the driven pairs was kept constant at 100 mV. The cross-correlation values varied from 0 (no correlation) to 1 (strong correlation). The correlation colour bar from yellow (no correlation) to green (strong correlation) was used to demonstrate the correlation degree between any two pairs of electrodes.

Figure A-2 presents voltage dependence on the conductance modulation using time-correlated inputs. A sequence of 10 pulses with the pulse amplitude of 5 V was applied across Ch2 (V_{Input}, I_{Ouput} = B, T) as reference while a train of 5 pulses with varying pulse amplitude was supplied to Ch1 (V_{Input}, I_{Ouput} = R, L). Current responses on these two channels were recorded at the end of each reference pulse.

Table A-1: Cross-correlation plots between combinations of two electrodes of a four-contact nanoparticle network device (NND).
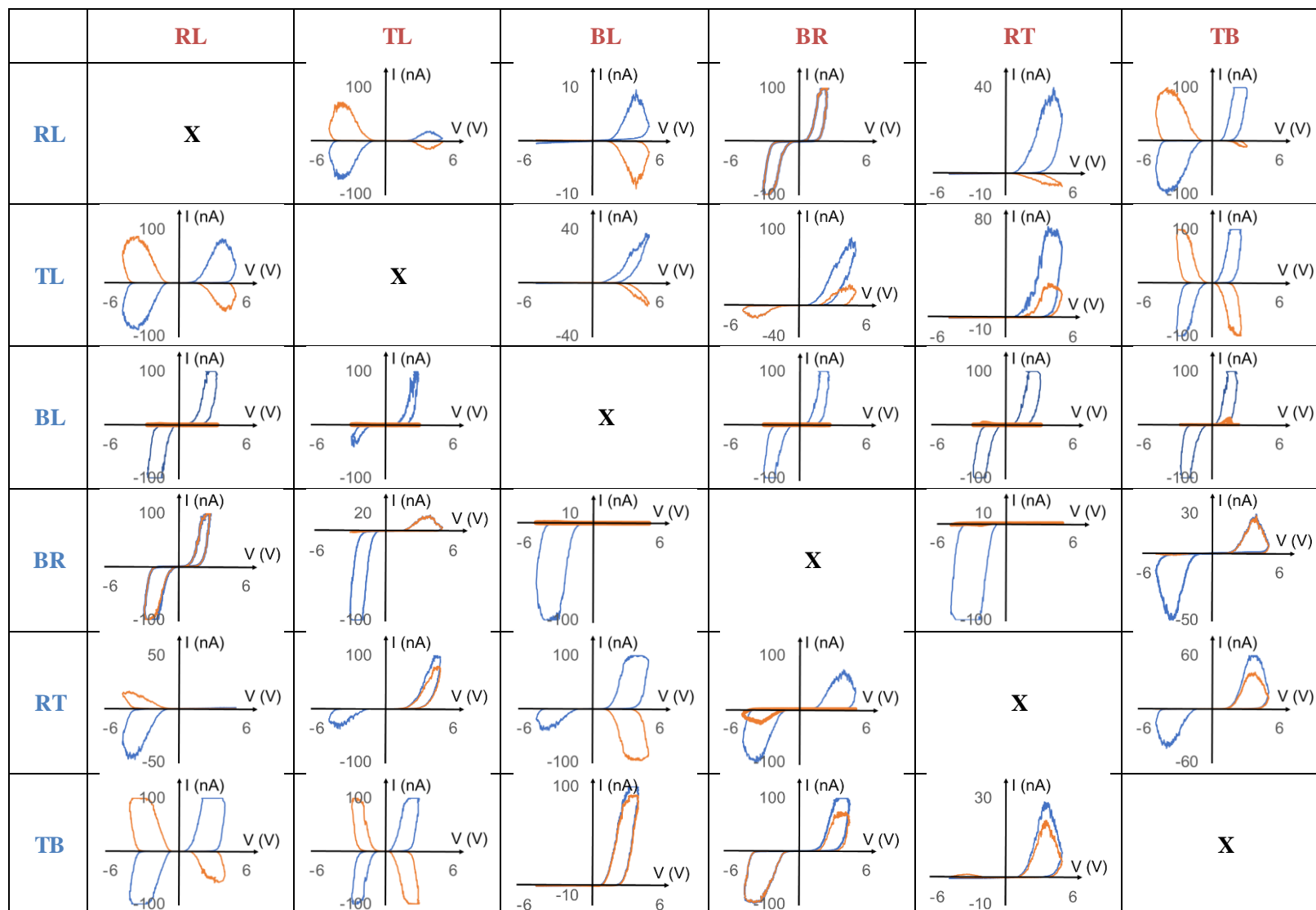
Where:

T, B, L, R: denote top, bottom, left and right electrodes of the NND.

RL, TL, BL, BR, RT, and TB: denote combinations of two electrodes of the NND (e.g. TB: top-bottom)

Table A-2: Cross-correlations of two contact pairs calculated from the measured resistances between the contact pairs when a sequence of 10 pulses with pulse amplitude of 3 V and pulse width of 500 ms was applied

	TR	TB / RB	TL / BL / RL			TR	TB / RB	TL / BL / RL		Correlation range
$V_{RL} > 0$	0.975	0.280	0.967		$V_{RL} < 0$	0.185	0.992	1.000		0.000
		0.978	0.998				1.000	0.041		0.045
			X					X		0.091
										0.136
$V_{TB} > 0$	0.967	X	0.994		$V_{TB} < 0$	0.129	X	0.932		0.182
		0.969	0.994				0.986	0.575		0.227
			0.929					0.998		0.273
										0.318
$V_{TR} > 0$	X	0.134	0.061		$V_{TR} < 0$	X	0.992	0.977		0.364
		0.990	0.143				0.269	0.997		0.409
			0.939					0.255		0.455
										0.500
$V_{TL} > 0$	0.997	0.370	X		$V_{TL} < 0$	0.061	0.997	X		0.545
		0.967	0.810				0.999	0.237		0.591
			0.824					1.000		0.636
										0.682
$V_{RB} > 0$	0.982	0.967	0.923		$V_{RB} < 0$	0.109	0.996	0.951		0.727
		X	0.299				X	0.842		0.773
			0.986					0.988		0.818
										0.864
$V_{BL} > 0$	0.095	0.969	0.095		$V_{BL} < 0$	0.990	0.036	0.994		0.909
		0.371	X				0.044	X		0.955
			0.135					0.780		1.000
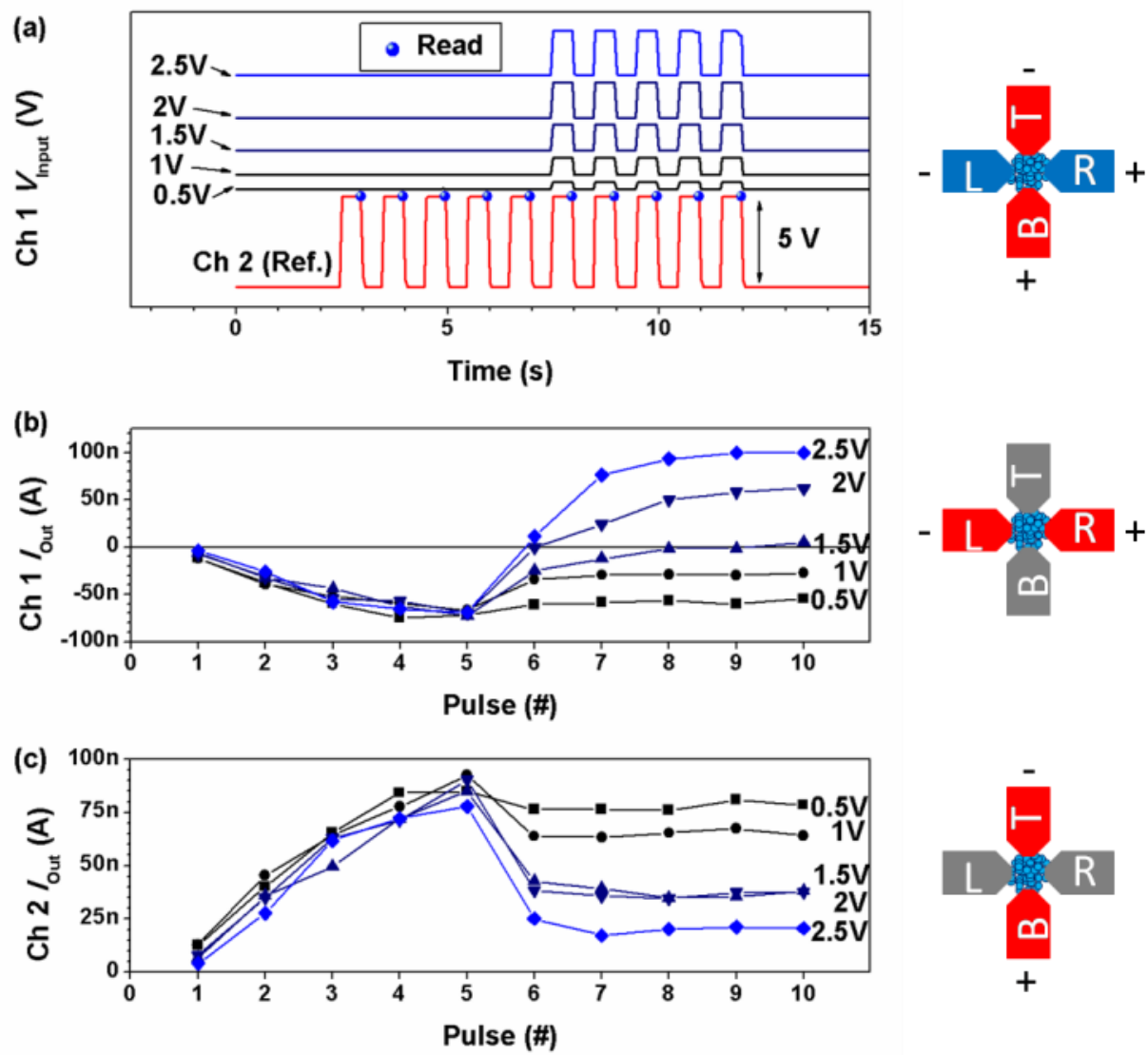
*Figure A-2: Voltage dependence on the conductance modulation using time-correlated inputs. (**a**) Input voltage pulse trains (500 ms duration, 500 ms intervals) supplied to Ch1 (V_{Input}, I_{Ouput} = R, L). Reference pulse train is supplied to Ch 2 (V_{Input}, I_{Ouput} = B, T). (**b**) Ch1 and (**c**) Ch2 output currents. The corresponding electrode configurations are shown schematically to the right of each panel.*

Appendix B:

Resistive switching nanoparticle networks self-assembled from mixed phase tin oxide: formation and network characteristics

(will be submitted)

Resistive switching nanoparticle networks self-assembled from mixed phase tin oxide: formation and network characteristics

Phuong Y Le[a], Billy J Murdoch[b], Anders J Barlow[c], Zijun C Zhao[d], David R McKenzie[d], Anthony S Holland[a], Dougal G McCulloch[b] and Jim G Partridge[b]

a.   School of Engineering, RMIT University, GPO Box 2476V, Melbourne VIC 3000, Australia.

        Email: phuong.leyen@rmit.edu.au

b.   School of Science, RMIT University, GPO Box 2476V, Melbourne VIC 3000, Australia.

c.   Centre for Materials and Surface Science (CMSS), Department of Chemistry and Physics, La Trobe University, Melbourne VIC 3086, Australia

d.   School of Physics, The University of Sydney, New South Wales 2006, Australia

We report a facile, top-down, method for assembling electrically-contacted, resistive-switching random networks. The random networks of nanoparticles were formed in ambient conditions within thin films of mixed phase tin oxide simply by passing limited current between on-film electrodes with nanoscale separations. The formation mechanism was found to be sensitive to the stoichiometry of the as-deposited film but networks were self-assembled within SnOx films in which $1.76 < x < 1.9$. Bidirectional volatile threshold-switching between high- and low-resistance states occurred immediately after network formation, again in ambient conditions. Comparison with filamentary memristors formed in similar films of mixed phase tin oxide highlighted the differing device characteristics and assisted in identification of the differing switching mechanisms. The networks exhibited characteristics of recurrent neural networks and efficient passive higher-order harmonic generation, suggesting suitability for applications including reservoir computing.

Introduction

With potential applications including non-volatile random-access memories and bio-inspired computing, resistive switching devices have attracted significant research interest.[138] Resistive switching devices, or memristors, are most frequently two-terminal metal-insulator-metal devices. The dense and non-porous insulator layer provides the functionality by exhibiting high- and low- resistance states (HRS and LRS). Switching between these states is achieved by applying voltage to the metal layers. Electric-field driven defect/impurity migration [141, 312, 313] and/or Joule heating induced phase modification are examples of mechanisms producing HRS/LRS switching. Sub-stoichiometric metal oxides such as TiO_{2-x},[141] $NbO_{1-x[266]}$ and $HfO_{2-x}N_x$ [261]are proven high endurance memristive layers but Si memristors have also been demonstrated[280]. Self-programmable circuits formed from TiO_2 memristors and Si transistors highlight the new computing approaches enabled by memristive circuit elements.[253]

Distinctly different resistive switching devices are formed from complex networks of nanoparticles or nanowires.[194, 275, 282, 283, 288, 309] The network constituents are normally metallic with surrounding insulating or semiconducting shells. Most often, the nanoparticles/wires are formed remotely before being deposited as a random network onto an appropriate surface.[283, 288] Electrodes can be formed on the same surface before or after the nanoparticle/wire deposition to provide electrical connectivity.[194, 283, 288] Resistive switching has been attributed to lowering/removal of the potential barriers separating the individual nanoparticles or nanowires and formation of conduction path(s) through the (initially) highly-resistive film/network.[194, 283, 289] Once again, application of electric-field and passage of current is an effective means to induce electromigration[283] and/or Joule heating related defect/impurity motion.[194] Diverse behaviours including quantized conduction,[289, 314] emulation of biological synaptic functions such as short- and long- term plasticity,[195, 196] photo-sensitive memristance[275, 290] and memristance modulated by bio-molecule attachment[292] have all been reported in these networks. Their non-linearity has also provided efficient production of harmonics from alternating inputs.[194, 275] Perhaps most significantly, reservoir computing is a potential application for these networks. 'Reservoir' describes a complex network of switching elements that transform input signals into a higher dimensional space.[198, 315, 316] After suitable training of their "output layers", reservoir computing circuits have completed tasks such as pattern recognition[200, 211, 317] with very high efficiency.

Many of the interesting characteristics reported to date in memristive nanoparticle networks have required vacuum and/or low temperature operation[282, 288]. In this paper, we report a facile

method for selective assembly of tin oxide nanoparticle networks on a substrate. These networks are formed within semi-insulating thin films of mixed phase tin oxide deposited onto insulating substrates by sputtering at room temperature. In a 'top-down' approach, the pristine film is transformed into the network of nanoparticles between lateral metal contacts (and nowhere else). This selective formation is achieved simply by applying a potential difference to the contacts to cause passage of (limited) current between them. After the 'electroforming' process, the networks of nanoparticles exhibit memristive characteristics including bidirectional threshold switching. These device characteristics are measured in ambient conditions at room-temperature using the same lateral contacts employed to transform the pristine film. The formation process and device characteristics are discussed here in detail.

Experimental

The tin oxide device layer was deposited onto SiO_2 (50 nm layer thickness on Si wafer) at room temperature using an AJA magnetron sputtering (MS) deposition system connected to a RUP-7 pulsed power supply. Prior to deposition, the system pressure was less than 1×10^{-6} Torr. A Sn target (3-inch diameter, 99.99% purity) was operated in high impulse power MS mode (with pulse amplitude, width and frequency of 640 V, 100 μs and 100 Hz). The potential of the substrate was allowed to float (at ~10 V) during the 20 min deposition. The 1:3 $Ar:O_2$ process pressure was 6.0 mTorr. The Sn magnetron source was positioned non-centrally in the chamber whilst the wafer was mounted centrally. This off-axis deposition process provided a small but quantifiable variation in film composition (Sn:O) across the wafer. The reactive deposition process produced a film approximately 25 nm in thickness. Following deposition, the wafer was diced into 10×10 mm² substrates for structural/electrical characterisation and device fabrication.

The compositions of the as-deposited tin oxide samples were determined using a Thermo Scientific K-alpha X-ray photoelectron spectroscopy (XPS) system with mono-chromated Al K-α source. An Asylum Research MFP-3D Infinity atomic force microscope (AFM) provided surface topography and step-height measurements. X-ray diffractograms obtained using a Bruker D4, operating in Bragg-Brentano configuration, indicated the films were nano-crystalline. Al Van der Pauw contacts were thermally evaporated and measurements using an Ecopia HMS-3000 system showed the as-deposited SnO_x films were semi-insulating.

The device contacts were formed lithographically. Electron-beam resist (950 PMMA A4, thickness 200 nm) was patterned using a FEI Nova NanoSEM electron microscope interfaced with Nabity NPGS electron beam writing software. The operating conditions were: 30.00 kV accelerating voltage, working distance 5.0 mm, beam current 22 pA. A Gatan PECS ion-beam deposition system was then used to deposit the 20 nm thick Pt contacts. With the device mounted on a probe-station, a Keysight B2902A twin channel source-measurement unit (SMU) enabled both initial electroforming and subsequent acquisition of two-probe current-voltage (I-V) characteristics. A current limit (I_{limit}) of 100 nA was imposed during the measurement. All electrical and scanning-probe measurements were performed at room-temperature in air.

The pristine and electro-formed devices were imaged using the FEI Nova NanoSEM and their oxidation states were revealed using Auger electron spectroscopy (AES). The latter was performed on a PHI 710 Scanning Auger Nanoprobe (SAN) (Physical Electronics, Chanhassen, USA) utilising a field emission electron source and a coaxial single pass cylindrical mirror analyser for electron energy analysis. The source was operated at 10 kV, 1 nA for spectroscopy and microscopy.

Results and discussion

As-deposited film, device architecture and electroforming

Figure 1 shows x-ray photoelectron spectra from an as-deposited (pristine) tin oxide device layer. SnO_2 was identified as the dominant phase from the Sn 3d spectrum shown in Fig 1(a). In this spectrum, the Sn^{4+} and Sn^{2+} components are deconvoluted. The peak intensity of Sn^{4+} (at 486.5 eV) significantly exceeds that of Sn^{2+} (at 485.8 eV). The composition calculated from XPS was 1(Sn):1.85(O). Other species detected using XPS included surface-bound -OH and -CO groups (visible in the fitted O1s spectrum Fig. 1(b)). Although OH attachment is known to cause downward band-bending and surface electron accumulation in n-type semiconducting oxides including ZnO and SnO_2,[229, 247] the as-deposited SnO_x film was semi-insulating. Fig. 1(c) shows a valence-band (VB) XPS spectrum (with binding energy range 0 - 10 eV) which includes contributions from SnO and from SnO_2. The peak centred at a binding energy of 2.04 eV is attributed to the Sn 5s-derived valence band maximum (VBM) in SnO while the peak centred at 4.14 eV is attributed to the O 2p-derived VB maximum in SnO_2.[14, 244] Hence, the as-

deposited film is mixed-phase. The important feature within the spectra (and film) is the presence of the minority SnO phase. The inherently n-type behaviour of the majority SnO_2 phase is compensated by acceptor-like states (above its VBM) caused by the inclusion of the SnO phase.
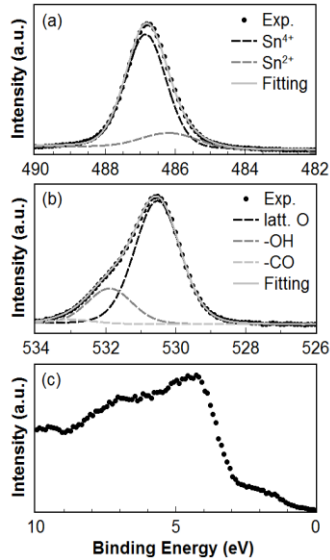

Fig. 1   XPS spectra from the SnO_x film in the (a) Sn 3d, (b) O 1s and (c) valence band regions. Deconvolution of the spectra enables quantification of the phase composition and surface adsorbates (see main text).

XPS produced no resolvable features attributable to metallic Sn but based on prior work[114], we expect that the Sn phase is present as nanoscale Sn clusters. The concentration of these Sn clusters would be higher in more Sn-rich SnO_x and as shown later, subtle changes in stoichiometry can affect the device characteristics. Despite the variation in the Sn:O composition caused by the off-axis deposition, very similar Sn 3d, O 1s and VB spectra were observed from all films and all films exhibited mixed phase composition. The ratio SnO_2:SnO ranged from 1:0.30 to 1:0.16 from the Sn-rich to O-rich sides of the wafer.

Figure 2(a) shows the device structure as a cross-sectional schematic. The evolution of the electrical characteristics during electroforming are shown in Fig. 2(b). The pristine device (with Sn:O of 1:1.85 and SnO_2:SnO of 1:0.18) exhibited high resistance (>10 GΩ) at low bias (path 1 in Fig. 2(b)) and there the I-V relationship is approximately linear (see inset). This is consistent with transport limited by back-to-back (Pt-SnO_x-Pt) Schottky diodes. In this device configuration, carrier emission over the potential barriers is excluded and direct tunnelling is the dominant transport mechanism. With an applied voltage of 27 V, the current

increases sharply (path 2 in Fig. 2(b)). Immediately after electroforming, the device enters its LRS (path 3 in Fig. 2(b)). Post electroforming, the threshold voltage decreased significantly, and the device exhibited distinct HRS and LRS separated by more than two-orders of magnitude, as shown in Fig. 2(b).

Before further discussion of the switching characteristics of the devices, we show the morphological/compositional changes that accompany the onset of resistive switching. Fig. 3(a) is an atomic force micrograph of the device immediately after the electroforming process. The region between the planar Pt electrodes clearly differs in its morphology to the surrounding unmodified layer (UL). Rather than the (as-deposited) flat film, it resembles a densely packed but porous network of nanoparticles. This change in morphology was observed immediately following the electroforming sweep in several similar devices. Electro-thermal simulations performed using Sentaurus TCAD suggest that the nanoscale region between the device electrodes may reach temperatures exceeding 1000°C during the electroforming process. SnO (the minority phase in the device layer) is known to decompose above 300°C[242] to yield product phases of SnO_2 and Sn.[242] Since interstitial Sn is an n-type donor in SnO_2, this leads to significantly increased conductivity. In the device electroforming characteristics in Fig. 2(b), the rapid thermally-induced increase in conduction is consistent with 'Path 2' and we attribute the morphological change to partial melting by Joule heating. In the ambient conditions, this melting is followed by rapid cooling and re-oxidation of the nanoparticles when the voltage and current are reduced. Hence, relaxation back to the HRS occurs within the nanoparticle network.

Interestingly, this transformation does not occur in films that are relatively oxygen poor. Samples taken from locations on the wafer closer to the Sn magnetron gun during deposition and therefore with higher Sn relative to O do also exhibit resistive-switching but this is caused by a filamentary conduction path within a substantially unmodified device layer. Further comparison of the formation and switching mechanisms of the network and filamentary devices is presented later in this article.

The composition of the nanoparticle network was investigated using AES. Fig. 3(b) shows spectra obtained from the as-deposited layer and from the nanoscale area between the Pt contacts after electroforming. The alterations in peak intensities and positions before/after electroforming are consistent with a change in the dominant oxidation state from SnO_2 to SnO.[294] Hence, there is a net loss of oxygen as the film is transformed into the network. We lack the resolution required to determine the composition of the individual
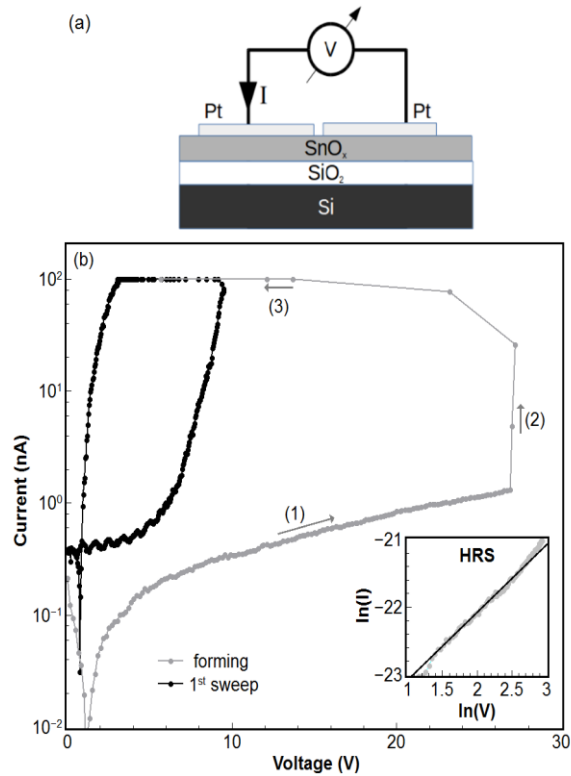
Fig. 2   (a) Cross-sectional schematic of the Pt contacted tin-oxide memristor and (b) current-voltage characteristic (V swept from 0 to 30 V, I_{limit} = 100 nA) recorded during the electroforming process (grey) and the first switching event recorded immediately afterwards (black). The inset shows that in the pristine state, current transport is consistent with direct tunnelling i.e. I proportional to V.

nanoparticles but given that all electrical measurements are performed in air, it is most probable that the nanoparticles are more oxidised at their surfaces i.e. they have a compositionally graded structure with the core being Sn-rich and the outer surface being more O-rich. Fig. 3(c) is an atomic force micrograph that shows a similar self-assembled nanoparticle network that is electrically connected to four planar electrodes. This device structure was achieved by performing two electroforming steps with characteristics similar to those in Fig. 2(b). The first being between contacts A and C and the second between contacts B and D. Once again, the facile electroforming process resulted in a memristive nanoparticle network located between the contacts and within a semi-insulating SnO_x film. I-V characteristics taken from all combinations of contact pairs immediately after formation exhibited pronounced hysteresis (not shown).

The remainder of this paper focuses on the characteristics of dual-contact devices. The device characteristics of four-contact devices will be discussed in detail elsewhere.

Resistive switching characteristics

Fig. 4(a) shows typical I-V characteristics of a nanoparticle network device (NND) measured after the electroforming sweep shown in Fig. 2(b). These measurements, taken with a 100 nA current limit
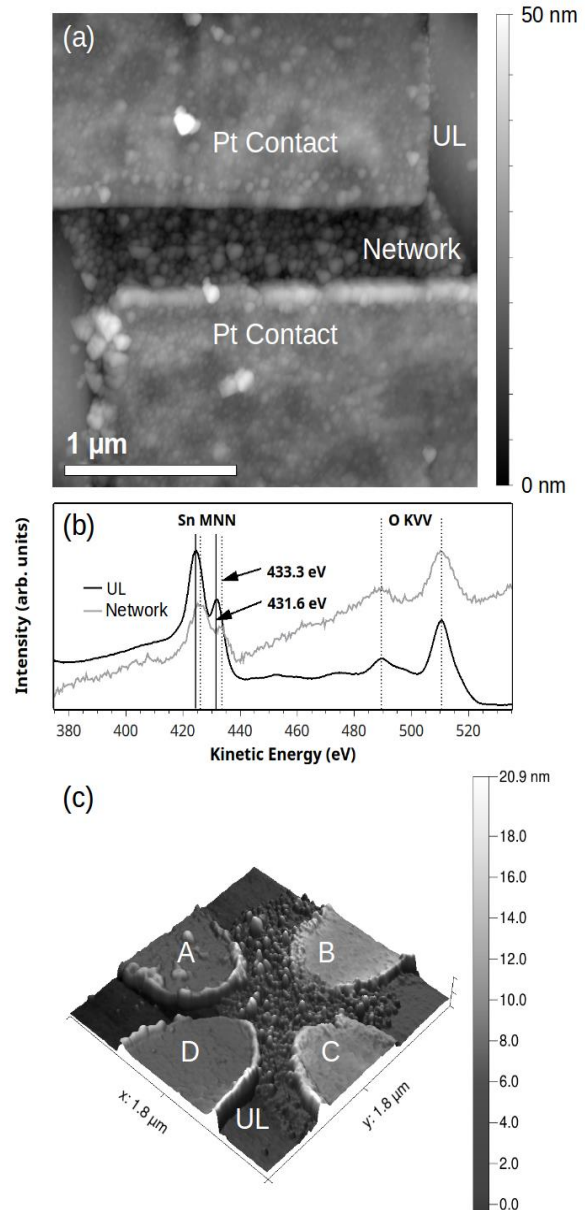

Fig. 3   (a) Atomic force micrograph and (b) Auger electron spectra taken from the memristive device after electroforming. The self-assembled network of nanoparticles and the unmodified layer (UL) are visible in (a). (c) Atomic force micrograph of a similar self-assembled nanoparticle network formed between four planar electrodes.

imposed and with one complete sweep taking 18 s, show I-V hysteresis characteristic of memristors. The device exhibits volatile resistive switching behaviour. The dominant transport mechanisms in the HRS and LRS differ as shown in Fig. 4(b) and (c). In the HRS (Fig, 4(b)), transport is limited by Schottky emission. In the LRS (Fig.

130

4(c)), the I-V characteristics are initially consistent with transport limited by Fowler-Nordheim tunnelling. As the voltage across the device falls below 1.0 V, the current diminishes rapidly, and the device relaxes back to the HRS.

To assist in determining the mechanisms causing the memristance in the NNDs, we now compare the NNDs with tin-oxide filamentary devices (TFDs) formed in similar (but not identical) mixed-phase material. The device layers in the TFDs remain as dense solid films throughout electroforming and undergo no significant surface morphological changes. Instead, microscopy (not shown) has revealed evidence of single nanoscale filaments between the contacts post-electroforming. These distinctly different memristive mechanisms are caused by the (slightly) different phase compositions of the as-deposited layers in the NNDs and TFDs. The more Sn-rich TFD tin oxide layers likely contain a higher concentration of Sn clusters relative to the tin oxide NND layers and it is believed that the higher density of clusters assists in establishing an initial conduction path. Joule heating along this conduction path then results in cluster-linking and a filament which localizes the device current and the Joule heating. The surrounding layer passes little current and therefore remains unaltered. The TFDs can be operated with higher current limits (up to 300 nA) without morphological transformation occurring. Above this limit, the filamentary region melts and the TFDs then either exhibit no switching or chaotic switching. In either case, formation of nanoparticle networks like those in Fig. 3 does not occur.

In the NNDs, switching to the LRS occurs (during electroforming) at a higher (~30%) threshold voltage relative to the TFDs. The density of Sn clusters is expected to be lower in the more oxygen-rich as-deposited layer in the NNDs. With a higher current, the NNDs reach a higher temperature during the electroforming process. Decomposition of the SnO phase is expected to increase conductivity and as the temperature rises further, the entire region of the device layer between the contacts becomes molten. Surface-energy minimisation and Ostwald ripening processes ultimately lead to the nanoparticle network morphology shown in Fig. 3(a) and (c).

Bidirectional resistive switching characteristics from a TFD (shown in Fig. 4(d)) resemble those of the NND but differences provide some insight into the underlying mechanisms. In the HRS (Fig 4(e)), the transport mechanism is characteristic of Schottky emission, as it is in NNDs. In the LRS (Fig.4(f)), the TFDs produce ohmic I-V characteristics. In these devices, a filament extends between the contacts when the LRS is entered. This filament must short out the Schottky barriers at the contacts for ohmic conduction to occur. When the

voltage/field is removed fitting show that the device current is once again limited by Schottky barriers. This is consistent with rupture of the filament and removal of the parallel connection across the Schottky barriers. Importantly, this memristive mechanism prevents the recurrent behaviour exhibited by some neural networks and by some atomic/nanoparticle switching networks[194].

Switching from the HRS to the LRS in the NNDs could occur by multiple mechanisms. As the voltage and current increase in the HRS, Joule heating causes an increase in the free electron concentration and an increase in the tunnelling current. Thermal expansion within the network may narrow the average width of the tunnel barriers separating the nanoparticles. Decomposition of the minority SnO phase is also expected, as in the TFDs. Significant re-configuration of the network seems unlikely given the highly reproducible switching characteristics shown in Fig. 4(a). Atomic force microscope images of an NND taken after the electroforming, 10th, and 20th I-V sweeps were image processed to yield average diameters of the
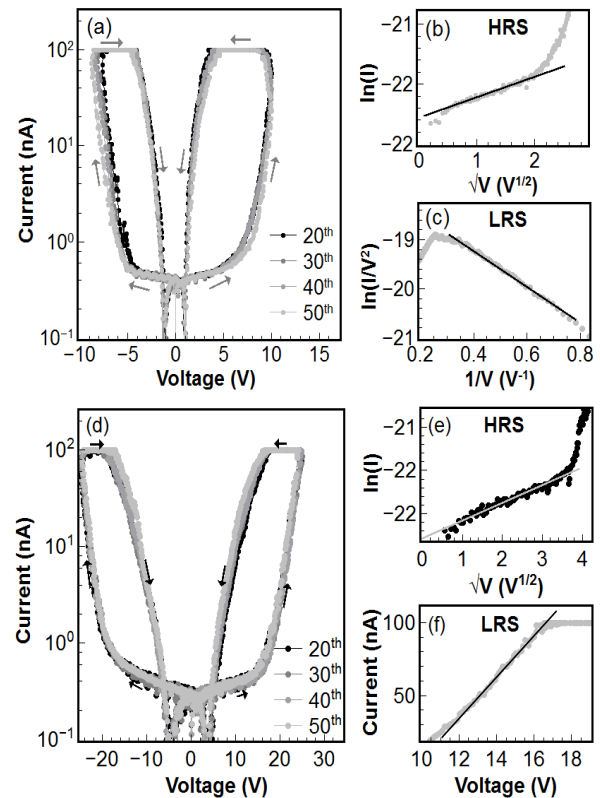

Fig. 4   (a) Cross-sectional schematic (a) I-V characteristics of an NND with 100 nA current limit imposed during measurement, (b) fitting of HRS and (c) Fowler-Nordheim fitting of averaged (20th, 30th, 40th, 50th) LRS characteristics of the NND. (d) I-V characteristics of the TFD with 100 nA current limit imposed, (e) fitting of the TFD HRS and of the (f) LRS.

nanoparticles within the network. These changed only from 19.8 to 20.3 nm.

It has been demonstrated in atomic switching networks[194, 275] and single memristors[274] that second-order harmonic generation occurs under sinusoidal voltage stimulus. Figure 5(a) shows the frequency responses of the NNDs (top) and TFDs (bottom) to 8V peak-to-peak, 9.25 Hz sinusoidal inputs. Generation of second-order harmonics is observed using both the NND and TFD, but third-order harmonics are only observed in the NND. The relative amplitude of higher harmonic generation in neural networks increases with the number of switching junctions.[194] Here, the NND exhibits an order of magnitude higher second harmonic at a bias of 8V when compared with the TFD (Fig. 5(a) and (b)). It has been suggested that NNDs such as these could be exploited in circuits requiring passive generation of higher-order harmonics. Theoretical modelling has shown that interconnected memristor circuits could achieve >40% power conversion rates for second-order harmonics, compared with 4.5% for optimal diode bridges.[274] The NNDs shown here generate second-order harmonics with voltage amplitudes up to 18% of the fundamental with no optimisation performed.

The relative amplitude of the second-order harmonics rises steeply in the NND as the applied voltage approaches the threshold voltage. In recurrent neural networks, asynchronous feedback inhibition[306, 307] arises due to delayed, opposing signals that occur across the same network junction, leading to voltage cancellation and associated damping of signals. Fig. 5a shows that, while the harmonics in the NND are of higher amplitude than those produced by the TFD, they are noticeably damped as a result of the recurrent dynamics inherent to the NND. In a fully recurrent network, complete signal cancellation occurs and therefore no harmonics are generated. Since higher order harmonics are observed in the NND, there are 'feedforward' pathways present and these must transmit the majority of the device current.[194, 308]

In summary, while the TFDs exhibit short-term memory and classification properties suitable for individual cells in reservoir computing circuits[24], only the NND provides the interconnectivity required for projection from a temporal signal into a high-dimensional space. Hence, there is great potential to explore reservoir computing functions using these simple-to-fabricate NNDs.
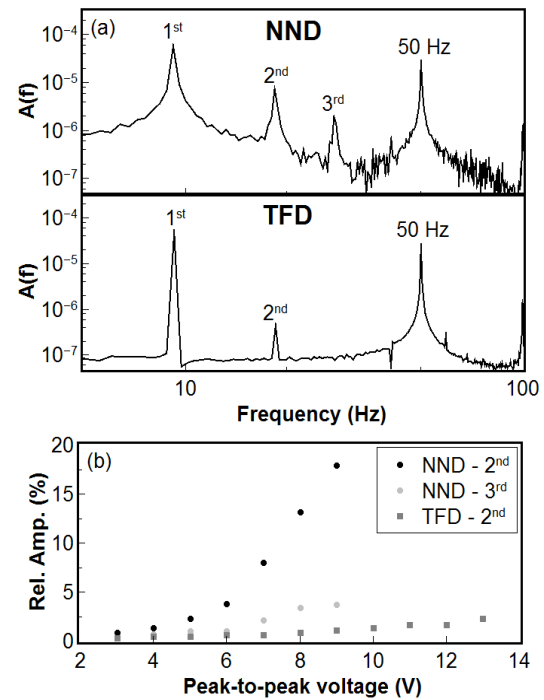
Conclusions

Fig. 5 (a) Amplitude spectra obtained after Fourier transformation of responses from the NND and TFD to 8V, 9.25 Hz sinusoidal input signals. (b) Relative amplitudes of harmonics generated in the NND and TFD as a function of bias voltage.

We have described a facile method for the fabrication of memristive nanoparticle networks in sub-stoichiometric (mixed phase) tin oxide. The effects of composition on the resulting devices have been discussed and comparison has been made between the network devices and filamentary memristors formed in similar layers. Stable, volatile, bidirectional resistive switching was observed in ambient and at room-temperature immediately after the formation of the nanoparticle networks. Higher-order harmonic generation and damping observed in the network devices are consistent with recurrent network behaviour rather than filamentary memristance. These characteristics suggest potential for similar devices to be exploited in applications requiring efficient passive harmonic generation and in reservoir computing.

Conflicts of interest

There are no conflicts to declare.

Acknowledgements

132

Notes and references

1. L. Chua, *IEEE Transactions on Circuit Theory*, 1971, **18**, 507-519.
2. B. J. Choi, D. S. Jeong, S. K. Kim, C. Rohde, S. Choi, J. H. Oh, H. J. Kim, C. S. Hwang, K. Szot, R. Waser, B. Reichenberg, and S. Tiedke, *Journal of Applied Physics*, 2005, **98**, 033715.
3. T. Bak, J. Nowotny, M. Rekas and C. C. Sorrell, *Journal of Physics and Chemistry of Solids*, 2003, **64**, 1043-1056.
4. D. B. Strukov, G. S. Snider, D. R. Stewart and R. S. Williams, *Nature*, 2008, **453**, 80-83.
5. X. Liu, S. Li, S. K. Nandi, D. K. Venkatachalam and R. G. Elliman, *Journal of Applied Physics*, 2016, **120**, 124102.
6. B. J. Murdoch, D. G. McCulloch, R. Ganesan, D. R. McKenzie, M. M. M. Bilek and J. G. Partridge, *Applied Physics Letters*, 2016, **108**, 143504.
7. S. H. Jo, K-H. Kim, T. Chang, S. Gaba and W. Lu, Proc. 2010 IEEE International Symposium on Circuits and Systems, 13-16.
8. J. Borghetti, Z. Li, J. Straznicky, X. Li, D. A. Ohlberg, W. Wu, D. R. Stewart and R. S. Williams, *Proceedings of the National Academy of Sciences*, 2009, **106**, 1699-1703.
9. S. K. Bose, C. P. Lawrence, Z. Liu, K. S. Makarenko, R. M. J. van Damme, H. J. Broersma and W. G. van der Wiel, *Nature Nanotechnology*, 2015, **10**, 1048-1052.
10. S. K. Bose, J. B. Mallinson, R. M. Gazoni and S. A. Brown, *IEEE Transactions on Electron Devices*, 2017, **64**, 5194-5201.
11. C. Minnai, A. Bellacicca, S. A. Brown and P. Milani, *Scientific Reports*, 2017, **7**, 7955.
12. A. V. Avizienis, H. O. Sillin, C. Martin-Olmos, H. H. Shieh, M. Aono, A. Z. Stieg and J. K. Gimzewski, *PloS One*, 2012, **7**, e42772.
13. Y. Viero, D. Guérin, A. Vladyka, F. Alibart, S. Lenfant, M. Calame and D. Vuillaume, *Advanced Functional Materials*, 2018, **28**, 1801506.
14. A. Z. Stieg, A. V. Avizienis, H. O. Sillin, C. Martin-Olmos, M. Aono and J. K. Gimzewski, *Advanced Materials*, 2012, **24**, 286-293.
15. K. Terabe, T. Hasegawa, T. Nakayama and M. Aono, *Nature*, 2005, **433**, 47-50.
16. A. Sattar, S. Fostner and S. A. Brown, *Physical Review Letters*, 2013, **111**, 136808.
17. T. Hasegawa, T. Ohno, K. Terabe, T. Tsuruoka, T. Nakayama, J. K. Gimzewski and M. Aono, *Advanced Materials*, 2010, **22**, 1831-1834.
18. T. Ohno, T. Hasegawa, T. Tsuruoka, K. Terabe, J. K. Gimzewski and M. Aono, *Nature Materials*, 2011, **10**, 591-595.
19. W. Wang, G. N. Panin, X. Fu, L. Zhang, P. Ilanchezhiyan, V. O. Pelenovich, D. Fu and T. W. Kang, *Scientific Reports*, 2016, **6**, 31224.
20. S. Carrara, D. Sacchetto, M.-A. Doucey, C. Baj-Rossi, G. De Micheli and Y. Leblebici, *Sensors and Actuators B: Chemical*, 2012, **171**, 449-457.
21. H. O. Sillin, R. Aguilera, H.-H. Shieh, A. V. Avizienis, M. Aono, A. Z. Stieg and J. K. Gimzewski, *Nanotechnology*, 2013, **24**, 384004.
22. L. Appeltant, M. C. Soriano, G. Van der Sande, J. Danckaert, S. Massar, J. Dambre, B. Schrauwen, C. R. Mirasso and I. Fischer, *Nature Communications*, 2011, **2**, 468.
23. M. S. Kulkarni and C. Teuscher, 2012 IEEE/ACM International Symposium on Nanoscale Architectures (NANOARCH), 226-232.
24. C. Du, F. Cai, M. A. Zidan, W. Ma, S. H. Lee and W. D. Lu, *Nature Communications*, 2017, **8**, 2204.
25. J. P. Carbajal, J. Dambre, M. Hermans and B. Schrauwen, *Neural Computation*, 2015, **27**, 725-747.
26. M. Prezioso, F. Merrikh-Bayat, B. Hoskins, G. C. Adam, K. K. Likharev and D. B. Strukov, *Nature*, 2015, **521**, 61-64.
27. M. W. Allen, C. H. Swartz, T. H. Myers, T. D. Veal, C. F. McConville and S. M. Durbin, *Physical Review B*, 2010, **81**, 075211.
28. S. K. V. Farahani, T. D. Veal, J. J. Mudd, D. O. Scanlon, G. W. Watson, O. Bierwagen, M. E. White, J. S. Speck and C. F. McConville, *Physical Review B*, 2014, **90**, 155413.
29. M. Batzill and U. Diebold, *Progress in surface science*, 2005, **79**, 47-154.
30. J-M Themlin, M. Chtaïb, L. Henrard, P. Lambin, J. Darville and J-M. Gilles, *Physical Review B*, 1992, **46**, 2460-2466.
31. J. A. Caraveo-Frescas, P. K. Nayak, H. A. Al-Jawhari, D. B. Granato, U. Schwingenschlögl and H. N. Alshareef, *ACS Nano*, 2013, **7**, 5160-5167.
32. H. Giefers, F. Porsch and G. Wortmann, *Solid State Ionics*, 2005, **176**, 199-207.
33. L. Kövér, Z. Kovács, R. Sanjinés, G. Moretti, I. Cserny, G. Margaritondo, J. Pálinkás and H. Adachi, *Surface and Interface Analysis*, 1995, **23**, 461-466.
34. G. Z. Cohen, Y. V. Pershin and M. Di Ventra, *Applied Physics Letters*, 2012, **100**, 133109.

35. J. Kremkow, A. Aertsen and A. Kumar, *Journal of Neuroscience*, 2010, **30**, 15760-15768.

36. B. K. Murphy and K. D. Miller, *Neuron*, 2009, **61**, 635-648.

37. S. Ganguli, D. Huh and H. Sompolinsky, *Proceedings of the National Academy of Sciences*, 2008, **105**, 18970-18975.